JUSTUS-LIEBIG-UNIVERSITÄT GIESSEN

IRG1/Itaconate Axis as an Immunometabolic Regulator of Pulmonary Hypertension

Inauguraldissertation

zur Erlangung des Grades eines

Doktors der Humanbiologie **(Dr. biol. hom.)**

des Fachbereichs Medizin
der Justus-Liebig-Universität Gießen

vorgelegt von

Golnaz Hesami

aus Qom, Iran

Gießen (2024)

Aus dem Fachbereich Medizin der Justus-Liebig-Universität Gießen

Aus dem Fachbereich Medizin

Der Justus-Liebig-Universität Gießen

Center for Infection and Genomics of the Lung (CIGL)

Lung Vascular Epigenetics

Gutachterin: Prof. Dr. Savai Pullamsetti, Soni

Gutachter: Prof. Dr. Ludger, Fink

Tag der Disputation: 13.05.2025

Dedicated to

My parents and Siavash,

for your love and support

Table of Contents

1. Introduction

1.1. Pulmonary hypertension

Pulmonary hypertension (PH) is a critical, progressive, and fatal cardiopulmonary disorder characterized by pulmonary vascular remodeling and an increase in mean pulmonary artery pressure (mPAP) above 20 mmHg, leading to right ventricular (RV) failure and death. This vascular remodeling is characterized by thickening of the intima, medial and/or adventitial layers of the pulmonary vessels (1). The pathogenesis of PH involves complex interactions between different cell types within the lung, including vascular cells, immune cells and circulating cells. Dysfunction of pulmonary artery endothelial cells (PAECs) due to shear stress or vascular injury triggers the overproduction of growth factors and proinflammatory cytokines that promote hyper-contractility, proliferation, and an apoptotic-resistant phenotype in pulmonary artery smooth muscle cells (PASMCs) and pulmonary artery adventitial fibroblasts (PAAFs), associated with remodeling of the extracellular matrix (ECM) production (2). Genetic factors, epigenetic alterations, metabolic reprogramming, and abnormal mitochondrial dynamics also play a crucial role in these pathological processes (3-6).

PH is clinically categorized into five groups based on the underlying causes (7, 8).
Group 1 PH: known as pulmonary arterial hypertension (PAH): this includes idiopathic or familial PAH with or without germline mutations, as well as PAH triggered by viruses (e.g., HIV) or exposure to drugs and toxins.
Group 2 PH: It is associated with left heart disease and is the most common cause of PH (9).
Group 3 PH: Caused by hypoxia or lung diseases such as pulmonary fibrosis, chronic obstructive pulmonary disease (COPD), emphysema, or interstitial lung disease.
Group 4 PH: Associated with chronic thromboembolic pulmonary hypertension (CTEPH) and occlusion of the proximal pulmonary arteries.
Group 5 PH: Caused by multifactorial or unclear mechanisms.

Despite advances in the diagnosis and treatment of PH over the last two decades, the disease remains incurable. Current therapies focus on three key pathways that regulate pulmonary vascular tone and cell proliferation: the nitric oxide pathway, the prostacyclin pathway and the endothelin pathway. New approaches such as the development of drugs that target specific molecular signaling pathways (e.g. platelet-derived growth factor (PDGF), Bone morphogenetic proteins/ Transforming growth factor-β (BMP/TGF-ß)) are currently being investigated (10). Understanding the comprehensive pathophysiology of PH is crucial for the development of more effective treatments that could improve the quality of life and survival rates of patients with this debilitating disease.

1.1.1. RV remodeling and failure

Chronic RV hypertrophy and failure, as seen in pathological conditions such as PH, are characterized by dilation of the RV lumen and thickening of the RV wall. These changes are associated with reduced exercise tolerance, poor functional capacity and reduced cardiac output (CO) and often lead to death in PH patients. In the initial stages of RV remodeling, the RV adapts by increasing its afterload to maintain CO and function, which is referred to as the adaptive phase. This hypertrophy enables the heart to generate significant pressure to counteract the increasing afterload. However, prolonged pressure overload leads to maladaptive RV function and subsequent uncoupling of the RV and pulmonary artery, termed the maladaptive phase (11). Numerous studies have investigated the cellular and molecular mechanisms underlying the adaptive and maladaptive phases of RV remodeling and the transition phase. At the cellular level, key features include cardiomyocyte hypertrophy, immune cell infiltration, cardiac fibroblast hyperproliferation and their transition to myofibroblasts (12). In these studies, excessive collagen and ECM deposition, impaired angiogenesis, ischemia, inflammation, metabolic dysregulation, mitochondrial dysfunction, impaired neurohormonal homeostasis, and increased reactive oxygen species (ROS) production were found to contribute to RV remodeling and failure (13-16). Integration of RV transcriptomes with plasma proteomes from PAH patients has shown that the ECM proteins, Nidogen (1NID1), C1q/TNF-Related Protein 1 (C1QTNF1) and Cartilage acidic protein 1(CRTAC1) are deregulated in decompensated RV patients, suggesting that they may serve as biomarkers to identify the development of a maladaptive RV state (17).

Examination of the transcriptomic signature of RV failure in two different PH rat models, the monocrotaline (MCT) and Sugen hypoxia models, revealed enrichment of signaling pathways related to endothelial-to-mesenchymal transition, inflammation, and metabolism (18). Multiomics integration analysis of proteome and RNA sequencing data from RV samples of MCT rats revealed significant enrichment in purine and ribose metabolism, mitochondrial and respiratory chain, and cellular respiration (19). Therefore, a comprehensive understanding of the molecular and cellular mechanisms responsible for RV hypertrophy and failure in PH is critical for the development of targeted therapeutic strategies to improve outcomes in these patients.

1.2. Cardiovascular disease

Cardiovascular disease (CVD) remains a major global health problem and is the leading cause of death worldwide. They include a broad spectrum of diseases of heart and blood vessels, such as stroke, heart failure (HF), hypertensive heart disease, rheumatic heart disease and peripheral arterial disease. As the main cause of morbidity and mortality, CVD represents a

major financial burden for healthcare systems and has a significant impact on quality of life and life expectancy. In 2016, almost a third of global deaths were due to CVD and it is predicted that this number could rise to over 23 million by 2030. Although the age-adjusted mortality rate for CVD has fallen by 27.3% in recent decades, the total number of deaths increased by 42.4% between 1990 and 2015, highlighting the growing burden of this disease on societies worldwide (20, 21).

1.2.1. Myocardial infarction

Myocardial infarction (MI), also known as heart attack, is the most common cause of HF in the Western world (22). MI is a critical CVD characterized by irreversible damage to myocardial cells as a result of prolonged ischemia due to coronary artery occlusion (23). This cell loss triggers a cascade of biochemical and structural changes in the heart that initiate processes such as necrosis, apoptosis, inflammation and dedifferentiation in the infarct border zone (24). These changes contribute to myocardial remodeling, which involves dilatation and hypertrophy of the myocardium and the formation of a collagen scar to compensate for the damaged tissue (25).

Remodeling after MI is divided into early and late phases, with the early phase characterized by expansion of the infarct zone (26) and the late phase involving global left ventricular dilation and hypertrophy (26). Mechanistic markers such as the release of transforming growth factor-β (TGF-β) and increased levels of natriuretic peptides, particularly NT-pro BNP, play a prominent role in these processes (27). In addition, the infiltration of immune cells, including macrophages, monocytes and neutrophils, into the infarct zone is crucial for the initiation and maintenance of the inflammatory response required for tissue repair (25). The pathophysiological changes following an infarction can significantly impair the heart's ability to pump blood efficiently and lead to HF (28). After MI, the heart undergoes cellular and neurohumoral changes that impair its function and structure. The acute loss of myocardium increases loading conditions and leads to ventricular remodeling, which continues until an equilibrium is reached between the stretching forces and the tensile strength of the collagen scar (29). Key mechanistic markers include increased noradrenaline levels and activation of the renin-angiotensin-aldosterone system, which drive compensatory mechanisms but also contribute to further deterioration (30). Factors such as infarct size and location, recurrent ischemia, and the extent of myocardial stunning influence the extent of remodeling and the risk of HF (31). As the heart struggles to compensate, symptoms such as volume overload, tachycardia and dyspnea manifest, highlighting the complex interplay of cellular dysfunction and neurohormonal activation in the progression of HF (28).

1.3. Inflammation and immune dysregulation in PH

Inflammation is a common feature of various forms of PH, with recent studies emphasizing the important role of chronic inflammation and immune system dysregulation in the pathogenesis of PAH (32). Hypoxia, a major trigger of immune and inflammatory responses, plays a critical role in mediating complex vascular homeostasis, which in turn controls vascular remodeling in the lung. This process is characterized by the persistent infiltration of immune cells and the elevation of numerous proinflammatory factors, ultimately leading to immune dysregulation (33). Specific immune cell activities such as the recruitment of monocytes and macrophages, the infiltration of T and B cells and the dysfunction of regulatory T cells and the increase of classical dendritic cells (cDCs) and monocyte-derived dendritic cells (mo-DCs) in the perivascular area are associated with the initiation and exacerbation of PAH (34-38). In the MCT rat model, reducing these inflammatory cells by inhibiting the chemokine CXC motif chemokine 12 (CXCL12) (NOX-A12), which attracts and activates immune cells, improved hemodynamics and pulmonary vascular remodeling (38). The presence of tertiary lymphoid tissue and extracellular neutrophil traps in plexogenic lesions, as well as circulating inflammatory cytokines, chemokines and proteases, is further evidence of the inflammatory nature of PAH (39, 40).

PAECs and inflammatory cells are both important sources and targets of chemokines and cytokines that drive pulmonary vascular remodeling in PH (41). Prominent proinflammatory cytokines such as interleukin 6 (IL-6) and interleukin 1β (IL-1β) can directly influence the proliferation, migration and differentiation of PAECs, PASMCs and immune cells (42, 43). IL-1β and tumor necrosis factor (TNF)-α are associated with the accumulation of ECM proteins such as fibronectin observed in PAH lesions (44). Dysregulated expression of chemokines and cytokines, including IL-6, interleukin 8 (IL-8) and interleukin 10 (IL-10), has been associated with poorer clinical outcomes in PAH patients and serves as a biomarker for disease progression (45, 46). Elevated levels of these inflammatory mediators have been detected in remodeled pulmonary vessels, where they promote recruitment of additional immune cells and vascular remodeling (37). Loss-of-function mutations in the BMPR2 gene, the most common genetic cause of PH, are associated with significant inflammation and immune dysregulation. This increased inflammation, together with impaired TGF-β signaling, promotes pulmonary vascular remodeling and exacerbates the disease (47). Consequently, the study of these inflammatory processes holds great potential for the development of novel therapeutic approaches aimed at modulating immune responses to treat PH (48).

1.4. The bone marrow niche and hematopoietic stem cells

The bone marrow (BM) is the major hematopoietic organ in adults, playing a vital role in the continuous generation of blood and immune cells throughout life. Hematopoietic stem cells (HSCs) are housed in specialized microenvironments in the BM niches, which are essential for regulating the behavior and function of HSCs. The concept of the hematopoietic niche was first introduced in 1978 and described as an environment in which stem cells interact with the surrounding cells that determine their behavior (49). These niches are primarily located within the trabecular bone and consist of various cell types such as endothelial cells (ECs), mesenchymal stromal cells (MSCs), osteolineage cells and adipocytes, all of which support the maintenance and function of the HSC (50).

The adult BM circulation is highly vascularized and is innervated by sympathetic and parasympathetic nerve fibers, creating a complex network that facilitates signaling pathways involving cytokines, chemokines and hormones. This signaling network modulates HSC activity in response to various physiological stimuli, including normal cell turnover, circadian rhythm, hematopoietic replenishment requirements, and immune response to damage or infection. These niches are primarily located in perivascular regions, which are further subdivided into sinusoidal and arteriolar compartments (51). The spatial positioning of HSCs in these compartments is thought to influence their quiescence and cell cycle activation, as the sinusoidal regions may provide better access to nutrients, cytokines and oxygen, which are critical for cell cycle progression (52). However, some studies have also identified dormant HSCs near the sinusoids, indicating an ongoing debate about the exact structure of the niche and the organization of HSCs (53). Leptin receptor-positive ($LepR^{+}$) MSCs and ECs are key components of the BM niche that contribute to the maintenance of HSCs through the secretion of factors such as CXCL12 and stem cell factor (SCF) (54, 55). ECs also support hematopoiesis through their secreted molecules and surface signaling that directly interact with hematopoietic progenitor cells (52, 56).

The identification and study of HSCs has evolved considerably since Weissman and colleagues first enriched HSC populations with surface markers in 1988 (57). Over time, additional markers such as Stem cells antigen-1 (Sca-1), KIT proto-oncogene, receptor tyrosine kinase (c-Kit), Cluster of differentiation 34 (CD34) and signaling lymphocyte activation molecule (SLAM) markers, etc. have been identified, allowing precise isolation and characterization of HSCs (58-60). HSCs possess remarkable versatility and are able to differentiate into all blood cell lineages, including immune cells such as macrophages, ensuring continuous renewal of the hematopoietic system throughout life (61). Hematopoiesis begins during embryogenesis and continues in adulthood to ensure the balance of blood cell production. In the adult BM, HSCs undergo both symmetric and asymmetric divisions to either maintain the stem cell pool or generate progenitor cells that further differentiate. Ultimately,

these progenitor cells lead to the production of more than 100 billion new blood cells per day (50).

Single-cell analysis and serial transplantation studies have demonstrated considerable heterogeneity among HSCs, revealing differences in their ability to form mature cells and self-renew (62). Advances in single-cell genomics have improved our understanding of hematopoiesis, revealing a complex continuum of differentiation with intermediate stages and distinct progenitor cell populations (63). These findings challenge the traditional hierarchical view of hematopoiesis and point to a more interconnected and dynamic process.

HSCs are categorized into two main subgroups: Long-term HSCs (LT), which support hematopoiesis over longer periods of time, and short-term HSCs (ST), which provide transient reconstitution (64, 65). ST-HSCs are particularly important for rapid hematopoietic recovery, especially after transplantation (66). The revised hematopoietic hierarchy also emphasizes the presence of multipotent progenitor cells (MPP) that exhibit lineage preferences while remaining flexible in differentiation. These MPPs include the lymphoid-primed MPP (MPP^{Ly}), granulocyte-monocyte-primed MPPs (MPP^{GM}), megakaryocyte-erythrocyte-primed MPPs (MPP^{MkE}) which further differentiate into common lymphoid, myeloid and erythroid progenitor cells. These CMPs eventually give rise to monocytes, which then mature into macrophages in response to certain environmental stimuli (61). This differentiation process is critical for maintaining tissue homeostasis and ensuring effective immune responses throughout the body.

1.5. Macrophage: classification and functions

Macrophages are one of the most important cellular compartments of innate immunity and function as professional phagocytes. These cells perform important tissue-specific roles by maintaining homeostasis in tissues, fighting infections and contributing to tissue repair by removing dead cells after cell injury (67).

In 1882, Elia Metchnikoff discovered macrophages as the cells responsible for phagocytizing foreign bodies in starfish larvae. This groundbreaking discovery led to Metchnikoff and Paul Ehrlich being awarded the Nobel Prize in Physiology or Medicine in 1908 (68). Macrophages are characterized by a high degree of plasticity, which enables them to respond differently to a variety of stimuli. Despite their versatility, macrophages share basic functions, such as phagocytizing foreign bodies, pathogens and apoptotic cells and triggering immune responses by secreting a variety of cytokines and chemokines. These common functions are controlled by a central macrophage program that includes key lineage-determining transcription factors (TFs) such as Spi-1 Proto-Oncogene (PU.1), MAF BZIP transcription factor B (MAFB) and zinc finger E-box binding homeobox 2 (ZEB2). These TFs play a critical role in the development and fate determination of monocytic cell populations (69, 70)

The activation status of macrophages, which varies in response to stimuli from their tissue environment, serves as the basis for classifying different macrophage phenotypes. These stimuli include microbial pathogens, cytokines and chemokines, metabolites, cellular components such as cell membranes, DNA and RNA, and microenvironmental factors such as oxygen levels and pH. This classification system distinguishes between two extreme macrophage phenotypes: the classically activated macrophages (M1) and the alternatively activated macrophages (M2) (71, 72).

Bacterial components such as lipopolysaccharide (LPS) and T-helper 1 cells (Th1) cytokines such as Interferon Gamma (IFNγ) drive macrophage polarization towards the classically activated M1 phenotype, which is characterized by a robust proinflammatory response (67). In addition, succinate, a by-product of the tricarboxylic acid cycle (TCA) in mitochondria, has been identified as a proinflammatory molecule that specifically induces IL-1β production in various immune cells, including macrophages (72, 73). Environmental factors also play a role, with hypoxia shown to exacerbate the proinflammatory responses of macrophages under LPS stimulation (74). M1 macrophages exhibit a distinct proinflammatory transcriptional profile driven by factors such as Signal Transducer and Activator of Transcription 1 (STAT1) and Interferon Regulatory Factor 3 (IRF3). These transcriptional activators promote the production of Th1 cell-attracting chemokines (e.g., CXCL9 and CXCL10) and proinflammatory mediators such as TNFα, IL-1β, IL-12 and reactive oxygen and nitrogen species. These molecules confer potent proinflammatory, antimicrobial and tumoricidal functions to M1 macrophages (67). In contrast, Th2 cytokines such as interleukin-4 (IL-4) and IL-13 polarize macrophages towards the M2 phenotype. Metabolic factors such as alpha-ketoglutarate (αKG), another intermediate of the TCA cycle, have been shown to promote the anti-inflammatory M2 phenotype (75). In addition, environmental factors such as acidosis can also drive macrophages into the M2 phenotype. For example, acidic conditions in the tumor microenvironment favor M2 polarization, whereas neutralization of tissue acidity reduces M2 properties and promotes the proinflammatory M1 phenotype (76, 77). M2 macrophages are characterized by the expression of scavenger and mannose receptors such as Mannose receptor (CD206) and the production of polyamines via the arginase pathway. They also secrete growth factors and ECM components, while having low levels of IL-12 and elevated levels of IL-10. This profile endows M2 macrophages with capabilities for parasite clearance, tissue remodeling and wound healing and tumor progression (75).

The classification of macrophages based on their inflammatory responses has added a new dimension to cellular metabolism, which has traditionally been viewed only as an energy source. Recent studies have shown that cellular metabolism plays a significant role in the activation and polarization of macrophages towards the M1 and M2 phenotypes (76). In the same line, metabolic distinctions serve as key identifiers for these phenotypes. M1

macrophages are primarily dependent on glycolysis and exhibit impaired TCA cycle activity associated with increased production of ROS and accumulation of the unique metabolite itaconic acid (itaconate). In contrast, M2 macrophages rely on oxidative phosphorylation and fatty acid oxidation, maintaining an intact TCA cycle and proper mitochondrial function (77) (Figure 1.1).

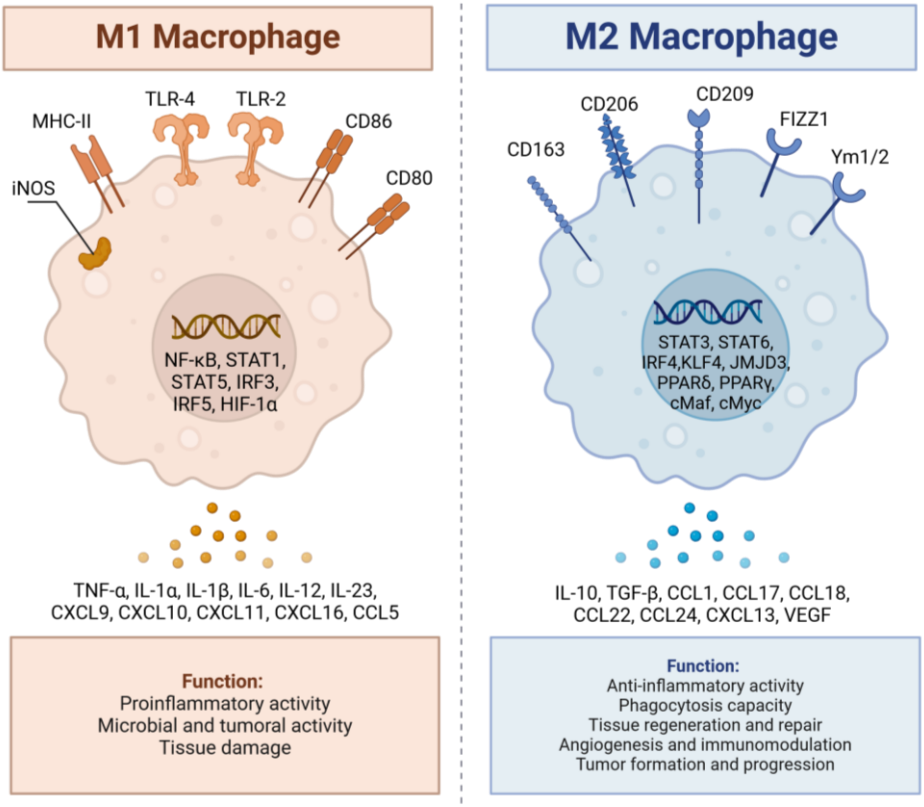

Figure 1.1. Macrophage polarization to proinflammatory (M1) and anti-inflammatory (M2) macrophages. Created with BioRender.com.

1.5.1. Pulmonary macrophages: origin and function

Pulmonary macrophages are divided into two different types: Alveolar macrophages (AM) and interstitial macrophages (IM), which arise in three developmental waves from the yolk sac, fetal liver and BM (78).

AMs, which are tissue-resident macrophages, are localized in the alveolar compartment and airways, where they play a key role in maintaining immune balance (79). AMs are generated in lung tissue during embryonic development, prior to the generation of HSCs. Studies in mice have shown that AMs have an embryonic origin derived primarily from mesenchymal progenitor cells in the yolk sac and in a second wave from embryonic liver mononuclear cells (80). AMs have self-renewal potential and proliferate independently (81). Granulocyte–macrophage colony-stimulating factor (GM-CSF) secreted by alveolar type II cells induces the expression of Peroxisome Proliferator-Activated Receptor γ (PPARγ), an important regulator

of lipid metabolism in AMs. By activating PPARγ signaling, AMs play a vital role in surfactant clearance in the alveoli. In addition, AMs support their own homeostasis and development by producing TGF-β (82). Misharin et al. identified a novel subset of AMs in the fibrotic lung that are derived from blood mononuclear cells and have a pro-fibrotic transcriptome signature, highlighting the dynamic and responsive nature of macrophages under pathologic conditions (83).

IMs are derived from blood monocytes originating from myeloid stem cells located in BM and spleen. They are recruited to the lungs during the activation of immune responses (84). In contrast to AMs, BM–derived macrophages (BMDMs) have a short lifespan, proliferate infrequently and are constantly renewed. C-X3-C Motif Chemokine Ligand 1 (CX3CL1) and C-C Motif Chemokine Ligand 2 (CCL2) are two potent chemokines that stimulate the migration of monocytes from BM into the tissue. Monocytes infiltrated into the tissue differentiate into macrophages and dendritic cells (DCs) and contribute to adaptive immune responses through their ability to present antigens (85). Both AMs and IMs play essential roles not only in maintaining lung function under normal conditions but also in contributing to inflammatory and pathological states, such as pulmonary fibrosis and PH.

1.5.2. Cardiac macrophages: origin and function

Cardiac macrophages consist of resident cardiac macrophages (RCMs) and monocyte-derived macrophages, which are derived from different sources and have specific phenotypes and functions (86). These two types of macrophages can be distinguished by the expression of the C-C chemokine receptor 2 (CCR2). RCMs are CCR2 cells of embryonic origin derived from yolk sac and fetal liver progenitor cells. RCMs arise during embryonic development and maintain their number through self-renewal properties. The heart is one of the few organs in which a significant number of yolk sac macrophages persist into adulthood (87). During development, circulating monocytes replace fetal liver monocytes (88). RCMs play a vital role in tissue repair by secreting anti-inflammatory messengers and eliminating apoptotic cells, thereby preventing myocardial fibrosis and cardiac hypertrophy. In addition, RCMs facilitate cardiac electrical conduction through the distal atrioventricular node by expressing connexin 43, with depletion of CCR2 RCMs leading to arrhythmias (89, 90). They also contribute to proper coronary plexus remodeling and coronary angiogenesis by secreting insulin-like growth factor 1 (IGF1) (90). $CCR2^{+}$ recruited macrophages are derived from monocytes derived from hematopoietic stem and progenitor cells (HSPCs) in the BM, known as BMDMs (91). The chemokine ligand CX3CL1 is strongly associated with the recruitment of BMDMs into the damaged heart (87). $CCR2^{+}$ macrophages promote monocyte recruitment through a myeloid differentiation primary response 88 (MYD88)-dependent mechanism that leads to secretion of monocyte chemoattractant proteins (MCPs) and subsequent mobilization of monocytes (92).

Pathogen/damage-associated molecular patterns (PAMPs/DAMPs) are potent activators of cardiac macrophages. $CCR2^{+}$ macrophages exhibit a proinflammatory transcriptome signature and express genes involved in the NLR Family Pyrin Domain Containing 3 (NLRP3) inflammasome and Nuclear Factor Kappa B (NF-κB) signaling, particularly IL-1β (93). Both RCMs and monocyte-derived macrophages can express major histocompatibility complex class II (MHC-II), which is associated with antigen presentation and T cell activation. MHC-II-rich subsets play a critical role in antigen presentation and clearance of pathogens (93). In newborn mice, the expression of MHC-II in embryonic CCR2 macrophages is extremely low, whereas the CCR2-MHC-II-rich population gradually increases after birth. Based on CCR2 and MHC-II expression, three main subgroups of cardiac macrophages can be distinguished in mice: $CCR2^{-}MHCII^{low}$, $CCR2^{-}MHC\text{-}II^{high}$ and $CCR2^{+}MHC\text{-}II^{high}$ (94).

1.6. Macrophages in cardiopulmonary disease

1.6.1. Macrophages in pulmonary hypertension

Myeloid leukocytes, especially macrophages, are the main culprits for inflammation and the subsequent development of PH. An increase in perivascular macrophages was found in the remodeled pulmonary vessels of PH patients, indicating their central role in inflammation and vascular remodeling (32). Hypoxia-induced pulmonary vascular remodeling also depends on the recruitment of circulating monocytes/macrophages, highlighting the critical importance of macrophages in PH progression (38, 95).

The inflammatory microenvironment in the pulmonary vasculature is characterized by infiltrating immune cells into perivascular area, their secreted products and the ECM. In this environment, factors such as ion homeostasis imbalance, hypoxia, increased reactive oxygen species and low pH can activate macrophages, leading to metabolic dysregulation and abnormal gene transcription (96, 97) These perturbations can lead to abnormal macrophage activation, which disrupts the balance of the M1/M2 phenotype and results in excessive secretion of chemokines or growth factors that accelerate PASMC proliferation and PAEC transformation (97). In addition, increased chemokine levels in the lung recruit circulating monocytes to replace resident macrophages (34).

Recent studies question the traditional M1/M2 polarization as it does not fully capture the complexity of macrophage gene expression *in vivo*. There is evidence that macrophages can simultaneously express M1 and M2 genes during injury, repair and progression of PH (98). Macrophage low (MacLow) mice, generated through doxycycline-inducible CD68-driven expression of the cytotoxic diphtheria toxin A chain, exhibited PAH when treated with doxycycline and IL-4. This was accompanied by a disruption in the M1/M2 macrophage balance in both the lungs and BM. Similarly, studies in PAH patients revealed a comparable

M1/M2 imbalance, underscoring the complex and pivotal role of macrophages subtypes in the pathogenesis of PAH (97).

In a hypoxia exposure study in mice, IMs and perivascular macrophages showed an early increase, while AMs remained unaffected. Gene expression analyzes showed that AMs at day 4 and 14 and IMs at day 4 were characterized by hypoxia-induced mitochondrial dysfunction, proinflammatory gene activation and mTOR complex 1 (mTORC1) signaling. However, on day 14, IMs switched to an anti-inflammatory and pro-reparative transcriptional state (99).

Further insights were provided by Kumar and colleagues in a single-cell transcriptome study of murine pulmonary IMs exposed to hypobaric hypoxia. The results show an initial acute inflammatory phase characterized by an enrichment of IFNγ, Interleukin 2 (IL-2) and IL-6 signaling pathways, followed by a pro-remodeling phase with dysregulated chemokine production, hemoglobin clearance, tissue repair processes and activation of specific complement pathways (100). Cytokines such as CCR5 and IL-1R1, which are expressed by both macrophages and PASMCs, can act as bidirectional chemotactic agents and maintain the abnormal proliferation of PASMCs (96). Chemokine systems such as CCL2-CCR2, CX3CL1-CX3CR1 and CCL5-CCR5 are critical for macrophage recruitment in PH, with receptors on ECs, PASMCs and macrophages, suggesting complex interactions between these cell types (101-103).

In PH, macrophages also play a role in the activation of T cells by secreting cytokines that lead to the release of inflammatory mediators such as TNF-α and IFNγ by T cells, which in turn contribute to vascular remodeling (104). Understanding the complex role and behavior of macrophages, including their gene expression and response to various stimuli, may provide valuable insights into potential therapeutic targets for the treatment of PH. Further exploration of macrophage biology in PH will be critical to developing more effective treatments and improving patient outcomes.

1.6.2. Macrophages in myocardial infarction

Macrophages play a crucial role in the progression and healing of CVD through their dynamic phenotypic changes and their multiple functions in inflammation and tissue repair. In ischemic HF, damaged cardiomyocytes release DAMPs that activate pattern recognition receptors (PRRs) on surviving parenchymal cells. This activation triggers the secretion of inflammatory cytokines and chemokines that attract monocytes and other inflammatory cells to the affected area (105). In the context of chronic ischemia, the most striking pathologic finding is interstitial fibrosis in the remote zone, which is primarily caused by persistent inflammation and structural remodeling of the heart (88).

Following MI, macrophages and other inflammatory cells migrate into the infarct zone and initiate the early proinflammatory phase. This process is characterized by the release of proinflammatory cytokines that increase inflammation and support the clearance of necrotic tissue (105). During MI, leukocyte recruitment further enhances the inflammatory response, increases DAMP production and facilitates efferocytosis, the process of removing dying cells and tissue degradation by proteases and oxidases(106). Efferocytosis of apoptotic cardiomyocytes, largely mediated by macrophages expressing myeloid-epithelial-reproductive tyrosine kinase (Mertk), is critical for the transition to resolution of inflammation and wound healing (107). Once the necrotic debris is cleared, macrophages change phenotype and begin producing anti-inflammatory cytokines, ending the inflammatory phase and promoting tissue repair (108)

The inflammatory phase, which generally lasts zero to four days after ischemia, is characterized by the recruitment of immune cells and the clearance of necrotic tissue. Ly6C^{high} monocytes are recruited to the infarct zone via CCR2/CCL2 signaling and differentiate into CCR2^{+}MHC-II^{high} macrophages to replace the lost resident macrophages, thereby playing a dominant role in this initial inflammatory phase (109, 110). In contrast, CCR2^{-} resident macrophages can suppress monocyte recruitment, which is a key mechanism to prevent myocardial fibrosis after injury (111). Proinflammatory mediators such as NLRP3 inflammasome, IL-6, angiotensin-II (Ang-II) and especially IL-1β contribute to fibrosis by upregulating pro-fibrotic genes such as TGF-β1 and connective tissue growth factor (CTGF) in cardiac fibroblasts (112-116). In addition, macrophages secrete metalloproteinases (MMPs) during the inflammatory phase to regulate the infiltration of other immune cells such as neutrophils and macrophages (117).

Recent research has emphasized the role of mitochondrial metabolism in macrophage efferocytosis. Deficiency of mitochondrial complex I in macrophages has been shown to promote glycolysis and increased ROS production in mitochondria, which exacerbates the inflammatory response, impairs efferocytosis, and ultimately impedes fibroblast proliferation and scar formation after MI (118).

After the first three days of MI, anti-inflammatory mediators are gradually produced that suppress neutrophil infiltration, enhance phagocytosis of apoptotic neutrophils by macrophages, and promote the conversion of recruited CCR2+Ly6C^{high} macrophages into reparative phenotypes (119).

Systemic hypertension and valvular heart disease cause pressure overload, a mechanical stress that leads to cardiac hypertrophy and myocardial fibrosis. Pressure overload is typically divided into a compensatory phase and a decompensated phase (120). During the compensatory phase, CCR2^{+} macrophages predominate, helping to inhibit fibrosis and

hypertrophy. However, with persistent monocyte infiltration, monocyte-derived $CCR2^+$ macrophages replace resident CCR2 macrophages and assume a dominant role in the decompensatory phase, promoting myocardial fibrosis and hypertrophy (121, 122). Early depletion of $CCR2^+$ macrophages during the compensatory phase may attenuate fibrosis, whereas their removal in the decompensated phase does not halt fibrosis progression, emphasizing the importance of early regulation (123, 124)). Following pressure overload, angiotensin-II activates calcium/calmodulin-dependent protein kinase IIδ (CaMKIIδ), which in turn triggers NF-κB signaling and inflammasome activation in cardiomyocytes, leading to the recruitment of $CCR2^+$ macrophages (125). NF-κB signaling in macrophages drives downstream inflammasome activation and expression of inflammatory (126, 127). In addition, aldosterone and mechanical stress in pressure overload stimulate EC to synthesize IL-6, which facilitates the recruitment of CCR2+ macrophages (128). Trans-signaling of IL-6 activates the TGF-β/Smad pathway in cardiac fibroblasts, promoting fibroblast proliferation and differentiation (129).

Overall, the diversity of macrophage phenotypes and their dynamic changes are closely related to various types and stages of CVD, including coronary artery disease, valvular heart disease, myocarditis, cardiomyopathy, HF, atherosclerosis and aneurysms. These observations highlight the importance of understanding the regulatory mechanisms of macrophages in the specific context of each disease.

1.6.3. Macrophage metabolism in cardiopulmonary disease

Upon activation, macrophages undergo metabolic reprogramming, adapting their metabolic profiles and nutrient demands to fuel the anabolic and catabolic pathways necessary for their effector functions (130, 131). In addition to meeting their own metabolic needs, macrophages contribute to systemic metabolic homeostasis by regulating essential metabolites such as iron, bilirubin, calcium, lipids, and amino acids (130). Macrophages also influence tissue metabolism by competing for and metabolizing specific substrates (132, 133). For instance, their glycolytic versus oxidative metabolic balance determines glucose uptake by EC, thereby influencing angiogenesis (134). Metabolic reprogramming reflects macrophage functional plasticity and is marked by shifts in multiple metabolic pathways, including glycolysis, oxidative phosphorylation (OXPHOS), the TCA cycle, and fatty acid oxidation (135). In MI, ischemic hearts exhibit an accumulation of the TCA metabolite citrate, which is converted to cytosolic acetyl-CoA by ATP citrate lyase (ACLY) (136). Elevated acetyl-CoA levels drive histone acetylation, inducing epigenetic modifications that regulate inflammatory gene expression. This process is associated with increased ACLY and histone acetyltransferase activity in inflammatory macrophages (137).

Other TCA intermediates, such as α-KG, fueled by glutaminolysis, serves as a substrate for 2-oxoglutarate–dependent dioxygenases (2-OGDDs), including hypoxia-inducible factor prolyl hydroxylase (HIF PHD), which suppresses hypoxia-inducible factor (HIF) levels (138). High α-KG-to-succinate ratios promote the epigenetic activation of IL-4–induced macrophage genes through histone demethylases such as Jumonji domain–containing proteins (75). Although reduced cardiac α-KG levels have been linked to myocardial ischemic injury, their specific impact on cardiac macrophages remains to be clarified (139).

Reparative macrophage metabolism integrates glycolytic and mitochondrial pathways. Glycolysis-derived lactate polarizes macrophages toward an anti-inflammatory state and preserves ventricular function post-MI (140). Fatty acids, including those derived from apoptotic cells via MerTK-dependent efferocytosis, enter mitochondria to fuel respiration and increase nicotinamide adenine dinucleotide (NAD^+) production (141). NAD^+ serves as a signaling molecule to induce pro-reparative cytokines, promoting tissue repair (142). Deficiency in mitochondrial complex I in macrophages exacerbates inflammatory responses by promoting glycolysis and increasing mitochondrial ROS production, impairing efferocytosis and hindering fibroblast activation and scar formation after MI (118).

In PH, dysregulated macrophage metabolism disrupts the balance between M1 and M2 phenotypes. This imbalance leads to the excessive release of chemokines and growth factors, accelerating the proliferation of PASMCs and promoting mesenchymal transformation of ECs. Elevated fatty acid synthase activity has been observed in the lung tissue of MCT PH model. Increased CD36 expression in M1-type macrophages within the RV leads to higher fatty acid levels and reduced fatty acid oxidation, contributing to enhanced PASMC proliferation (143).

1.7. IRG1/Itaconate axis in macrophages

A notable mitochondrial metabolite induced after injury or infection in activated proinflammatory macrophages is itaconate. In the last decade, it was discovered that the mammalian immune system produces itaconate, as evidenced by its detection in cell lysates and supernatants of LPS-stimulated macrophages and in lung extracts from mice infected with Mycobacterium tuberculosis (144-146). Subsequent studies showed that itaconate is synthesized by the decarboxylation of cis-aconitate, a citrate-derived intermediate of the TCA cycle. This process is mediated by the gene *IRG1* (immune-responsive gene 1, also known as *Acod1*), which is highly expressed in M1 macrophages following stimulation by proinflammatory signals such as LPS and IFNγ (147). Since this discovery, several regulatory functions of IRG1/Itaconate and its derivatives, including 4-octyl-itaconate (4OI) and dimethyl-itaconate, have been identified, particularly in the modulation of immune responses under proinflammatory conditions. In M1 macrophages, IRG1/Itaconate activates the nuclear factor

erythroid 2-related factor 2 (NRF2), an important regulator of cellular redox balance. This activation occurs primarily through the modification of cysteine residues on Kelch-like ECH-associated protein 1 (KEAP1). These modifications lead to the degradation of KEAP1 and thus prevent NRF2 from being targeted by KEAP1 for proteasomal degradation (148). In addition, IRG1/Itaconate affects cell metabolism primarily by inhibiting succinate dehydrogenase (SDHA) and glyceraldehyde-3-phosphate dehydrogenase (GAPDH), which not only interrupts the TCA cycle and increases succinate levels, but also suppresses glycolysis (149, 150). In addition, itaconate plays an epigenetic role by modulating the DNA methylation profile of M1 macrophages through direct interaction with DNA demethylating enzymes, Ten-Eleven Translocation (TET) family proteins, resulting in inhibition of their activity (151). Conversely, anti-inflammatory M2 macrophages neither express *IRG1* nor produce itaconate, a regulation influenced by PPARγ and the miR-93/ Interferon Regulatory Factor 9 (IRF9) axis. This suggests that IRG1/Itaconate serves as a suppressor of the anti-inflammatory M2 phenotype (152). Indeed, 4OI has been shown to reprogram anti-inflammatory M2 macrophages into a proinflammatory phenotype by inhibiting the Janus kinase 1 (JAK1)/STAT6 signaling pathway, which is essential for maintaining the anti-inflammatory response of M2 macrophages (153). Recent evidence shows that macrophages can secrete itaconate, which is subsequently taken up by cancer cells and hepatocytes via the SLC13A3 transporter (154, 155). These observations suggest an extracellular regulatory role for itaconate as a metabolic messenger that shapes the immune microenvironment in different tissues and disease contexts.

Given the significant contribution of macrophage metabolic reprogramming to the damaging and reparative processes in cardiopulmonary diseases, understanding the metabolic signatures associated with these states is critical. Disturbances in intracellular metabolism can lead to abnormal macrophage activation and phenotype imbalance. Despite extensive research on macrophages in CVD and PH, the role of the TCA metabolite itaconate in these diseases remains underexplored. Therefore, in this thesis, we aim to investigate the contribution of the IRG1/itaconate axis in cardiopulmonary disease, focusing on its potential role in PH.

2. Aims of the study

Macrophages originating from BM niches show remarkable plasticity and adapt their phenotype to the local microenvironment. In proinflammatory macrophages, the IRG1/Itaconate axis has been identified as a central signaling pathway for regulating immune responses and maintaining cellular homeostasis. Considering that BM niches, as primary sources of macrophages, are highly sensitive to inflammatory signaling and contribute to systemic pathology, their role in inter-organ communication between BM, heart and lung is particularly relevant in diseases such as PH. We hypothesize that the IRG1/Itaconate axis mediates protective communication between the BM, heart and lung organs that influences the phenotype of HSCs and downstream cardiopulmonary homeostasis.

To evaluate this hypothesis, the following objectives were investigated:

1- Baseline assessment of structural and functional parameters in the heart and lungs of *Irg1*-knockout (*Irg1*$^{-/-}$) mice.

2- Immune profiling of heart, lung and BM of *Irg1*$^{-/-}$ mice.

3- Investigation of PH development in *Irg1*$^{-/-}$ mice under hypoxia.

4- Evaluation of the paracrine effects of IRG1-deficient macrophages on the phenotype of pulmonary vascular and cardiac cells.

5- Exploring Irg1-deficient HSCs differentiation phenotype and their molecular signature.

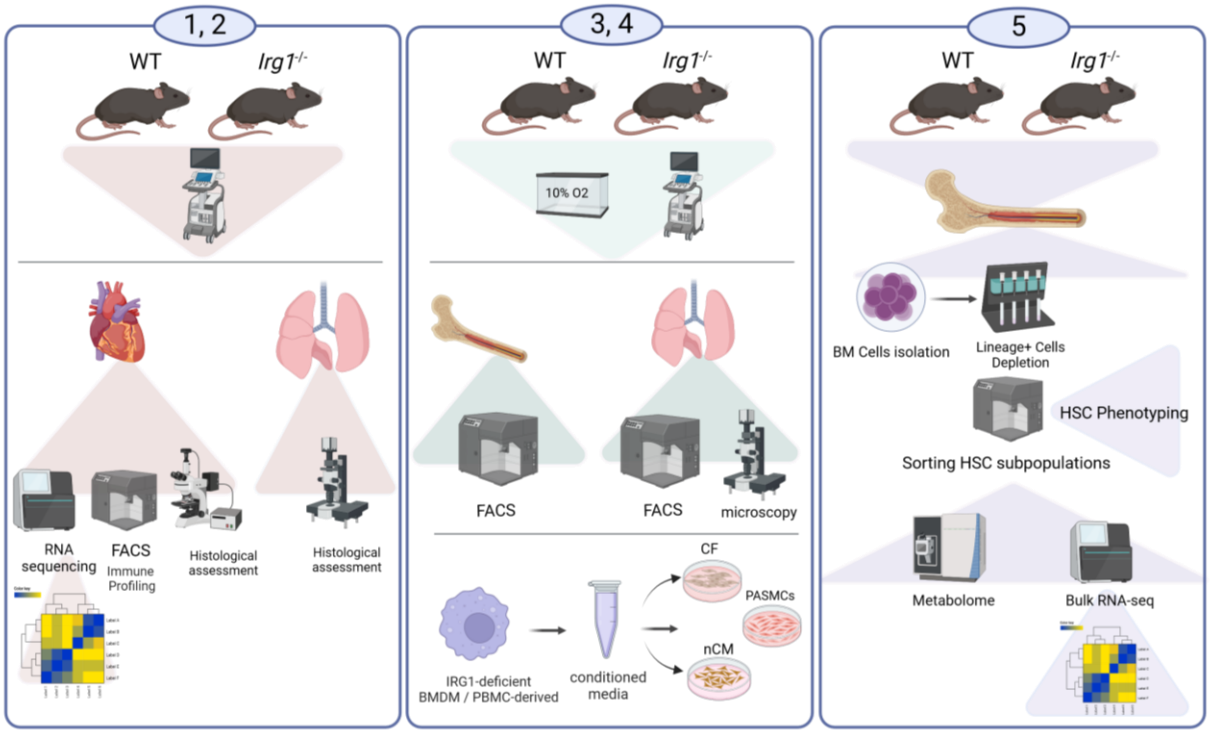

Figure 2.1: Schematic representation of objectives of my thesis. Created with BioRender.com.

3. Materials and methods

3.1. Materials

Table 3.1.1. Reagents and chemicals

Reagent	Company
4′,6-Diamidin-2-phenylindol (DAPI)	Invitrogen, USA
Acetic acid, glacial	Sigma, USA
Acetone	Carl Roth, Germany
Acrylamide solution (30%)	Sigma Aldrich, USA
Agarose, low gelling temperature, Type VII	Sigma Aldrich, USA
Ammonium Persulfate (APS)	Sigma Aldrich, USA
Bovine serum albumin (BSA)	Carl Roth, Germany
Bromophenol blue	Roche, Germany
BSA solution (2mg/ml)	BioRad, USA
β mercaptoethanol	Sigma Aldrich, USA
Chloroform	Carl Roth, Germany
Citrate buffer	Life technologies, USA
Dako Fluorescence Mounting Media	Dako, Denmark
Dimethyl sulfoxide	Sigma Aldrich, USA
Diphenylacetohydroxamic acid	Sigma Aldrich, USA
DirectPCR® lysis reagent	Peqlab, Germany
Di-sodium hydrogen phosphate	Carl Roth, Germany
DNA ladder	Fermentas, USA
Ethanol absolute	Carl Roth, Germany
Ethidium Bromide	Carl Roth, Germany
Ethylenediamine-Tetraceticacid (EDTA)	Carl Roth, Germany
Ferric-hematoxylin A	Waldeck, Germany
Ferric-hematoxylin B	Waldeck, Germany
Fluorescence mounting medium	Dako, USA
Halt™ protease and phosphatase inhibitor cocktail	Thermo Fisher Scientific, USA
Hanks' Balanced Salt solution	Thermo Fisher Scientific, USA
Hematoxylin Solution	Life technologies, USA
Hydrochloric acid	Carl Roth, Germany
Hydrogen peroxide	Merck, Germany
Isopropanol	Carl Roth, Germany
Mayer's Hematoxylin Solution	Sigma Aldrich, USA
Methanol	Carl Roth, Germany

Reagent	Company
Methyl-green	Vector, USA
Milk powder	Carl Roth, Germany
N,N,N´,N´-Tetramethyl diaminomethane (TEMED)	Sigma Aldrich, USA
Page Ruler Prestained Protein Ladder	Thermo Scientific, USA
Paraformaldehyde	Carl Roth, Germany
Pertex Mounting Medium	Medite, Germany
Picric acid	AppliChem, Germany
Ponceau S Solution	Sigma Aldrich, USA
Potassium chloride	Carl Roth, Germany
Potassium dihydrogen phosphate	Carl Roth, Germany
Proteinase K	Peqlab, Germany
1x protease and phosphatase inhibitor cocktail	Thermo Scientific, USA
RIPA lysis buffer	Santa Cruz Biotechnology, USA
Rainbow protein molecular weight marker	AmershamBiosciences, USA
RNase Away	Invitrogen, USA
Scott′s Tap Water Substitute Concentrate 10X	Sigma Aldrich, USA
Sodium bicarbonate	Carl Roth, Germany
Sodium chloride	Carl Roth, Germany
Sodium dodecylsulfate (20% w/v)	Carl Roth, Germany
Sodium hydroxide	Carl Roth, Germany
Stripping Buffer	Thermo Scientific, USA
SYBR green mix	Applied Biosystems
Tetramethylrhodamine methyl ester (TMRM)	Invitrogen, USA
Tris 0.5 M (pH 6.8)	Amresco, Germany
Tris 1.5M (pH 8.9)	Amresco, Germany
Tris base	Sigma Aldrich, USA
Triton X-100	Carl Roth, Germany
TRIzolTM	Thermo Fisher Scientific, USA
Trypsin Concentrate and Diluent	Life technologies, USA
Tween 20	Sigma, USA
Xylol	Carl Roth, Germany

Table 3.1.2. List of the equipment used

Equipment	Company
Agarose electrophoresis chambers	BioRad, USA
Cell culture incubator, Hera cell	Heraus, Germany
Centrifuge	Thermo Scientific, USA
StepOnePlus™ Real-Time PCR System	Thermo Scientific, USA
Whitley H35 Hypoxystation	Don Whitley Scientific Ltd, UK
All-in-One Fluorescence Microscope (BZ-X series)	Keyence Corporation, USA
Fluorescence microscope Leica DM 2500	Leica, Germany
ImageQuant LAS 4000	GE Healthcare, UK
Leica DM 6000B	Leica, Germany
Microplate reader Infinite 200	TECAN, Germany
NanoDrop2000 Spectrophotometer	Thermo Scientific, USA
PCR thermocycler T3000	Biometra, Germany
Power supply	BioRad, USA
PowerLab	AD Instruments, Australia
Precellys Homogenizer	PeQLab, Germany
Nanozoomer 2.0 HT	Hamamatsu, Japan
Water bath (cell culture)	Heraeus, Germany
Western blot chambers	BioRad, USA
Cryostar NX50	Thermo Scientific, USA
Leica RM2255 Rotary Microtome	Leica, Germany
Leica EG1160 Tissue Embedding Station	Leica, Germany
ASP200S Advanced Smart VacuumTissue Processor	Leica, Germany
VisualSonics VEVO 1100	FujiFilm, Canada
MPVS Ultra Pressure-Volume Unit from Millar	AD Instruments, New Zealand
Q Exactive Orbitrap Mass Spectrometer	Thermo Scientific, USA
gentleMACS DIssociators	Miltenyi Biotec
FACS Symphony A5SE flow cytometer	BD Biosciences
micromanometer/Mikro-Tip Pressure catheter	Millar Instruments
NextSeq2000	Illumina
RS-2000 Biological Irradiator	Rad Source Technologies, USA

Table 3.1.3. Kits used

Kit	Company
High Capacity cDNA synthesis kit	Applied Biosystems, USA
DC Protein assay kit	BioRad, USA
BrdU Incoportation assay kit	Roche, Germany
In situ cell death detection kit	Roche, Germany
DAB substrate kit	Vector, USA
Neonatal Heart Dissociation Kit	Miltenyi Biotec
Neonatal Cardiomyocyte Isolation Kit	Miltenyi Biotec
Multi Tissue Dissociation Kit 2	Miltenyi Biotec
miRNeasy Micro Kit	Qiagen
MART-Seq® v4 Ultra® Low Input RNA Kit	Takara Bio
Trichrome staining with Aniline Blue kit	Morphisto, Germany

Table 3.1.4. Cell Culture medium and reagents

Culture medium	Company
Dulbecco's Phosphate Buffer saline (DPBS)	Sigma, USA
Fetal calf serum (FCS)	PAA, USA
Human Pulmonary arterial smooth muscle cells (PASMCs)	Lonza, USA
Human cardiac fibroblasts (CF)	ScienCell, USA
OptiMEM	Gibco, USA
Penicillin/Streptomycin	Lonza, USA
Smooth muscle cell medium (SmGM)	Lonza, USA
Fibroblast Growth Medium	ScienCell, USA
Trypsin/EDTA	Lonza, USA
DMEM GlutaMAX	BD Biosciences, Germany
RPMI 1640	Gibco life technologies, USA
Gelatin	Sigma-Aldrich, Germany

3.2. Methods

3.2.1. Cell isolation, differentiation and culture

3.2.1.1. Culturing of human pulmonary arterial smooth muscle cells

PASMCs were cultured in 10 cm Petri dishes containing 8 mL of PASMC growth medium. Cells were maintained in a humidified incubator at 37°C with 5% CO_2. When cells reached 90–95%

confluence, they were passaged at a 1:3 ratio and used for experiments at passage 6. For passaging, culture dishes were rinsed with 8 mL of DPBS and incubated with 3 mL of Trypsin/EDTA for 3 to 4 minutes. Cell detachment was confirmed under a microscope. The trypsinization was neutralized by adding an equal volume of growth medium. Cells were transferred to 50 mL falcon tubes and centrifuged at 1,350 rpm for 7 minutes. The supernatant was discarded, and the cell pellet was gently resuspended in 1 mL of PASMC growth medium before seeding into new culture dishes.

3.2.1.2. Human cardiac fibroblast culture

Human cardiac fibroblasts (CFs) provided by ScienCell company were cultured on dishes coated with poly-lysine (1:1000 in double distilled water) using a fibroblast medium enriched with FBS, FGS, penicillin, and streptomycin (2301, ScienCell, USA). The cells were kept in a 5% CO2 incubator at 37 °C. Experiments were conducted using the cells between passages 5 and 6. Upon 24-hr serum starvation using a basal medium with penicillin containing 0.1% fetal calf serum (FCS, 10500064, Gibco® life technologies, NY, USA), CFs were treated with CM of donor pro-inflammatory Macrophages transfected with Scramble or si-*Irg1* for 24 hr.

3.2.1.3. Macrophage differentiation and polarization

The blood samples were provided by Lung Center blood bank at the Universities of Giessen and Marburg according to ethical approval from the Ethics Committee, under file number AZ 58/15. Human Macrophage were derived from peripheral blood mononuclear cells (PBMCs), following the protocol outlined in previous studies (Sarode, Zheng et al. 2020; Karger, Mansouri et al. 2023). PBMCs were extracted from buffy coats, utilizing Ficoll density gradient centrifugation. 15 ml of Ficoll-Paque media (L6115, BIOCOLL Biochrom AG, Germany) was added to Leucosep centrifuge tubes (227290, Greiner Bio-one, Germany), and the blood samples were gently layered onto the media, followed by centrifugation for 35 minutes at 440 g without applying brakes. Then the upper white layer containing PBMCs was carefully transferred to a fresh 50 ml Falcon tube. To remove red blood cells (RBCs) and platelets, two rounds of washing were performed with using lysis buffer (555899, BD Biosciences, Germany) and DPBS, respectively. PBMCs were then seeded into 6-well plates (83.3920.300, Sarstedt, Germany) in RPMI 1640 medium (21875034, Gibco® life technologies, USA) with 1% (v/v) penicillin/streptomycin (P/S) (15140122, Gibco® life technologies, USA). Non-adherent cells were washed away after a 2-hour (hr) incubation, and the adherent cells were cultured to differentiate into Macrophage over a period of 10 days using macrophage complete medium (RPMI 1640 supplemented with 2% (v/v) human serum and 1% (v/v) P/S). To polarize Macrophage to M1, the cells were treated with LPS (100 ng/ml; L5418, Sigma-Aldrich, USA) and IFNγ (100 U/ml; 285-IF, R and D Systems, USA) for 24 hr.

3.2.1.4. Murine macrophage differentiation

Mouse BM cells were used for differentiating to mouse Macrophage, known as bone BMDM After steriliz the mice skin with 80% ethanol, the tibia and femur were dissected from both legs and transferred to cold PBS. Subsequently, the bones were flushed with 15 ml RPMI 1640 medium containing 1% (v/v) P/S. The flushed cells were passed through a 40-µM cell strainer (CLS431750-50EA, Merck, Germany) and centrifuged at 500 g for 10 minutes. The cell pellet was resuspended in RPMI 1640 medium supplemented with 10% (v/v) FCS, 1% (v/v) P/S, and mouse Macrophage colony-stimulating factor (M-CSF, 20 ng/ml; 416-ML, R and D System, USA). Cells were then seeded into a six-well plate and cultured for 5-6 days, with the medium changed every 2 days, resulting in differentiation into Macrophage. For mouse Macrophage polarization to M1, LPS (100 ng/ml) treatment was done for 24 hr. Before harvesting the macrophages, their conditioned medium was collected. Snap-frozen, and kept in -80 for future experiments.

3.2.1.5. Neonate cardiomyocyte isolation and culture

Neonatal hearts were isolated from P0 to P3 WT C57bl/6 pups. Initially, the pups were decapitated using sterile scissors (straight), and the chest was opened along the sternum to allow access to the chest cavity and the heart. The aortic root and atria were physically removed before isolation. The extracted hearts were immediately transferred into the 10-cm dish containing 1x PBS (without Ca2+, Mg2+). The harvested hearts belonging to the pups (n: 7-10) from the same littermates were pulled and dissociated using mouse and rat Neonatal Heart Dissociation Kit (130-098-373, Miltenyi Biotec, Germany), according to manufacturer´s instructions. Briefly, the harvested hearts from the same littermate were transferred into the gentleMACS C Tube (Miltenyi Biotec, Germany) containing 2.5 ml of enzyme mixture. The tissue dissociation was done by gentleMACS Octo Dissociator (Miltenyi Biotec, Germany). After detaching the C Tube from the dissociator, 7.5 mL of DMEM GlutaMAX™ (31966021, BD Biosciences, Germany) supplemented with 10% FCS and 1% P/S was added to the dissociated cells. The resulting cell suspension was then filtered through a 70 µm MACS SmartStrainer (130-110-916, Miltenyi Biotec, Germany). Following centrifugation, RBCs were lysed by adding 5 µL of lysis buffer (12770000, Invitrogen, USA). Neonatal cardiomyocytes (nCMs) were isolated using the Mouse Neonatal Cardiomyocyte Isolation Kit (130-100-825, Miltenyi Biotec, Germany) according to the manufacturer's protocol. Non-target cells were depleted through magnetic labeling with a cocktail of monoclonal antibodies conjugated to MACS® MicroBeads. The labeled non-target cells were retained in a MACS Column (130-042-401, Miltenyi Biotec, Germany) within the magnetic field of a MACS Separator, allowing the unlabeled cardiomyocytes to pass through and be collected. Subsequently, nCMs were plated

on 6-well plates coated with 1% gelatin (G939, Sigma-Aldrich, Germany) dissolved in PBS and cultured in DMEM with 10% FBS and 1% P/S for 48 hr. For experimental purpose nCMs were treated with CM of WT or *Irg1*$^{-/-}$ BMDM for 24 hr then the cells were harvested for RNA isolation.

3.2.1.6. siRNA transfection

IRG1 was silenced in Macrophages using two distinct siRNAs, in a serum-free Opti-MEM medium (11058021, Sigma-Aldrich, Germany) and HiPerFect transfection reagent (371707, Qiagen, Germany), following the manufacturer's protocol. The siRNAs, listed in Table 3.2.1, were all sourced from Qiagen (Qiagen, Hilden, Germany). The HiPerFect reagent was first combined with Opti-MEM and briefly vortexed, after which the siRNAs were added, mixed thoroughly, and allowed to incubate at room temperature (RT) for 5–10 minutes. Meanwhile, the medium of Macrophages was removed and the transfection mix was dropwise applied to the cells. Following 6 hr incubation of the cells with the transfection mixture, 1.5 ml of complete medium was added, and the cells were incubated for an additional 24 or 48 hr. After 24 hr of transfection, macrophages were polarized to the M1 phenotype by 24-hr treatment with LPS (100 ng/µl) and IFN-γ (100 International unit (IU)/ µl).

Table 3.2.1. Custom siRNAs used for knockdown of the *IRG1*

Target RNA	siRNA name	Catalog Nr.	Company	Final con.
Negative control	AllStars negative	1027292	Qiagen	25nM
IRG1	Hs_IRG1_4	SI05379920	Qiagen	25nM
IRG1	Hs_IRG1_3	SI05172685	Qiagen	25nM

3.2.1.7. Cellular functional assays

For cellular functional assays, the cells were seeded at a density of 6,000 cells per well in 96-well plates. The next day, the cells were serum starved for 24 hr and then were incubated with various macrophage conditioned media (CM), as indicated in the results section, for an additional 24 hr.

3.2.1.7.1. Cell proliferation assay

Cell proliferation was measured using cell proliferation assay kit (11647229001, Roche Diagnostics GmbH, Germany), a colorimetric immunoassay that quantifies BrdU incorporation during DNA synthesis, following the manufacturer's instructions. Initially, the cells were exposed to BrdU labeling solution and incubated at 37°C in an atmosphere of 5% CO2 for 90 minutes. Following this, the labeling medium was replaced with 200 µl per well of FixDenat solution, and incubation was conducted for 30 minutes at room temperature. The solution was then removed by gently tapping the wells, and 100 µl per well of anti-BrdU-POD solution (diluted 1:100) was added. Incubation was performed for 2 hr at room temperature in the dark.

Afterward, the antibody conjugate was removed by stripping, and the wells were washed three times with 300 µl per well of wash solution. Finally, 100 µl per well of substrate solution was added, and absorbance was measured at 370 nm, with a reference wavelength of 492 nm, using the infinite M200 PRO plate reader (Tecan Group, Maennedorf, Switzerland).

3.2.1.7.2. Cell apoptosis assay

Cell apoptosis was assessed using a cell death detection kit (11920685001, Roche Diagnostics GmbH, Germany), according to the manufacturer's protocol. After the cells were treated, they were centrifuged at 200 g for 10 minutes, and the supernatant was removed. A total of 200 µl of 1x lysis buffer was added to each well, followed by a 30-minute incubation. After lysis, the cells were centrifuged again at 200 g for 10 minutes to pellet the debris. Then, 20 µl of the supernatant was transferred into streptavidin-coated wells provided in the kit. To each well, 80 µl of freshly prepared immunoreagent was added, and the plate was shaken at 300 rpm for 2 hr in the dark. The solution was removed by tapping, and the wells were rinsed three times with 200 µl of incubation buffer. After the final wash, 100 µl of ABTS solution was added to each well. Absorbance was recorded at 405 nm, with a reference wavelength of 490 nm, using the infinite M200 PRO plate reader (Tecan Group, Switzerland).

3.2.2. Molecular biology methods

3.2.2.1. RNA isolation

Total RNA extraction was conducted using miRNeasy Micro Kit (Qiagen, 217084, Germany) according to the kit protocol. Upon washing the adherent cells with PBS, 700 µl of QIAzol (Qiagen, 79306, Germany) Lysis Reagent was added to the cells and the cells were disrupted by scraping. Cell lysates were transferred into separate tubes. Subsequently, 140 µl of chloroform was added to each sample, followed by vigorous shaking for 15 seconds. The mixture was incubated at RT for 2 minutes and then centrifuged at 12,000 g at 4°C for 15 minutes. Following centrifugation, upper aqueous phase was collected into a new tube, avoiding any contamination from the lower layers. To precipitate RNA from the aqueous phase, 450 µl of 100% ethanol was added per 300 µl of the aqueous phase and thoroughly mixed by pipetting. The mixture was applied to the RNA isolation column included in the kit. The columns were centrifuged at 9,000 g for 15 seconds at RT, and the flow-through was discarded. Following two-times washing of the columns with the wash buffers provided in the kit, a final wash was done with 80% ethanol. Each washing step, except the final one with 80% ethanol (which lasted 2 minutes), was performed at 9,000 g for 15 seconds at RT. The columns were then dried by centrifugation at 9,000 g for 5 minutes at RT. Finally, RNA was eluted by adding 14 µl of RNase-free water to the column and centrifuging in full speed for 1 minute at RT. The

RNA concentration and its purity were measured using a spectrophotometer (ThermoFisher Scientific, USA), and the samples were stored at -80°C for long-term.

3.2.2.2. Complementary DNA synthesis

The concentration and purity of RNA were determined using Nanodrop (Thermo Scientific). The High-Capacity cDNA Reverse Transcription Kit (4368814, Applied Biosystems, USA) was used to transcribe the RNA into complementary DNA (cDNA), according to the manufacturer's instructions. The reaction solution protocol and temperature programs used for cDNA synthesis are listed in Tables 3.2.2 and 3.2.3., respectively.

Table 3.2.2. Reaction mix for reverse transcription

Reagent	Volume [µl]
RNA template	1 µg in 10 µl RNase free water
10x RT Buffer	2
10x RT Random Primer	2
dNTPs (100 mM)	0.8
MultiScribe Reverse Transcriptase (50 U/µl)	1
RNase Inhibitor (20 U/µl)	0.5
RNase free water	3.7

Table 3.2.3. Reverse transcription program

Time	Temperature
10 min	25 °C
120 min	37 °C
5 min	85 °C
∞	4 °C

3.2.2.3. Quantitative polymerase chain reaction

Quantitative polymerase chain reaction (qPCR) was performed with StepOnePlus™ real-time PCR systems (A25742, Applied Biosystems, USA) using the cDNA in reaction mixture (table 3.2.4) according to the qPCR protocol mentioned in (table 3.2.5). For comparison of expression levels, Ct values of the gene of interest were normalized to the housekeeping gene, Hypoxanthine-guanine phosphoribosyl transferase 1 (HPRT1) using the equation ΔCt = Ct (reference gene) – Ct (gene of interest). To exclude the presence of any extraneous nucleic acid contamination in the PCR reaction, a negative technical control containing RNase-free water in place of cDNA template was included in each qPCR run. To further assess the efficiency of the qPCR, we performed a melt curve analysis in each run to confirm that the

amplicon produced a single peak. The primer sequences of each gene of interest were designed using sequence information from the National Center for Biotechnology Information database and purchased from Metabion, Germany (table 3.2.6).

Table 3.2.4. qPCR reaction mixture

Reagent	Volume [µl]
Template cDNA (1:20 dilution)	4
SYBR green mix (Applied Biosystems)	5
Forward primer (10 µM)	0.5
Reverse Primer (10 µM)	0.5

Table 3.2.5. qPCR protocol

qPCR steps	Temperature	Time	Number of cycles
Initial denaturation	95°C	3 min	1
Denaturation	95°C	10 sec	40
Annealing	60°C	30 sec	
Elongation	72°C	30 sec	
Final elongation	95°C	10 sec	5 min
Melting curve	65°C to 95°C	0.5°C increase/sec for 5 sec	1

Table 3.2.6. qPCR primer list

Species	Gene	Sequence (5`–3`)	
Human	*HPRT*	FP	TGACACTGGCAAAACAATGCA
		RP	GGTCCTTTTCACCAGCAAGCT
	TNFα	FP	GAGGCCAAGCCCTGGTATG
		RP	CGGGCCGATTGATCTCAGC
	IRG1	FP	GAGAGAGCCCTGCTTCCAAC
		RP	TGGCCTGTTGATCTGGCATT
	IL6	FP	AGCCAGAGCTGTGCAGATGAG
		RP	TGGCATTTGTGGTTGGGTC
	IL1 β	FP	CTAAACAGATGAAGTGCTCC
		RP	GGTCATTCTCCTGGAAGG
	POSTN	FP	TGATGGAGTGCCTGTGGAAA
		RP	CTTCCTCACGGGTGTGTCTC
	COL3A1	FP	TGGGAGAAATGGTGACCCTGG
		RP	CCAGGATAGCCTGCGAGTCCT
Mouse	*Hprt*	FP	GCTGACCTGCTGGATTACAT
		RP	TTGGGGCTGTACTGCTTAAC
	Tnfα	FP	CATCTTCTCAAAATTCGAGTGACAA
		RP	TGGGAGTAGACAAGGTACAACCC
	Il6	FP	TCTCTGCAAGAGACTTCC
		RP	AGTAGGGAAGGCCGTGGTTGT
	Il1β	FP	TGGCAACTGTTCCTG

		RP	GGAAGCAGCCCTTCATCTTT
	Myh6	FP	TCCAAGTTCCGCAAGGTGCAG
		RP	ATTGGCCACAGCGAGGGTCT
	Myh7	FP	GGAGCAGGCCAACACCAACC
		RP	GGCACCCTTGGAGCTGGGTA
	Anp	FP	CAGCTGCTTCGGGGGTAGGA
		RP	CCAAGCTGCGTGACACACCA
	Bnp	FP	CGGGTCCAGCAGAGACCTCA
		RP	CTGGGGAAAGAGACCCAGGCA
	Jmjd3	FP	TCTGCTGTAACCCACTGCTG
		RP	AGCCAATCATCACCCTTGTC

3.2.2.4. RNA-Sequencing

RNA was isolated by miRNeasy micro Kit (Qiagen) combined with on-column DNase digestion (RNase-Free DNase Set, Qiagen) to avoid contamination by genomic DNA. RNA and library preparation integrity were verified with LabChip Gx Touch (Perkin Elmer).

3.2.2.5. Library Construction

RNA amounts were normalized and 1µg of total RNA of RV and LV samples was used as input for VaZyme_VAHTS Universal Stranded mRNA-seq - V6 (Vazyme). For RNA samples of both HSCs subpopulations, following normalization of RNA amounts, 10 ng of total RNA was used as input for SMART-Seq® v4 Ultra® Low Input RNA Kit following manufacture's protocol (Takara Bio). Sequencing was performed on the NextSeq2000 platform (Illumina) using P3 flowcell with 72bp single-end setup.

3.2.2.6. RNA-Seq data analysis

Trimmomatic version 0.39 was employed to trim reads after a quality drop below a mean of Q15 in a window of 5 nucleotides and keeping only filtered reads longer than 15 nucleotides (156). Reads were aligned versus Ensembl mouse genome version mm39 (Ensembl release 109) with STAR 2.7.11a (157). Alignments were filtered to remove duplicates with Picard 3.0.0 (Picard: A set of tools (in Java) for working with next generation sequencing data in the BAM format), multi-mapping, ribosomal, or mitochondrial reads. Gene counts were established with featureCounts 2.0.4 by aggregating reads overlapping exons excluding those overlapping multiple genes (158). The raw count matrix was normalized with DESeq2 version 1.36.0 (159). Contrasts were created with DESeq2 based on the raw count matrix. Genes were classified as significantly differentially expressed at average count > 5, multiple testing adjusted p-value < 0.05, and -0.585 < log2FC > 0.585. The Ensemble annotation was enriched with UniProt data (Activities at the Universal Protein Resource (UniProt)). All downstream analyses are

based on the normalized gene count matrix. Volcano and MA plots were produced to highlight DEG expression. A global clustering heatmap of samples was created based on the Euclidean distance of regularized log transformed gene counts. Dimension reduction analyses (PCA) were performed on regularized log transformed counts using the R packages FactoMineR (160). DEGs were submitted to gene set overrepresentation analyses with KOBAS (161).

3.2.2.7. Protein extraction

To extract the protein from cells, MQs, nCMs and CFs were lysed in RIPA lysis buffer (sc-249482, Santa Cruz Biotechnologies, USA) supplemented with 1x protease and phosphatase inhibitor cocktail (78440, Thermo Scientific, USA). Heart tissue was homogenized using a Precellys homogenizer (PeQLab, Germany) in 500 µl of RIPA buffer supplemented with a protease/phosphatase inhibitor cocktail. Following 10 minutes incubation on ice, the samples were centrifuged at 14,000 rpm for 20 minutes at 4°C. The separation containing protein was carefully transferred to a fresh 1.5 ml Eppendorf tube and kept on ice. Quantification of proteins was performed using a modified Lowry assay and the DC™ Protein Assay Kit (5000122, Bio-Rad, Germany). A range of protein standards, from 0.125 to 2 µg/µl, was prepared using varying concentrations of bovine serum albumin (BSA). Protein concentration was measured at a wavelength of 750 nm using a microplate reader (Infinite M200 PRO, Tecan Group, Switzerland). The concentrations were then equalized across all samples, which were subsequently mixed with 5x sodium dodecyl sulfate (SDS) (1057.1, Roth, Germany) and boiled at 95°C for 3-5 minutes.

3.2.2.8. Western blotting

Depending on the size of target protein, equal amounts of the samples were loaded in 6%, 10% or 15% SDS-polyacrylamide gels (Table 3.2.7) and placed in running buffer. Then the protein samples were transferred to polyvinylidene difluoride membranes (PVDF) (1620264, Bio-Rad, USA) in blotting buffer (Table 3.2.8), with the transfer time for 1h and 25 min at 100 V. After blocking the membranes for 1h in 5% milk in TBST, formulated as 20 mM Tris (4855.2, Carl Roth, Germany), 150 mM NaCl (3957.1, Carl Roth, Germany) and 0.1% (w/v) Tween®-20 (P1379, Sigma, USA) detergent, they were incubated with a primary antibody diluted 1:1000 in 5% (w/v) BSA/TBST with constant shaking overnight at 4°C. After proper washing with TBST, the blots were incubated with appropriate horseradish peroxidase (HRP)-conjugated secondary antibodies in 5% milk in TBST buffer, followed by detecting protein-antibody conjugates with SuperSignal West Femto Chemi-luminescent Substrate (34095, Thermo Scientific, USA) and capturing the signal using an Image reader (GE Healthcare). Densitometry analysis of the blots was performed using ImageJ software, normalizing to β-actin, heat shock protein 90 (HSP90) or). Details of the antibodies can be found in Tables 3.2.9 and 3.2.10.

Table 3.2.7. Gel composition

Gel Component	Percentage of gel	
	6% (Stacking gel)	10% (Resolving gel)
30%	0.625 mL	1.5 mL
Tris-HCL	0.5 mL	2 mL
SDS 10%	25 µL	60 µL
APS 10%	12.5 µL	30 µL
TEMED	2.5 µL	6 µL
Water upto final volume	1.3 mL	2.4 mL

Table 3.2.8. Running and blotting buffers composition

Components	Running buffer	Blotting buffer
Tris	25 mM	50 mM
Glycin	250 mM	40 mM
SDS 10% (w/v)	0.10%	-
Methanol (v/v)	-	20%
Water	Up to final volume	Up to final volume

Table 3.2.9. Primary antibodies used for western blotting

Antibody	Reference	Company
Beta-actin	A2228	Sigma
GAPDH	MA5-15738	Invitrogen
JMJD3/KDM6B	ab38113	Abcam
HSP90	4877	Cell Signaling
IRG1	17805	Cell Signaling
COL3A1	sc-271249	Santa Cruz
Endothelin-3	sc-81944	Santa Cruz

Table 3.2.10. Secondary antibodies used for western blotting

Antibody	Reference	Company
Anti-Mouse IgG-Peroxidase conjugated	A9044	Sigma
Anti-Rabbit IgG-Peroxidase conjugated	A0545	Sigma

3.2.3. Animal experiments

All mice, including C57Bl/6J, *Irg1*$^{-/-}$ strain, were housed under specific pathogen-free conditions with free access to water and food. They were kept at a controlled temperature of 22°C and maintained on a standard 12-hr light-dark cycle throughout the experimental period. The handling of the mice adhered to the European Union Commission guidelines for laboratory animals. The animal experiments conducted as part of this study were approved by the local authorities (Regierungspraesidium Darmstadt, Hessen, Germany, animal proposal: B2-2000). For our experiments, we used C57BL/6 mice aged 8 to 12 weeks.

3.2.3.1. Genotyping

Genomic DNA was extracted from ear punch samples by incubating them in a Tris-EDTA buffer (pH 8) containing 0.5% SDS and 20 mg/ml Proteinase K at 56°C for a minimum of 6 hr. After incubation, the samples were centrifuged, and the resulting supernatant, which held the genomic DNA, was diluted for use in downstream applications. Genotyping was conducted via PCR, with all reactions utilizing KAPA2G Fast ReadyMix (2GFRMKB, Sigma, USA), as detailed in table 3.2.11.

Table 3.2.11. Master mixture material for genotyping PCR

Reagent	Volume [µl]
H_2O	6
KAPA2G Fast ReadyMix	12
$MgCl_2$	0.5
Primer 1	1.25
Primer 2	1.25
Primer 3	1.25
DMSO	1.25
Template	1

The primer list used for *Irg1*$^{-/-}$ genotyping and The PCR product detected by Qiaxel (Qiagen, Hilden, Germany) are provided in Table 3.2.12, respectively. The PCR product was detected by Qiaxel. The PCR reaction program can be found on table Table 3.2.13.

Table 3.2.12. Genotyping primer list and PCR product for *Irg1*$^{-/-}$ mice.

Primer	Sequence 5' --> 3'
Common-Forward	GTGGGGAGGGGAACTATGAG
Irg1 WT-Reverse	ATTTGGAGGAACCCCATGAC
Irg1 mutant-Reverse	CAGCCTCTAAGCCAGACAGC

*(L) ladder, (1-4) Irg1-/-, (n) negative control

Table 3.2.13. PCR reaction for *Irg1*$^{-/-}$ mice

Temperature	Time	Cycle
95°C	5 minutes	1
95°C	20 seconds	35
64°C	30 seconds	
72°C	15 seconds	
72°C	10 minutes	1
4°C	∞	1

3.2.3.2. Hypoxia mouse model

To induce PH in mice, C57BL/6J WT and *Irg1*$^{-/-}$ mice (n = 7 per group) were exposed to chronic hypoxia (10% oxygen) for 35 days, following a protocol widely used in studies of hypoxia-induced PH. At the end of hypoxia exposure, echocardiography and hemodynamic measurements were performed. Following this the mice was euthanized and the organs were harvested for further analysis. The left lung was perfused with 4% paraformaldehyde (PFA), excised, and subsequently fixed in 4% PFA for histological analysis. Two lobes of the right lung were used for tissue dissociation for fluorescence-activated cell sorting (FACS) analysis. The remaining right lobe was snap-frozen and stored at -80°C for molecular biology studies, including gene expression and protein analysis.

3.2.3.3. Bone marrow transplant mouse model

The C57BL/6 WT recipient mice were initially exposed to radiation using the RS-2000 Biological Irradiator from Rad Source Technologies, Inc., Alpharetta, GA, USA. The radiation dose was calibrated for the cage area (Special Cage Irradiator) to ensure a consistent delivery of 19.5 mGy/sec or 1.17 Gy/min across the cage. The mice underwent irradiation for a total of 483 seconds, receiving a cumulative dose of 9.5 Gy. Following this, recipient mice were given an intravenous infusion of 1.5-2x10^{7} BM cells sourced from *Irg1*$^{-/-}$ donor mice. Prior to harvesting BM, donor mice were intraperitoneally injected with 500 units of heparin and euthanized using a lethal dose of ketamine and xylazine (1:1:2 ratio). Following dissection of the femurs and tibias, the BM cells were flushed out using RPMI 1640 medium supplemented with 1% P/S. After centrifugation, the cells were resuspended in fresh medium, filtered through a 40µm cell strainer, counted and prepared for transplantation into the irradiated recipient mice. Each recipient mouse was intravenously injected with 3×10^{6} cells suspended in 100µL of PBS. The mice were positioned prone in a mouse box with tail access and up to 200µL of the cell suspension was injected into the tail vein of the C57BL/6 recipients, whose tails had been pre-warmed using a red light lamp. The mice's immune systems were then allowed to regenerate, with BM reconstitution taking place over 21 days. An additional 10-day recovery period was

provided before injecting tumor cells. The mice's weight was closely monitored until it returned to pre-transplant levels. Subsequently, the mice went under echocardiography, hemodynamic and cardiac hypertrophy assessment and their lungs were harvest as described in section 3.2.3.2.

3.2.3.4. Echocardiography

Echocardiography was done using VEVO1100 system equipped with a 30-MHz, 100-frame-per-second micro-visualization linear probe for cardiovascular imaging (MS250, Visual Sonics, Toronto, Canada). The mice were anesthetized using a Tabletop Laboratory Animal Anesthesia System (Vet Equip Inc. Pleasanton, USA) with 5% isoflurane and 100% oxygen at a flow rate of 1 L/min. The animals were positioned supine on the imaging platform and connected to the anesthetic system with a nasal con, receiving 1.5% to 2% isoflurane mixed with 1 L/min of 100% oxygen, allowing for spontaneous breathing. A physiological heart rate (HR) of 400–550 bpm was maintained by adjusting the isoflurane levels, as necessary. The isoflurane concentration was carefully increased or decreased gradually to ensure the animal's HR remained within the optimal range. To monitor heart rate (HR), electrocardiogram (ECG) electrodes were attached to the animals' paws using surgical tape and electrode gel. Body temperature was carefully monitored maintaining at 37°C using a rectal thermometer (Indus Instruments, Houston, TX). Dexpanthenol ophthalmic ointment (Bepanthen®, Bayer Leverkusen, Germany) was applied to the eyes to prevent dryness. After removing the chest hair between the sternum and diaphragm with depilatory cream, a pre-warmed acoustic coupling gel (Aquasonic® 100, Parker Laboratories, Inc.) was applied to the chest to ensure optimal ultrasound imaging.

A standard 2D echocardiographic assessment was first conducted in the parasternal long-axis view to evaluate left ventricular (LV) dimensions and systolic performance. LV ejection fraction (LVEF) was calculated from the parasternal long-axis view. The LV area was traced at both end diastole (ED) and end systole (ES), and ejection fraction (EF) was determined using the following formula: LVEF (%) = (LVEDV – LVESV) / LVEDV × 100.

To assess pulmonary artery acceleration time (PAAT) and the velocity time integral (VTI) of pulmonary artery flow, pulsed-wave Doppler was utilized. PAAT, defined as the time interval from the onset of flow to the point of maximum forward flow velocity was measured from the Doppler flow velocity profile of the RV outflow tract (RVOT) in the parasternal short-axis view. In the parasternal short-axis view, focused on the pulmonary artery at the level of the aortic valve, RVOT diameter (RVOTd) was measured at mid-systole from the short-axis view at the pulmonary valve level, while the RVOT velocity time integral (VTI) was calculated from the pulsed-wave Doppler profile. The Doppler sample was placed at the tip of the pulmonary valve leaflets and aligned using color Doppler to optimize the assessment of laminar flow. Cardiac

output (CO) was estimated by combining RVOT VTI, RVOT area, and heart rate, following the methodology outlined in previous studies (162). Cardiac index (CI) was derived by normalizing the CO to 100 g of body weight (ml/min per 100 g). Pulmonary vascular resistance index (PVRI) was calculated using the formula: PVRI = RVSP/CI, where right ventricular systolic pressure (RVSP) was measured in mm Hg.

To assess RV free wall thickness (RVWT), a right parasternal long-axis view was utilized, incorporating both M-mode and B-mode imaging. RV internal diameter (RVID) was assessed in the apical four-chamber view using B-mode by measuring the maximum distance between the RV free wall and the septum. Tricuspid annular plane systolic excursion (TAPSE) was determined in the apical four-chamber view by positioning the M-mode cursor at the junction of the tricuspid valve plane and the RV free wall.

Echocardiographic data, including M-mode, 2D, and flow images, were collected in triplicate, ensuring that respiration peaks were excluded. The imaging was performed 10 to 25 minutes after anesthesia induction, and all calculations were carried out after the images were acquired.

3.2.3.5. Hemodynamic measurement

Invasive hemodynamic measurements were conducted following established protocols. Mice were anesthetized with isoflurane and placed in a supine position on a homeothermic plate (AD Instruments, Spechbach, Germany), which maintained body temperature at 37°C via a rectal probe connected to a control unit. In certain cases, mice were intubated and attached to a small-animal ventilator (MiniVent type 845, Hugo Sachs Elektronik, March-Hugstetten, Germany) for respiratory support. A high-fidelity 1.4F micromanometer/Mikro-Tip Pressure catheter (Millar Instruments, Houston, TX) was inserted into the RV through the right jugular vein to record RVSP. Subsequently, the catheter was passed through the left carotid artery to assess the aorta and LV, enabling the measurement of systemic arterial pressure (SAP). Data acquisition and analysis were performed using the PowerLab system (MPVS-Ultra Single Segment Foundation System, AD Instruments) and LabChart 7 software. Hemodynamic measurements were performed on anesthetized, tracheotomized mice using a fluid-filled catheter (PE 50 tubing).

3.2.3.6. Cardiac hypertrophy (Fulton index) assessment

After completing the measurements, the animals were exsanguinated by cutting the femoral artery under deep anesthesia by receiving 5% isoflurane. The heart was perfused with PBS and harvested. The RV was dissected out from the LV and septum (LV + S) to determine the Fulton index by calculating the weight ratio of RV to (LV + S).

3.2.3.7. Histology assessment

3.2.3.7.1. Medial wall thickness measurement of lung vasculature

To evaluate the medial wall thickness (MWT), the Weigert-Van Gieson staining method was employed. Mouse lung tissue sections, prepared at a thickness of 4 µm, were incubated at 60°C for 1 hr. Following incubation, the sections underwent deparaffinization by immersion in xylol three times, each for 10 minutes. This was followed by rehydration using a graded ethanol series (99% ethanol for 5 minutes twice, then 80% ethanol for 5 minutes, and finally 70% ethanol for 5 minutes). The slides were then immersed overnight at room temperature in Resorcin-Fuchsin solution. The next day, the slides were rinsed in tap water for 15 minutes and briefly dipped in distilled water. Afterward, they were stained with freshly prepared Weigert's iron hematoxylin for 5 minutes, washed in tap water for another 15 minutes, and subsequently treated with Van Gieson solution for 10 minutes. Following a brief rinse in distilled water, the slides were dehydrated in a graded ethanol series in ascending concentrations (70% ethanol for 5 minutes, 80% ethanol for 5 minutes, and 99% ethanol twice for 5 minutes each). Finally, the slides were mounted using Pretex mounting medium and coverslips. The MWT of the lung vasculature was analyzed using a Leica DM6000B microscope in conjunction with Leica Qwin V3 software. MWT was determined by measuring the distance between the lamina elastica interna and lamina elastica externa, applying the formula:
MWT (%) = (2 × medial wall thickness / external diameter) × 100.

3.2.3.7.2. Muscularization percentage of pulmonary vessels

Vascular remodeling was evaluated by double staining 4 µm-thick paraffin-embedded lung sections with antibodies against α-smooth-muscle-actin (α-SMA) and von Willebrand factor (vWF). Hematoxylin was used as a counterstain, and the sections were analyzed under a light microscope. A computerized morphometric system (Qwin, Leica, Wetzlar, Germany) was employed to assess the extent of muscularization in small peripheral pulmonary arteries. The proportion of fully muscularized pulmonary arteries was calculated as a percentage of the total number of pulmonary arteries, following the method previously described. To assess vascular remodeling, paraffin lung sections (3 µm) were double stained with anti–α-actin and anti-vWF. Sections were counterstained with hematoxylin and examined by light microscopy using a computerized morphometric system (Qwin, Leica, and Wetzlar, Germany) for assessing the degree of muscularization of small peripheral pulmonary arteries. The percentage of fully muscularized pulmonary arteries, relative to the total number of pulmonary arteries, was determined as described.

3.2.3.7.3. Immunofluorescence staining for cardiac hypertrophy assessment

Mouse heart tissues were fixed overnight at 4°C in 4% paraformaldehyde (PFA). The next day, the tissues were transferred into PBS, dehydrated, and embedded in paraffin. From each fixed heart, 4 µm-thick paraffin longitudinal sections were prepared. The sections were deparaffinized by heating at 60°C for 1 hr, followed by three washes in xylene for a total of 30 minutes. Subsequently, the sections were immersed in ethanol solutions of varying concentrations (99%, 96%, and 70%) for rehydration. Antigen retrieval was performed by heating the sections in 1 mM citrate buffer (Invitrogen, USA) for 20 minutes. After allowing the sections to cool at room temperature for 10 minutes, they were blocked with 5% BSA in PBS for 1 hr. For staining, the sections were incubated with wheat germ agglutinin (WGA) conjugated to Alexa-488 and isolectin B4 (IB4) conjugated to Alexa-594 (Table 3.2.14), both diluted at 1:1000. These stains were used to assess cardiomyocyte cross-sectional area (CSA) and capillary density, respectively. The sections were then counterstained with DAPI (diluted 1:1000 in PBS) for 10 minutes and mounted using Dako fluorescent mounting medium (DAKO, Denmark). Fluorescence images were captured with a Keyence BZ-X810 microscope (Keyence, Germany). CSA and capillary density were quantified using ImageJ software (NIH, USA). For each section, at least 10 randomly selected areas were imaged at 40x magnification for analysis.

Table 3.2.14. Lectin used for staining

Antibody	Running buffer	Company
Wheat Germ Agglutinin, Alexa Fluor™ 488 Conjugate	A-11037	Invitrogen
Isolectin GS-IB4 From Griffonia simplicifolia, Alexa Fluor™ 594 Conjugate	I21413	Invitrogen

3.2.3.7.4. Staining for collagen deposition in the heart

To assess collagen deposition in heart tissue of the mice, Masson Trichrome staining with Aniline Blue kit was utilized (18156, Morphisto, Germany), longitudinal paraffin sections were deparaffinized and rehydrated (as mentioned in 3.2.3.7.3). Then the slides were stained with Weigert's Hematoxylin for 10 minutes to highlight nuclei, followed by a wash in distilled water. The slides were treated with 1% Phosphomolybdic Acid for 10 minutes, blotted, and stained with Aniline Blue for 5 minutes, followed by another rinse. The slides were then dehydrated using increasing ethanol concentrations (96% and isopropanol, 2–5 minutes each), cleared with xylol (10 minutes), and mounted with a xylol-based medium. The acquired images were analyzed using ImageJ software.

3.2.4. Cell phenotyping

3.2.4.1. Mouse lung dissociation

After dissecting two lobes of the right lung and transferring them into cold 1x PBS, the lung tissue was minced into small pieces and placed into a 6-well plate containing 1.5 mL of enzyme mix. The tissue was incubated at 37°C for 30 minutes with gentle rotation. The enzymatic reaction was halted by adding DMEM supplemented with 10% FCS and 1% P/S, and the cell suspension was then filtered through a 100 µm cell strainer. Following centrifugation and RBC lysis, the resulting cell pellets were prepared for FACS analysis.

3.2.4.2. Adult mouse heart dissociation

To dissociate the mouse heart, the aortic root and atria were removed, leaving the ventricles, which were immediately transferred to a well of a 6-well plate containing 1x PBS (without Ca^{2+} and Mg^{2+}). The ventricles were then finely minced into small pieces, and tissue dissociation was performed using the Multi Tissue Dissociation Kit 2 (130-110-203, Miltenyi Biotec, Germany), following the specific protocol for adult mouse heart dissociation. The tissue fragments were transferred into a C-tube containing 2.5 mL of enzyme mix and processed with the gentleMACS Dissociator. After dissociation, 7.5 mL of DMEM supplemented with 10% FCS and 1% P/S was added to the dissociated tissue, and the cell suspension was filtered through a 100 µm cell strainer. Debris removal was performed according to the kit manual (130-109-398, Miltenyi Biotec, Germany), followed by RBC lysis. The final cell suspension was then prepared for FACS analysis.

3.2.4.3. Flow cytometry on lung, heart and BM

Single-cell suspensions were obtained from dissociated lung and heart tissues of mice, following the procedure outlined in section 3.2.4.1 and 3.2.4.2. To prevent nonspecific binding, cells were incubated with Fc receptor (FcR) blocking reagent (Miltenyi Biotec) in 0.5% PBS-BSA for 20 min. After blocking and labeling the cells with fluorochrome-conjugated antibodies, a FACS Symphony A5SE flow cytometer (BD Biosciences) was used to analyze the cells for further characterization. Live and single-cell populations were identified by assessing FSC and SSC profiles. The optimal antibody and reagent concentrations were determined through titration. Single-color compensation controls were created using BD Comp-Beads to construct multicolor compensation matrices. Fluorescence-minus-one (FMO) controls were employed for accurate gating. Instrument calibration was verified daily with Cytometer Setup and Tracking beads (BD Biosciences) to ensure proper functionality. Data were processed using FlowJo V10 software (TreeStar). The antibodies used in the experiment are listed in Table 3.2.15.

Table 3.2.15. Antibodies used for flow cytometry of lung and heart

Marker	Fluorochrome	Company
CD16/32	none	Biolegend
CD3	PE-CF594	BD Biosciences
CD4	V500	BD Biosciences
CD8	BV650	eBioscience
CD11b	BV605	eBioscience
CD11c	AlexaFluor700	BD Biosciences
CD19	APC-H7	BD Biosciences
CD45	VioBlue	Biolegend
CD206	FITC	Biolegend
F4/80	PE-Cy7	Biolegend
HLA-DR (MHC II)	APC	Miltenyi Biotec
Ly-6C	PerCP-Cy5.5	BD Biosciences
Ly-6G	APC-Cy7	Biolegend
CD49b	PE	Biolegend
CD80	PE	BD Biosciences
CD31	PE-Cy7	Miltenyi Biotec

3.2.4.4. HSCs phenotyping and sorting

Femurs and tibiae were removed from each mouse separately for single mouse analysis and cleaned to remove excess muscles and fibrous tissues. BM cells were extracted by flushing out from the bones with 3 ml cold 1x PBS using a 5 ml syringe (B. Braun SE, Germany) applied with a 23G needle (BD Biosciences, USA). To enrich BM-mononuclear cells, the 3 ml cell suspension was carefully loaded on top of 3 ml Histopaque® 1083 (Sigma, USA) and seperated by density gradient centrifugation (400 x g, 30 min, RT), without setting the breaks. The interphase was collected and washed twice with 1 x PBS (290 x g, 7 min, 4°C) and resuspended in 100 µl FACS buffer and were counted. The cells were incubated with 1 µl of the antibodies mentioned in table 3.2.16 and utilized for HSC phenotyping or sorting (163).

Table 3.2.16. Antibodies used for phenotyping of HSCs by flow cytometry

Marker	Company
Biotin anti-mouse CD3ε	Biolegend
Biotin anti-mouse CD19	Biolegend
Biotin anti-mouse B220	Biolegend
Biotin anti-mouse CD11b/Mac1	Biolegend
Biotin anti-mouse Gr1	Biolegend
Biotin anti-mouse Ter119	Biolegend
Biotin anti-mouse CD41	Biolegend
BV510 anti-mouse Sca-1	Biolegend

FITC anti-mouse CD48	Biolegend
BV421 anti-mouse CD117(cKit)	Biolegend
PE anti-mouse CD150	Biolegend
PE-Cy5 anti-mouse CD135	Biolegend
BV711 Streptavidin	Biolegend
eF780 Fixable viability dye	eBioscience
APC-H7 mTer119	Biolegend
eF660 anti-mouse CD34	eBioscience

3.2.5. HILIC-MS Method for Metabolome Analysis

Metabolome analysis was performed using a hydrophilic interaction liquid chromatography (HILIC) method coupled with high-resolution mass spectrometry. For sample preparation, 100 µL of Trifluoroethanol (TFE):H_2O (1:1) was added to the samples, followed by incubation for 10 minutes. Subsequently, 200 µL of MeOH (1:1) was added, and the mixture was incubated for another 10 minutes. An additional 200 µL of H_2O and 10 µL of an internal standard mix containing isotopically labeled standards (Homotaurine, Succinate-1,4-13C3, and Citrate-1,5-13C3 at 0.04 mM) were added and incubated for 10 minutes. The samples were sonicated on ice for 30 seconds, centrifuged at 14,000 rpm for 10 minutes at 4°C, and the supernatant was transferred into a new tube. The samples were partially dried under nitrogen flow, frozen at -80°C, and freeze-dried overnight. Dried samples were reconstituted in 7.5 µL of Milli-Q water, sonicated on ice for 30 seconds, and mixed with 42.5 µL of acetonitrile, followed by a final centrifugation (14,000 rpm, 10 minutes, 4°C). The supernatants were transferred to mass spectrometry vials, and 5 µL of each sample was injected for analysis. Blank samples, quality controls, and a 10-point standard curve were also prepared and analyzed.

The separation was carried out using a Waters Acquity UPLC BEH Amide column (2.1×100 mm, 1.7 µm) on an Agilent 1290 Infinity II BIO HPLC system. The mobile phase consisted of Solvent A (10 mM ammonium acetate and 5 µM medronic acid in water, pH 9.2) and Solvent B (10 mM ammonium acetate in acetonitrile, pH 9.2). A gradient elution was used, starting at 85% B, decreasing to 10% B over 15 minutes, and returning to 85% B for re-equilibration. The flow rate was set to 0.4 mL/min. Detection was performed using an Agilent 6495C QQQ mass spectrometer in positive polarity mode with AJS ESI and dynamic multiple reaction monitoring (MRM). Data analysis, including metabolite annotation and peak integration, was performed using Skyline-daily software.

3.2.6. Statistical analysis

Statistical analysis was conducted using Prism 10 software (GraphPad Software Inc., San Diego, USA). A two-tailed Student's *t*-test was employed for comparisons between two groups. For comparisons involving more than two groups, a one-way ANOVA followed by Tukey's

multiple comparison test was used to analyze unpaired, non-parametric variables. Data are presented as mean ± Standard Error of the Mean (SEM), with statistical significance defined as $p \leq 0.05$.

4. Results

4.1. *Irg1*$^{-/-}$ mice display RV and LV dilation and dysfunction

To investigate the baseline cardiac phenotype in the absence of *Irg1*, male *Irg1*$^{-/-}$ and control WT mice were analyzed for cardiac function using echocardiography, a non-invasive imaging technique. Subsequently, lungs and hearts were removed for anatomical and histological examinations. Echocardiography revealed a significant increase in left ventricular internal diameter (LVID) and a concomitant decrease in left ventricular ejection fraction (LVEF) in *Irg1*$^{-/-}$ mice (Figure 4.1.A, B). Examination of the right heart showed a remarkable increase in right ventricular internal diameter (RVID) and RV wall thickness (RVWT) (Figure 4.1.A, C). In addition, tricuspid valve plane systolic excursion (TAPSE), a parameter that assesses the longitudinal contraction of the annular plane of the tricuspid valve toward the apex of the heart during systole, was decreased in *Irg1*$^{-/-}$ mice (Figure 4.1.A, D). While heart rate (HR) remained unchanged between WT and *Irg1*$^{-/-}$ mice (Figure 4.1.E), *Irg1*$^{-/-}$ mice exhibited a significant reduction in both stroke volume (SV) and cardiac output (CO) compared to WT mice (Figure 4.1.F). Physiological assessment revealed a significant increase in left ventricular (LV) hypertrophy with a significantly increased LV mass to body weight (LV+septum/BW) and LV mass to tibial length (LV+septum/tibial length) ratio (Figure 4.1.G). However, *Irg1*$^{-/-}$ mice maintained a comparable body weight to WT mice (Figure 4.1H).

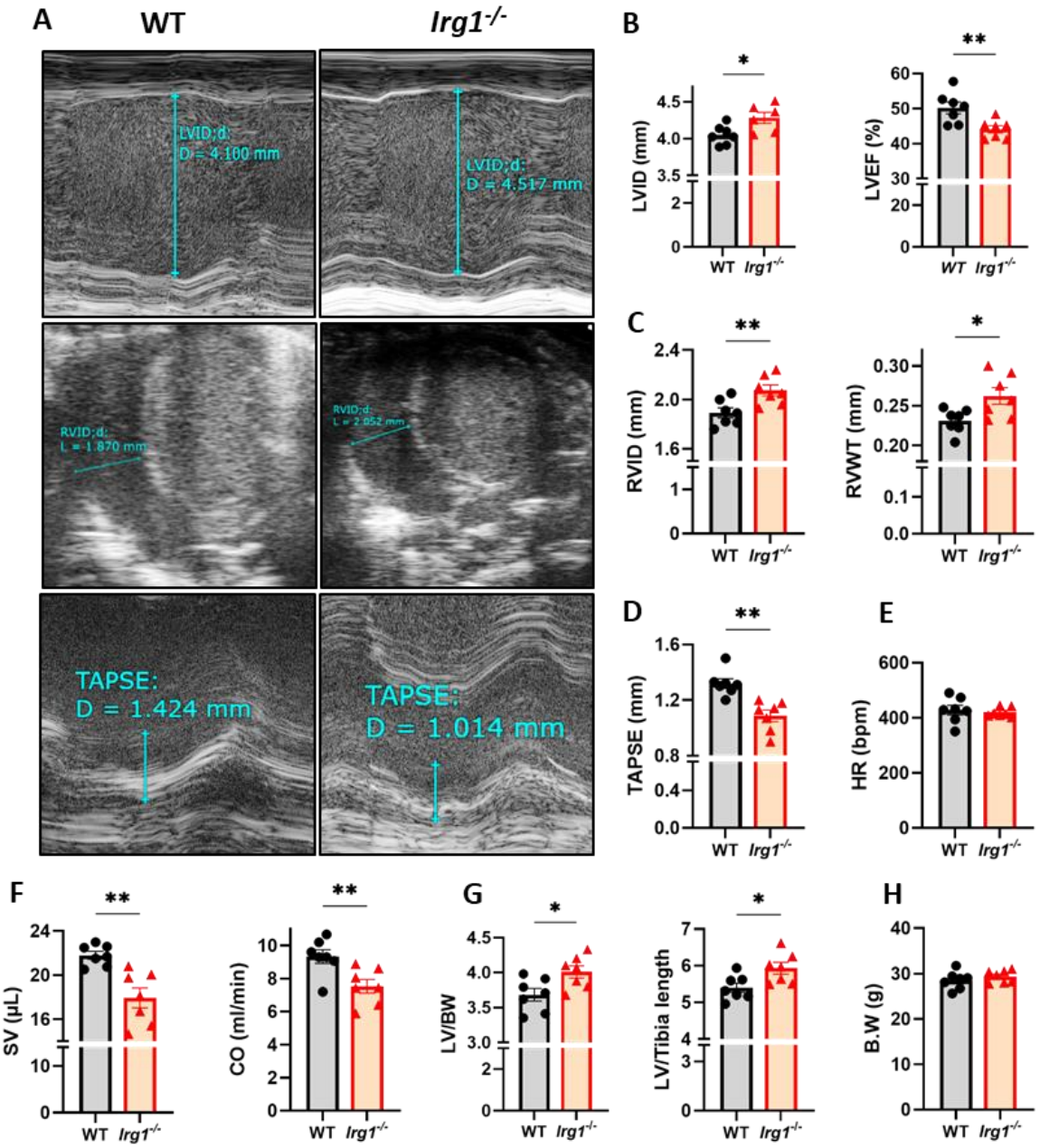

Figure 4.1: RV and LV dilation and failure in *Irg1-/-* mice. A) Representative echocardiographic images of WT and *Irg1*$^{-/-}$ hearts depicting LVID in the long-axis view (first row), RVID (middle row) and TAPSE (last row) in the four-chamber view. B-E) Quantitative echocardiographic measurements. B) LVID and LVEF. C) RVID and RVWT. D) TAPSE. E) SV and CO. F) LV mass, measured as the ratio of LV weight to total body weight ((LV+S)/BW) or tibia length ((LV+S)/Tibia length). G) Body weight (B.W.). LVID: Left ventricular internal diameter; LVEF: LV ejection fraction; RVID: Right ventricular internal diameter; RVWT: RV wall thickness; TAPSE: Tricuspid valve plane systolic excursion; HR: Heart rate; SV: stroke volume; CO: cardiac output. LV mass to body weight (LV+septum/BW) and LV mass to tibial length (LV+septum/tibial length) ratio. *n*=7 mice per group. Error bars indicate mean with SEM. Data were analyzed with unpaired Student's t-test *p<0.05, **p<0.01.

4.2. *Irg1*-deficient mice develop cardiomyocyte hypertrophy and impaired angiogenesis in the baseline.

To explore the cellular basis of cardiac hypertrophy, we performed immunofluorescence staining of cardiac cross-sections from WT and *Irg1*$^{-/-}$ mice using wheat germ agglutinin (WGA-FITC) and isolectin b4 (IB4-596) for cell membrane and endothelial cell membrane staining, respectively. This approach was designed to measure the cross-sectional area (CSA) of cardiomyocytes and assess capillary density in the LV and RV. The results showed that *Irg1*$^{-/-}$ mice exhibited a significant increase in CSA at baseline (Figure 4.2.A-C) in both ventricles, accompanied by a marked decrease in capillary density (Figure 4.2.A, B and D).

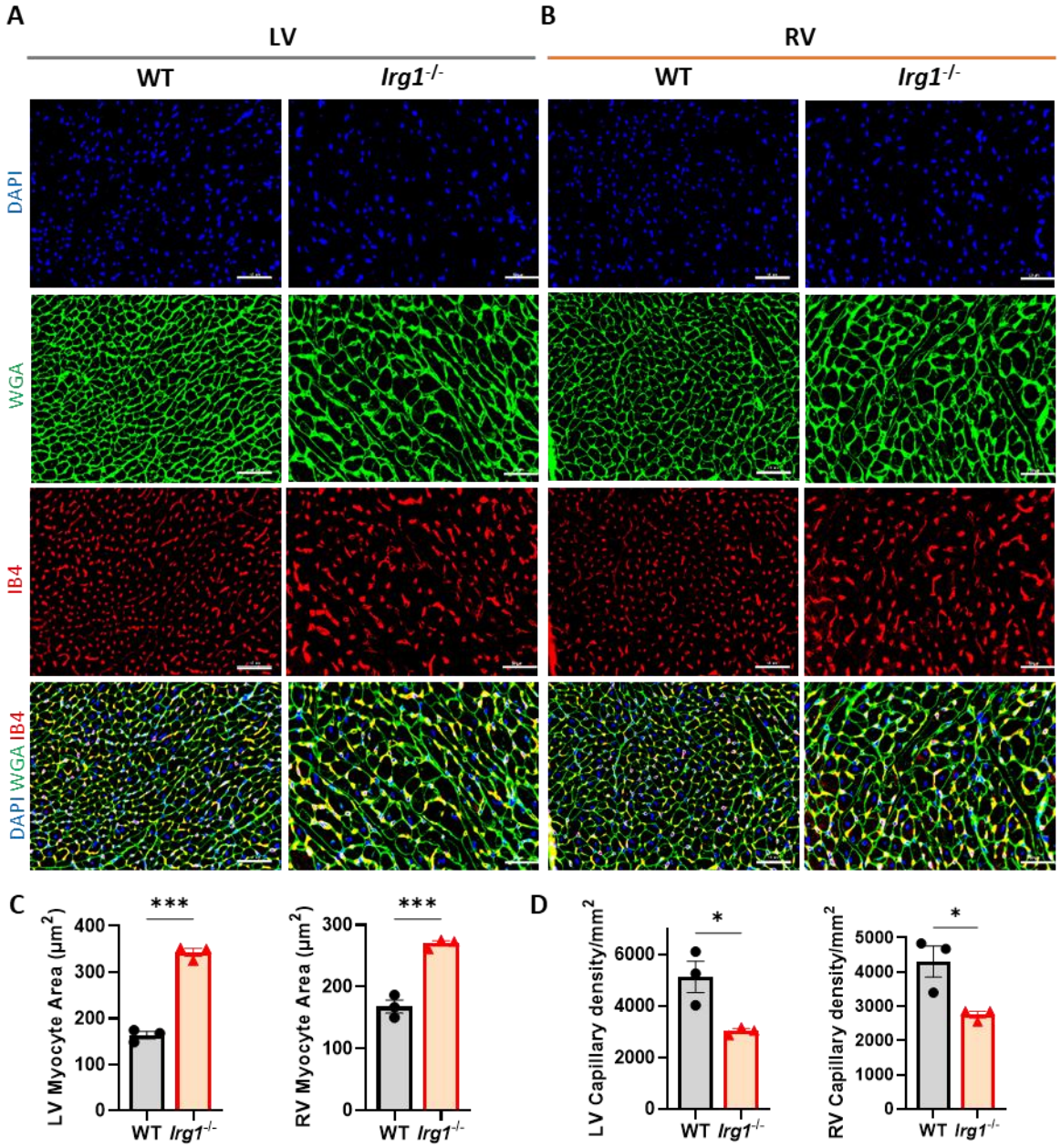

Figure 4.2: Cardiomyocyte hypertrophy and reduced capillary density in *Irg1*$^{-/-}$ hearts. A, B) Representative immunofluorescence staining of WGA (green), IB4 (red) and DAPI (blue).

C) Quantification of LV and RV myocyte area, C) Quantification of LV and RV capillary density. LV (*n* = 3), RV (*n* = 3). Scale bars: 50µm. LV: left ventricle; RV: right ventricle. Error bars indicate the mean value with SEM. Data were analyzed with an unpaired Student's *t*-test *p<0.05, ***p<0.001.

4.3. Irg1-deficient mice exhibit increased collagen deposition in their hearts.

Since excessive collagen deposition may be associated with cardiac dysfunction and hypertrophy because it contributes to stiffening of the myocardial ECM, we performed Masson trichrome staining on cross-sections of hearts to examine total collagen deposition in the heart. The collagen content was twice as high in *Irg1*$^{-/-}$ hearts, with a higher accumulation in the perivascular area of the intra-cardiac vessels (Figure 4.3.A-B). We also analyzed the collagen III (Col III) content in mice. Western blot analysis of the LV of WT and *Irg1*$^{-/-}$ mice showed an upregulation of Col III in *Irg1*$^{-/-}$ hearts compared to WT (Figure 4.3.C-D).

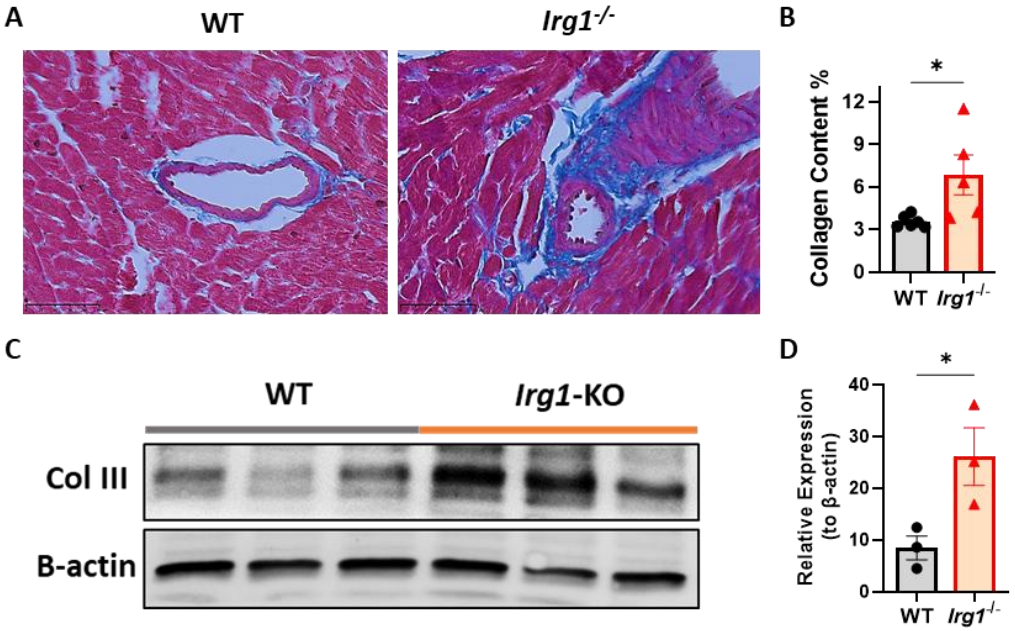

Figure 4.3: Increased collagen content in *Irg1*$^{-/-}$ hearts. A) Representative images of Masson's trichrome staining of WT and *Irg1*$^{-/-}$ heart sections. Scale bars: 50µm. B) Quantitative analysis of the percentage of collagen deposition in heart slices from WT and *Irg1*$^{-/-}$ mice (*n* = 5 per group). C) Representative images of the protein content of collagen III (Col III) and β-actin (loading control) determined by Western blot analysis. D) Corresponding densitometric quantification of Western blots as relative expression to the loading controls (*n* = 3 per group). The error bars indicate the mean value with SEM. Data were analyzed with unpaired Student's t-test *p<0.05.

4.4. *Irg1*$^{-/-}$ hearts display increased immune cell infiltration and altered myeloid cell composition in the baseline.

Considering that *Irg1* acts as an immunometabolic regulator, we performed a comprehensive whole heart immune profiling of both WT and *Irg1*$^{-/-}$ mice by flow cytometry (FACS) for our

assessment (Figure 4.4.A). The data showed a marked increase in the infiltration of total immune cells into the hearts of *Irg1*$^{-/-}$ mice (Figure 4.4.B), along with changes in the composition of macrophages and DCs. The total population of macrophages (CD45^{+}Ly6C^{+}Ly6G^{-}F4/80^{+}) increased significantly in the *Irg1*$^{-/-}$ mice (Figure 4.4.C), particularly in the subset of macrophages expressing low levels of MHC II (MHC II^{low}) (Figure 4.4.D). In addition, the composition of MHC II^{low} DC was also increased in the *Irg1*$^{-/-}$ hearts. In addition, plasmacytoid DCs (pDCs, CD45^{+}CD11c^{+}MHCII^{+}SiglecH^{+}), which are key components of the immune system and are characterized by their significant production of type I interferons, showed increased populations in *Irg1*$^{-/-}$ hearts (Figure 4.4.E). However, the numbers of monocytes (CD45^{+}CD11b^{+}Ly6C^{+}), B cells (CD45^{+}CD11b^{-}CD19^{+}) and neutrophils (CD45^{+}CD11b^{+}Ly6G^{+}) remained relatively unchanged between *Irg1*$^{-/-}$ and WT mice (Figure 4.4.F). These results suggest that *Irg1*$^{-/-}$ mice have a unique immune cell profile in the heart characterized by an increase in specific macrophage and DC populations. This imbalance in the myeloid cell lineage could potentially impact the polarization and inflammatory response of other immune cells, leading to changes in the transcriptome and morphology of the heart.

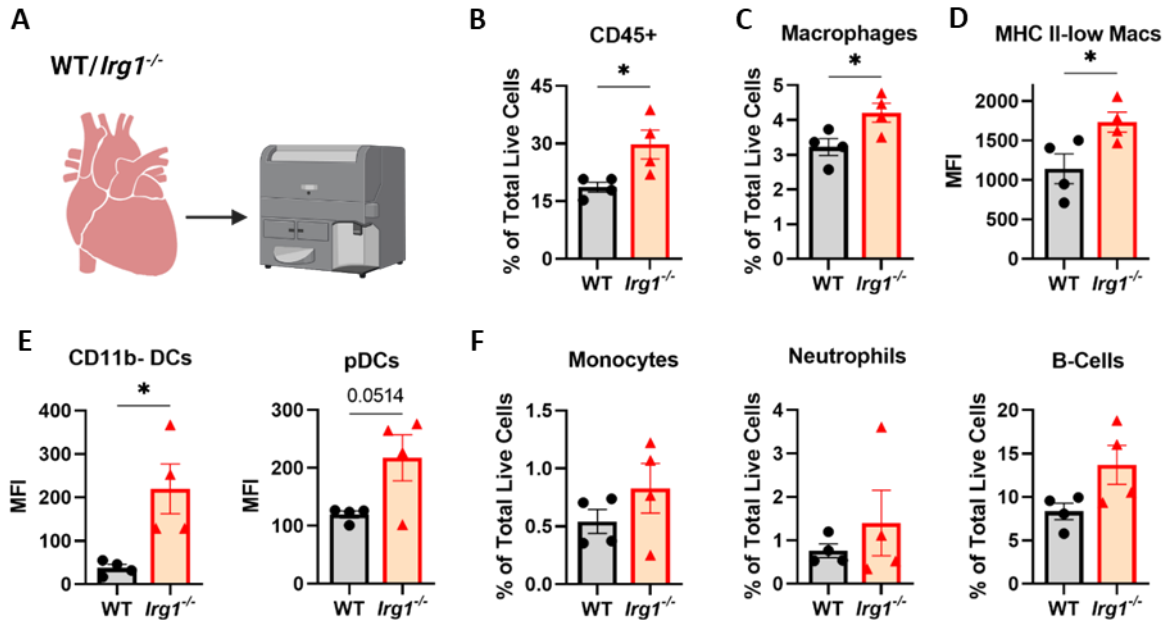

Figure 4.4: Impaired macrophage and DCs deposition in the *Irg1*-deficient heart. A) Schematic representation of FACS analysis for immune profiling of LV and RV in WT and *Irg1*$^{-/-}$ mice. B) Percentage of CD45+ cells in the total living cell population. C) Percentage of total MΦ (CD45^{+}Ly6C^{+}Ly6G^{-}F4/80^{+}) in the total living cells detected. D) Mean fluorescence intensity (MFI) of MHC II^{low} macrophages. E) MFI of CD11b^{low} DCs (CD45^{+}CD11c^{+}CD11b^{low}) and pDCs (CD45^{+}CD11c^{+}MHCII^{+}SiglecH^{+}). F) Proportion of monocytes (CD45^{+}CD11b^{+}Ly6C^{+}), neutrophils (CD45^{+}CD11b^{+}Ly6G^{+}) and B cells (CD45^{+}CD11b^{-}CD19^{+}) in the total number of living cells detected. *n* = 4 per group. The error bars indicate the mean value with SEM. Data were analyzed with unpaired Student's *t*-test. *p<0.05.

4.5. *Irg1*$^{-/-}$ mice display altered transcriptomic signature in both RV and LV.

To elucidate the underlying mechanisms of cardiac hypertrophy in *Irg1*$^{-/-}$ mice, we extracted RNA from the RV and LV of WT and *Irg1*$^{-/-}$ and performed transcriptomic profiling by bulk RNA sequencing. Data analysis revealed that a total of 37 genes were differentially expressed in the LV and 15 genes in the RV of *Irg1*$^{-/-}$ mice compared to WT controls (FDR < 0.05; Log2FC > ±0.585; mean number > 5in) (Figure 4.5.A). Of these, 16 and 10 differentially expressed genes (DEGs) were upregulated and 21 and 5 DEGs were downregulated in *Irg1*$^{-/-}$ LV and RV, respectively (Figure 4.5.B-C). To identify the most enriched pathways, Gene Set Enrichment Analysis (GSEA) using Hallmark Pathway Analysis revealed changes (either upregulation or downregulation) in the gene expression profile of 12 and 21 pathways in *Irg1*$^{-/-}$ LV and RV, respectively (normalized enriched score (NES) <> ±1.3 and FDR < 0.2). The Venn diagram visually depicts the distribution of differentially regulated signaling pathways in the RV and LV of *Irg1*$^{-/-}$ mice. There are 3 characteristic pathways that are altered exclusively in the LV, 12 pathways that are altered only in the RV, and 9 pathways that are altered in both ventricles together, indicating a common regulatory pattern in the cardiac hypertrophy observed in these *Irg1*-deficient mice (Figure 4.5.D).

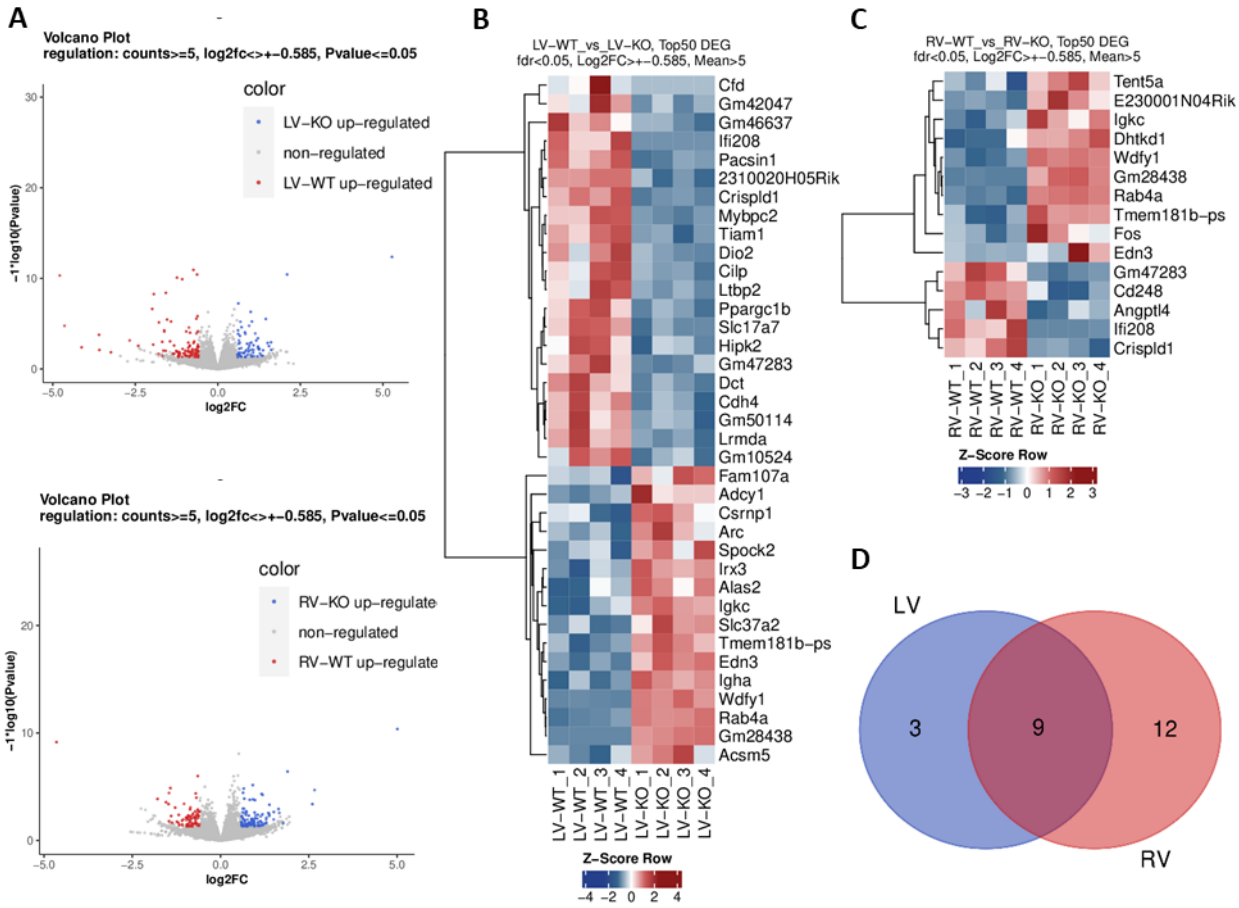

Figure 4.5: Transcriptomic profiling of LV and RV of *Irg1*$^{-/-}$ mice compared to WT mice. A) Volcano plot of all genes detected in the bulk RNA-seq of LV (top) and RV (bottom) (*n* = 4

per group). The X-axis is the log2-base fold change (log2FC) and the Y-axis is the −log10-base P value. The upregulated and downregulated genes in *Irg1*$^{-/-}$ samples are shown in red and blue, respectively. B) Heatmap showing the top 50 DEGs between WT and *Irg1*$^{-/-}$ LV and C) RV, based on log2FC (<> ± 0.58) and statistical significance (FDR < 0.05). Each row represents one DEG, and each column represents one sample. Red: represents the upregulated DEGs and blue: represents the downregulated DEGs. D) The Venn diagram visually represents the distribution of differentially regulated hallmark pathways in the RV and LV of *Irg1*$^{-/-}$ mice (normalized enriched score (NES) <> ±1.3 and FDR < 0.2). *n* = 4 per group. LV: left ventricle; RV: right ventricle.

4.6. Enrichment of inflammatory- and hypoxia-associated signaling pathways contributes to RV and LV remodeling in *Irg1*$^{-/-}$ mice.

Analysis of Hallmark signaling pathways revealed that Hallmark hypoxia and Hallmark_ TNFα_signalling_via_NFkB appeared as prominently enriched gene sets in both the LV and RV of *Irg1*$^{-/-}$ mice (Figure 4.5.A and B). Transcriptomic analysis of the hearts of *Irg1*$^{-/-}$ mice revealed significant dysregulation of gene expression associated with inflammation and hypoxia, suggesting that these processes play a key role in the observed cardiac hypertrophy.

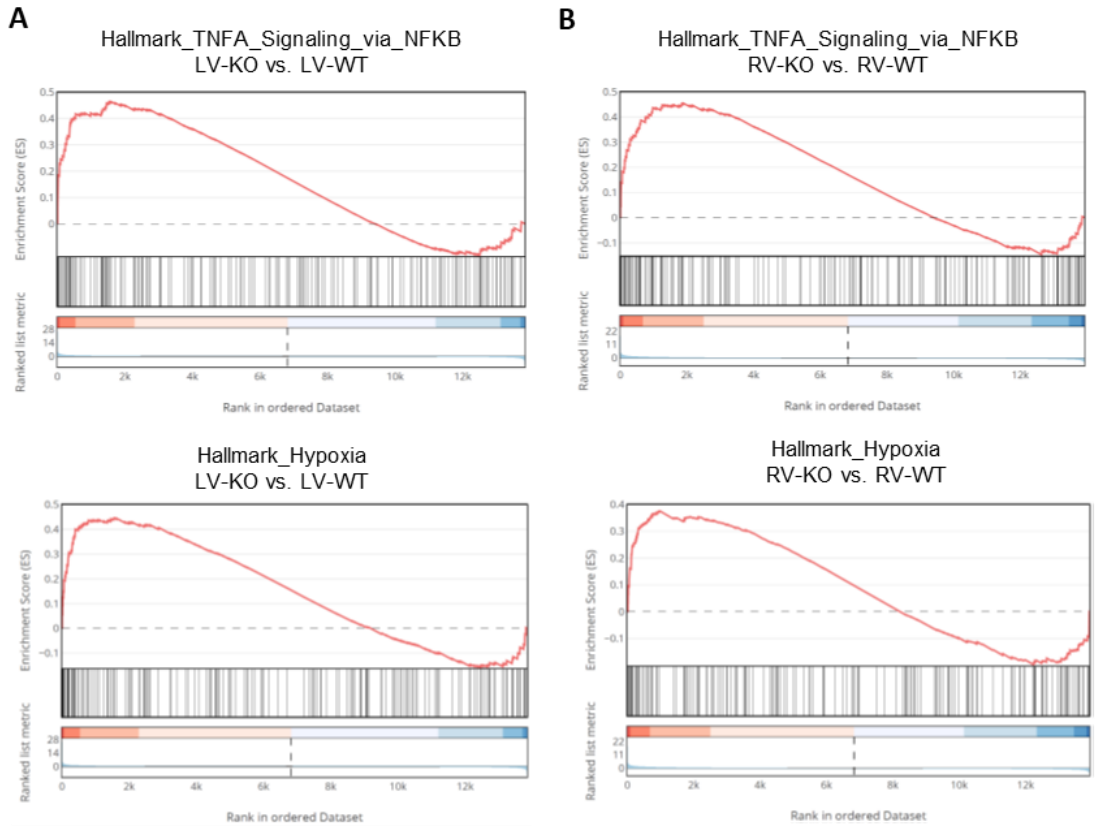

Figure 4.6: Enrichment of TNF-α signaling via NF-κB and hypoxia features in *Irg1*$^{-/-}$ RV and LV. A) Gene set enrichment analysis (GSEA) enrichment plots of TNF-α signaling via NF-κB (top) and hypoxia hallmarks (bottom) significantly enriched in *Irg1*$^{-/-}$ LV and B) RV. LV: left ventricle; RV: right ventricle.

4.7. Jmjd3 and End3 are associated with hypertrophic phenotype of *Irg1*$^{-/-}$ heart.

RNA-seq data from RV and LV showed a significant increase in histone demethylase Jumonji domain-containing protein-3 (JMJD3, also known as KDM6B) in *Irg1*$^{-/-}$ hearts. Jmjd3, which demethylates histone 3 lysine 27 trimethylation (H3K27me3) to activate gene expression of inflammatory pathways, including TNF-α and NF-κB, showed increased expression at both mRNA and protein levels in (Figure 4.7.A-C). This upregulation was accompanied by a marked reduction in H3K27me3 expression (Figure 4.7.B-C). In addition, endothelin 3 (End3), a member of the endothelin family that is critical for HF-related cardiac and vascular pathology, was among the significantly upregulated DEGs and showed increased protein levels in the *Irg1*$^{-/-}$ hearts (Figure 4.7.B and C). These results suggest that dysregulation of JMJD3 and End3 may contribute to the cardiac hypertrophy phenotype in *Irg1*$^{-/-}$ mice.

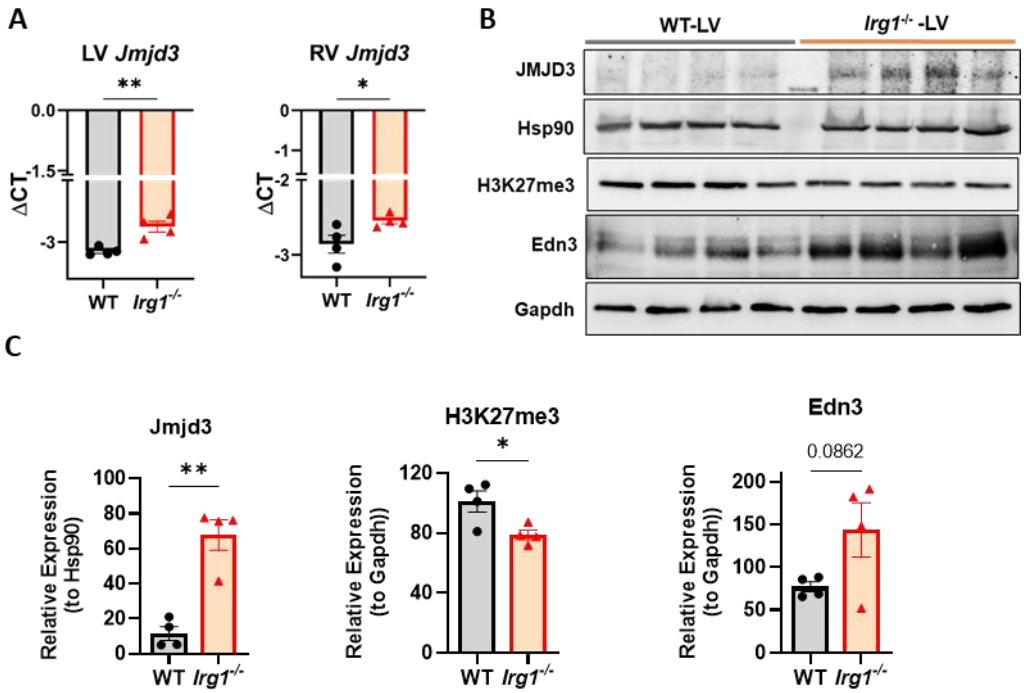

Figure 4.7: Upregulation of Jmjd3 and Edn3 in the *Irg1*$^{-/-}$ heart. A) Jmjd3 mRNA expression (ΔCT) in WT and *Irg1*$^{-/-}$ LV (left) and RV (right). B) Representative images of protein levels of Jmjd3, H3K27me3, Edn and loading controls: Hsp90 and Gapdh, determined by WB analysis. C) Corresponding densitometric quantification of WBs (*n* = 4 per group) as relative expression to the loading controls. Error bars indicate the mean value with SEM. Data were analyzed with unpaired Student's *t*-test. *p<0.05, **p<0.01.

4.8. *Irg1*-deficient mice develop mild pulmonary vascular remodeling at baseline.

After observing RV dilatation in *Irg1*$^{-/-}$ mice, we performed a histological examination of pulmonary vascular remodeling. Using elastica van Gieson staining, which highlights the inner elastic lamina and collagenous intimal thickening, the medial wall thickness of pulmonary vessels was examined. To determine the degree of muscularization in the small peripheral

pulmonary vessels (20-70 µm), lung sections from mice were double stained with anti-α-smooth muscle actin (αSMA) and anti-von Willebrand factor (vWF). Quantification of the data revealed that *Irg1*$^{-/-}$ mice had significantly greater medial wall thickness in microscopic small- (20-70 µm) and medium-sized (70-150 µm) vessels (Figure 4.8.A, B). In addition, the number of muscular microvessels increased (Figure 4.8.A, C).

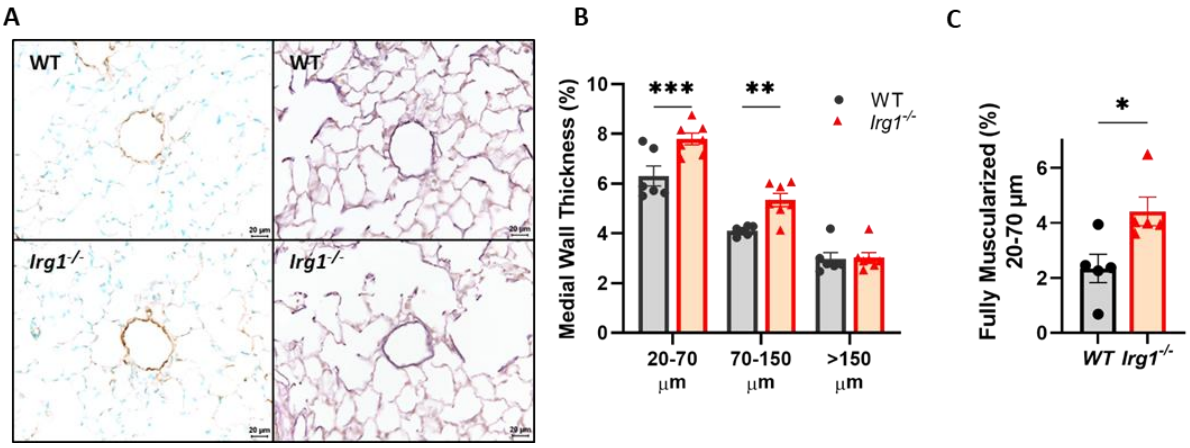

Figure 4.8: Remodeled pulmonary vessels in *Irg1*$^{-/-}$ mice. A) Representative images of immunostaining with vWF and α-SMA (left) and staining of medial wall thickness (elastin, right) B) Percentage of thickening of the medial wall of pulmonary vessels (*n* = 6 lungs per group). C) Percentage of fully muscled vessels (20–70 µm in diameter) (*n* = 5 lungs per group). Scale bars: 20µm. The error bars indicate the mean with SEM. Data were analyzed using two-way ANOVA and unpaired Student's t-test *p<0.05, **p<0.01, ***p<0.001.

4.9. *Irg1*$^{-/-}$ mice develop an exacerbated PH phenotype under hypoxic condition.

Given the observed cardiopulmonary phenotype associated with Irg1/Itaconate deficiency, we sought to further elucidate the role of the IRG1/Itaconate axis in CVD using the PH hypoxia mouse model. This established model effectively induces pulmonary vascular remodeling and subsequent RV hypertrophy in mice (164). In our study, WT and *Irg1*$^{-/-}$ mice were exposed to hypoxia (10% O2) for five weeks and underwent extensive hemodynamic and echocardiographic studies. After the interventions, the harvested organs, particularly the lungs and BM cells, were analyzed for immune cell profiles by FACS (Figure 4.9.A). Remarkably, *Irg1*$^{-/-}$ mice exhibited a marked increase in RV systolic pressure (RVSP) compared to WT mice, while LVSP remained unaffected (Figure 4.9.B). RV hypertrophy was more pronounced in *Irg1*-deficient mice, as evidenced by an increased Fulton index (RV/LV+septum) (Figure 4.9.C), increased RV wall thickness and RVID (Figure 4.9.D). *Irg1*$^{-/-}$ mice also showed worsening of CI and SVI (Figure 4.9.E). In addition, two other critical PH-related parameters, TAPSE and pulmonary vascular resistance index (PVRI), were severely deteriorated in *Irg1*$^{-/-}$ mice (Figure 4.9.F). LVEF was similarly impaired in hypoxic *Irg1*$^{-/-}$ mice as at baseline, and this impairment might be independent of PH-associated phenotypes (Figure 4.9.G).

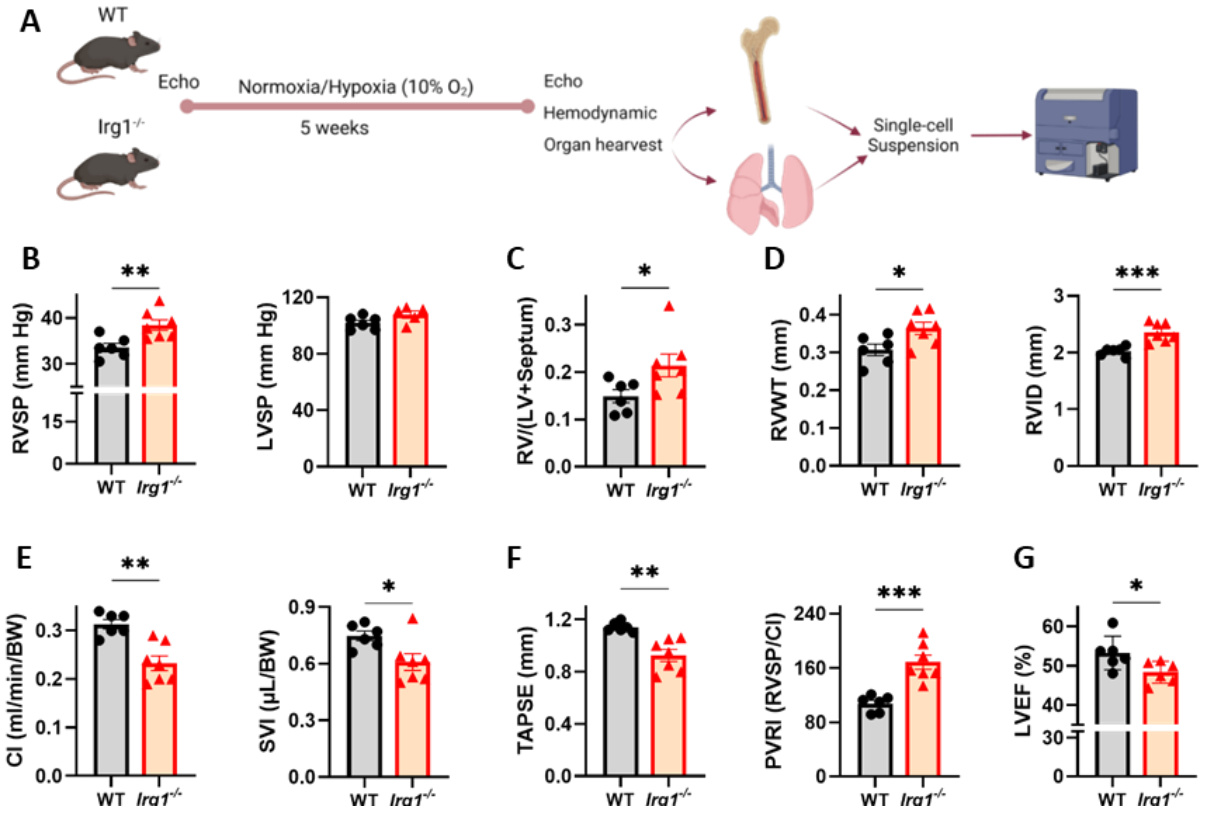

Figure 4.9: Aggravated PH phenotype in *Irg1*-deficient mice. A) Schematic representation of the hypoxia mouse model: WT and *Irg1*$^{-/-}$ mice were exposed to hypoxia for five weeks, followed by hemodynamic and echocardiographic examinations. Single cell suspensions from BM and heart lung were used for FACS immunoprofiling. B) Hemodynamic measurement of RVSP and LVSP. C) Fulton index (RV/(LV+septum)). D-G) Echocardiographic measurement of cardiac parameters in hypoxia-exposed WT and *Irg1*$^{-/-}$ mice. D) RVWT and RVID. E) CI and SVI. F) TAPSE and PVRI. G) LVEF. RVSP: right ventricle systolic pressure; LVSP: left ventricle systolic pressure; RVWT: RV wall thickness; RVID: RV internal diameter; CI: cardiac output ratio to body weight; SV: stroke volume ratio to body weight; TAPSE: Tricuspid valve plane systolic excursion; LVEF: LV ejection fraction. *n* = 5-7 mice per group. The error bars indicate the mean value with SEM. Data were analyzed using two-way ANOVA and unpaired Student's t-test *p<0.05, **p<0.01, ***p<0.001.

4.10. Hypoxia induction aggravates pulmonary vascular remodeling in *Irg1*$^{-/-}$ mice.

Vascular remodeling as the most important pathological feature of PH was studied in hypoxic mice. Both the thickness of the medial vessel wall and the number of muscular microvessels were significantly greater in hypoxic *Irg1*$^{-/-}$ mice compared to hypoxic WT mice (Figure 4.10.A-C). These results suggest that *Irg1* deficiency worsens the cardiopulmonary phenotype under hypoxia conditions and leads to exacerbation of PH.

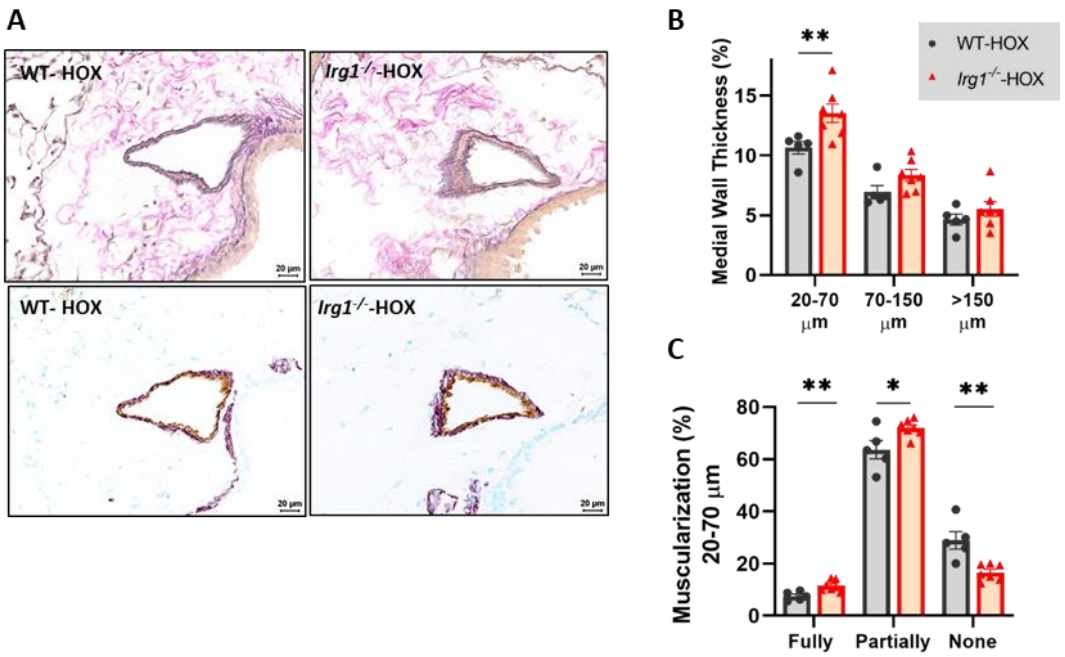

Figure 4.10: Evaluation of pulmonary vascular remodeling in hypoxia-exposed WT and *Irg1*$^{-/-}$ mice. A) Representative images of immunostaining with medial wall thickness (elastin, top) and vWF and α-SMA staining (bottom). B) Percentage of thickening of the medial wall of the pulmonary vessels. C) Percentage of fully, partially and non-muscularized vessels (20–70 µm diameter). WT *n* = 5 for WT and *n* = 7 for *Irg1*$^{-/-}$ lungs per group. Scale bars: 20µm. Error bars indicate the mean value with SEM. Data were analyzed with two-way ANOVA, *p<0.05, **p<0.01.

4.11. Irg1 deficiency elevates myeloid-derived immune cells composition, in lung of hypoxia-exposed mice.

To understand how immune cell composition changes in hypoxia-exposed *Irg1*$^{-/-}$ mice compared to WT mice, we performed lung immune profiling using FACS. The data showed that the total populations of macrophages ($CD45^+CD11b^+Ly6C^+F4/80^+$), DCs ($CD45^+CD11c^+$) were increased in *Irg1*$^{-/-}$ lungs (Figure 4.11.A), while the total number of AMs ($CD45^+CD11b^-CD11c^+$ $Ly6C^+F4/80^+$) and monocytes ($CD45^+CD11b^+Ly6C^+$) remained unchanged (Figure 4.11.B). In addition, the proportion of natural killer cells (NKs, $CD45^+CD3^-CD49b^+$) was increased in *Irg1*$^{-/-}$ lungs (Figure 4.11.C). The composition of Neutrophils ($CD45^+CD11b^+Ly6G^+$), B cells ($CD45^+CD11b^-CD19^+$) and T cells ($CD45^+CD11b^-CD3^+$) was also unchanged (Figure 4.11.D). These results suggest that *Irg1* deficiency leads to a specific increase in certain immune cell populations under hypoxic conditions, which may contribute to the exacerbated PH observed in these mice. The increased levels of MΦs, DCs, suggest a possible role of myeloid-derived cells in mediating the enhanced inflammatory response and vascular remodeling associated with *Irg1* deficiency in hypoxia-induced PH.

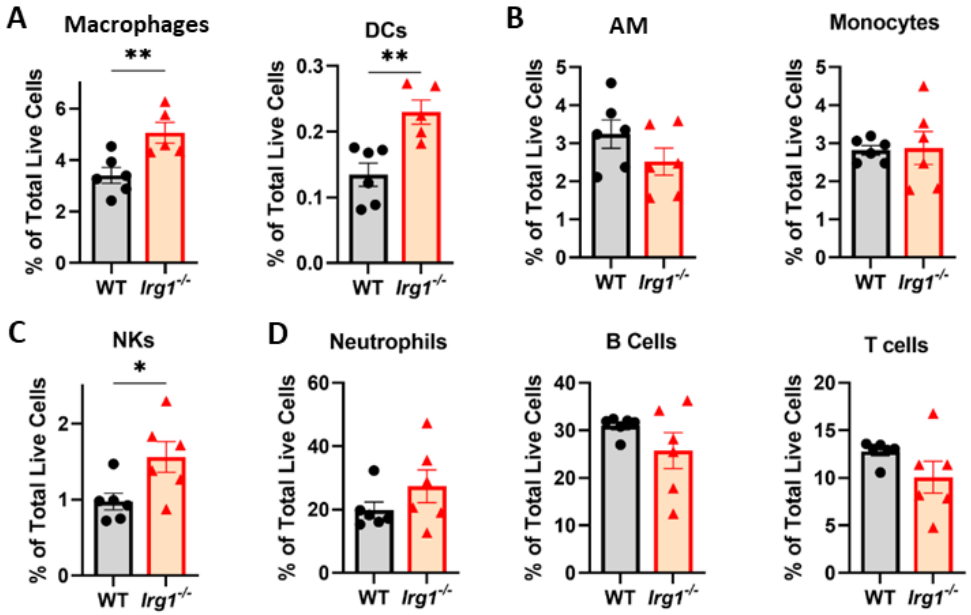

Figure 4.11: Increased composition of myeloid cells in hypoxic *Irg1*$^{-/-}$ mice. FACS immunoprofiling of hypoxia-exposed WT and *Irg1*$^{-/-}$ lungs: A) Percentage of interstitial macrophages (CD45^{+}CD11b^{+}Ly6C^{+}F4/80^{+}), DCs (CD45^{+}CD11c^{+}), B) AMs (CD45^{+}CD11b^{-} CD11c^{+} Ly6C^{+}F4/80^{+}) and monocytes (CD45^{+}CD11b^{+}Ly6C^{+}) of the total living cells detected. C) Quantification of the composition of NKs (CD45^{+}CD3^{-}CD49b^{+}). D) Neutrophils (CD45^{+}CD11b^{+}Ly6G^{+}), B cells (CD45^{+}CD11b^{-}CD19^{+}) and T cells (CD45^{+}CD11b^{-}CD3^{+}) compositions as a percentage of the total living cells detected. DCs: dendritic cells; AMs: alveolar macrophages; NKs: natural killer cells. *n* = 5-6 per groups. The error bars indicate the mean value with SEM. Data were analyzed using unpaired Student's *t*-test. *p<0.05. **p<0.01.

4.12. Irg1-deficient mice display impaired immune cell composition in BM.

The BM serves as a central hub for immune regulation as it influences the production and differentiation of various subsets of immune cells, which in turn influences the infiltration of immune cells into peripheral blood and other tissues. To explore these dynamics, we performed comprehensive profiling of BM immune cell composition in hypoxic WT and *Irg1*$^{-/-}$ mice using FACS. Unexpectedly, we observed a significant increase in the total immune cell population in *Irg1*$^{-/-}$ BM compared to WT (Figure 4.12.A). While the number of mature monocytes (CD45^{+}CD11b^{+}Ly6C^{+}) increased significantly in the *Irg1*$^{-/-}$ mice, the overall macrophage (CD45^{+}CD11b^{+}Ly6C^{+}F4/80^{+})composition decreased significantly (Figure 4.12.B). The number of DCs (CD45^{+}CD11c^{+}) tended to decrease in the *Irg1*$^{-/-}$ mice (Figure 4.12.C). In contrast, the proportion of neutrophils (CD45^{+}CD11b^{+}Ly6G^{+}) and T cells (CD45^{+}CD11b^{-}CD3^{+}) remained unchanged; however, the populations of mature B cells (CD45^{+}CD11b^{-}CD19^{+}) were also decreased in *Irg1*$^{-/-}$ mice compared to WT mice under hypoxia (Figure 4.12.D). These data suggest that macrophage and DC populations are increased in the lung, while these populations are simultaneously reduced in the ground tissue of hypoxic *Irg1*$^{-/-}$ mice, possibly due to increased infiltration into the bloodstream.

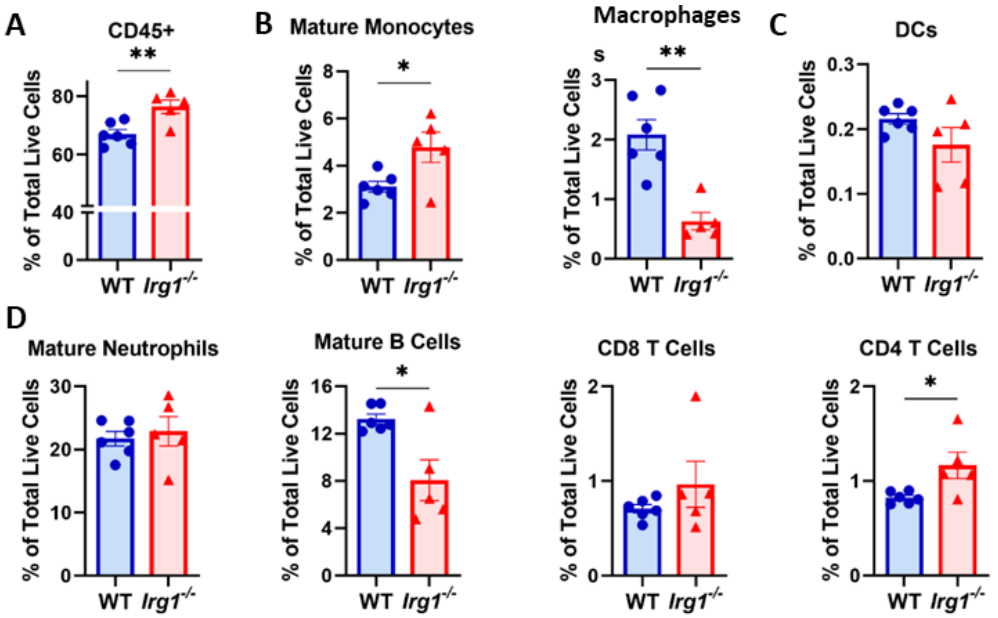

Figure 4.12: Impaired myeloid cells composition in the BM of hypoxic *Irg1*$^{-/-}$ mice. A-D) FACS immunoprofiling was performed on BM cells from hypoxia-exposed WT and *Irg1*$^{-/-}$ mice, with immune cell populations quantified as a percentage of total live cells detected. A) Total immune cells (CD45^{+}). B) Mature monocytes (CD45^{+}CD11b^{+}Ly6C^{+}) and total macrophages (CD45^{+}CD11b^{+}Ly6C^{+}F4/80^{+}). C) DCs (CD45^{+}CD11c^{+}). D) Mature neutrophils (CD45^{+}CD11b^{+}Ly6G^{+}), mature B cells (CD45^{+}CD11b^{-}CD19^{+}) and T cells (CD45^{+}CD11b^{-}CD3^{+}). DCs: dendritic cells. *n* = 6 for WT. *n* = 5 for *Irg1*$^{-/-}$. The error bars indicate the mean value with SEM. Data were analyzed with unpaired Student's *t*-test. *p<0.05. **p<0.01.

4.13. The composition of myeloid lineage-derived cells is significantly elevated in patients with group 1 PH.

Peripheral blood immune cell profiling of two cohorts, i.e., non-PH patients and Group 1 PH patients, revealed a 12% increase in myeloid lineage-derived immune cells in Group 1 PH patients. This finding is consistent with the phenotypes observed in *Irg1*$^{-/-}$ mice, which also exhibit impaired myeloid cell composition in the BM and lungs in PH, in the form of increased infiltration of myeloid cells in lung tissue (Figure 4.13).

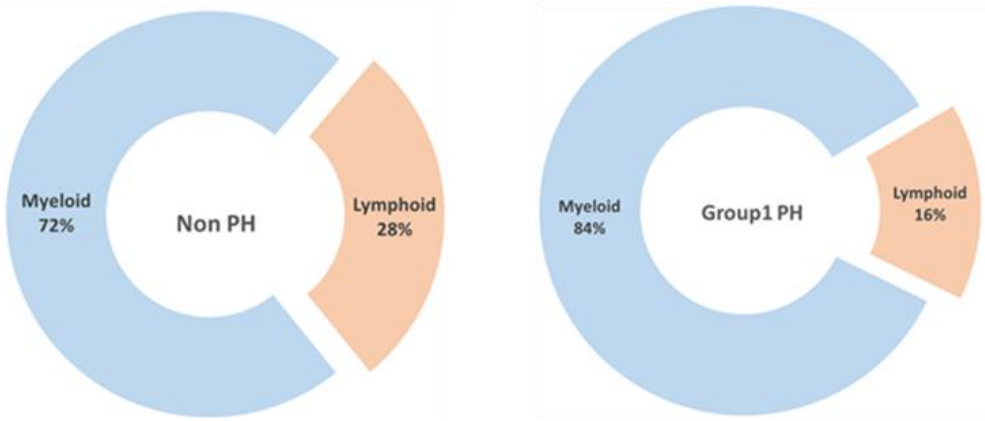

Figure 4.13: Enhanced myeloid cells population in group-1 PH patients. The donut diagrams show the proportions of myeloid and lymphoid cells in the peripheral blood of Non PH (left, *n* = 13) and Group 1 PH (right, *n* = 27).

4.14. Proinflammatory BMDMs and PBMC-derived macrophages are the predominant cells expressing *Irg1* in mice.

To characterize the cellular origins of *Irg1* expression in mice, we investigated the expression profiles of *Irg1* using the BioGPS databases. The analysis showed that *Irg1* was highly and specifically expressed in PBMC and BMDMs that had been chronically stimulated and polarized to M1 macrophages (Figure 4.14).

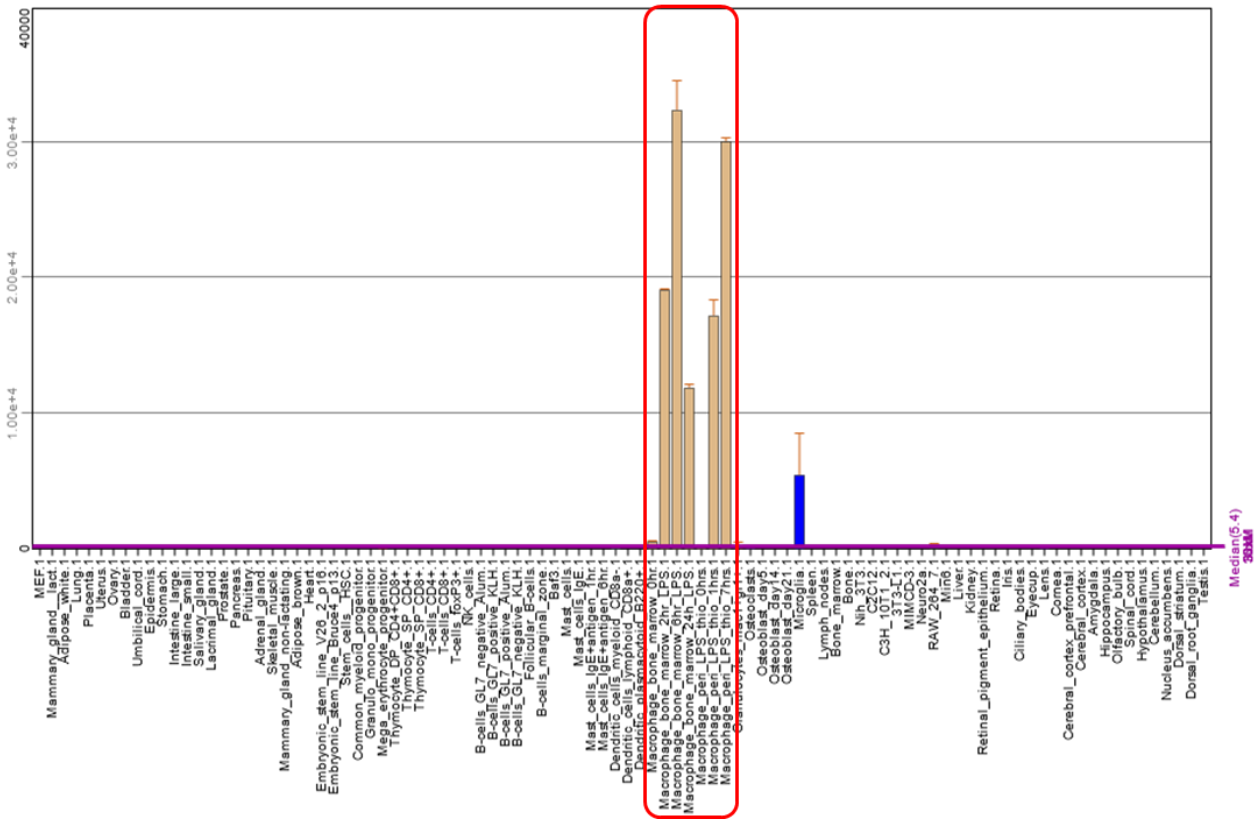

Figure. 4.14: Irg1-expressing cells in the mouse BioGPS dataset of Mus musculus.

4.15. Irg1-deficient proinflammatory BMDMs induce cardiac hypertrophy and failure markers in neonate cardiomyocytes as a paracrine effect.

The increased presence of CD45^{+} cells, particularly macrophages, in the hearts of *Irg1*$^{-/-}$ mice indicates a remarkable interaction with the structural cells of the heart. This interaction is important to understand how proinflammatory BMDMs responsible for *Irg1* expression and Itaconate production in mice affect cardiac fibroblasts and cardiomyocytes, which play a key role in cardiac fibrosis and hypertrophy. To investigate the *Irg1*$^{-/-}$paracrine effects of the proinflammatory BMDMs of *Irg1*$^{-/-}$ on cardiomyocytes, BM cells were isolated from WT and

Irg1$^{-/-}$ mice, differentiated into BMDMs using murine Mcsf, and subsequently polarized into M1 macrophages by LPS stimulation. The conditioned media (CM) of WT and *Irg1*$^{-/-}$ M1 macrophages were then used to stimulate WT neonatal cardiomyocytes (nCM) (Figure 4.15.A). Irg1 protein expression was completely absent in *Irg1*$^{-/-}$ M1 macrophages, whereas WT-M1 macrophages exhibited high *Irg1* expression (Figure 4.15.B). Compared to WT-M1 macrophages, *Irg1*$^{-/-}$ M1 macrophages exhibited a distinct proinflammatory phenotype through significantly increased *IL-1β* expression (Figure 4.15.C). *Nppb* and *Nppa*, the markers that are reactivated during HF, showed a trend to increase in mRNA level in nCM treated with *Irg1*$^{-/-}$ M1-macrophage conditioned medium, while the upregulation of *Nppb* was more pronounced (Figure 4.15.D). Remarkably, treatment of nCM with *Irg1*$^{-/-}$ M1-macrophage CM resulted in significant upregulation of myosin heavy chain 7 (*Myh7*) expression and downregulation of myosin heavy chain 6 (*Myh6*) (Figure 4.15.B), which significantly altered the ratio of *Myh7* to *Myh6* in nCM treated with CM from *Irg1*$^{-/-}$ M1 macrophages compared to controls (Figure 4.15.E-F).

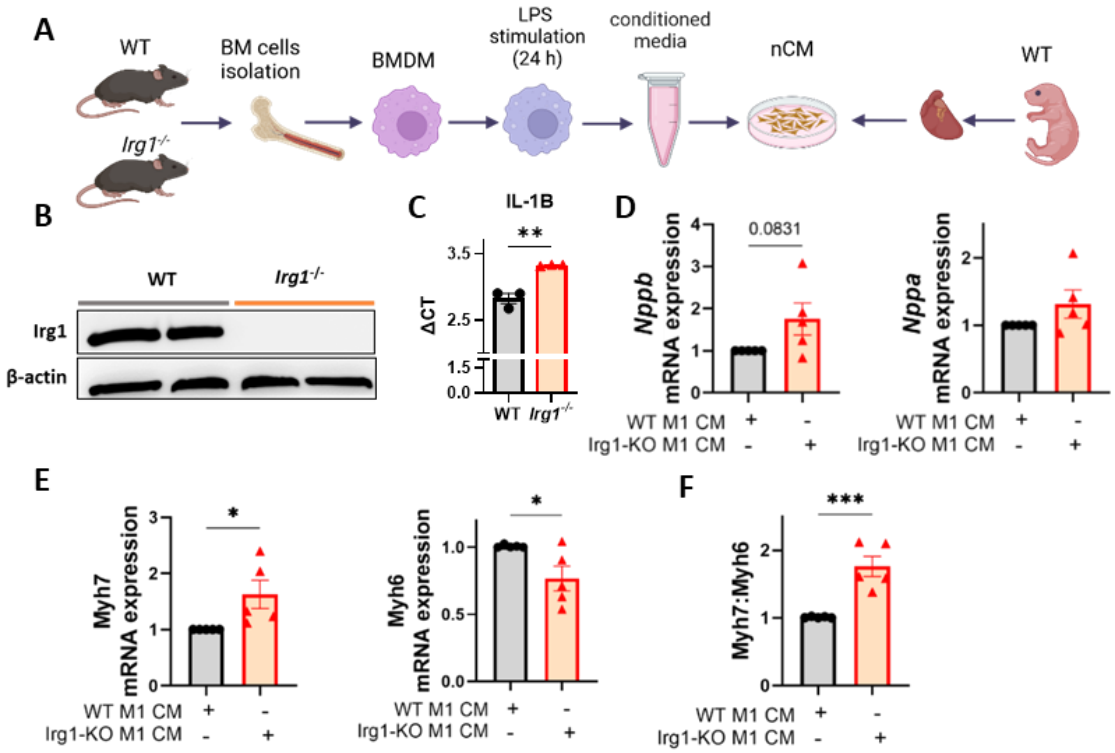

Figure. 4.15: Upregulation of markers of HF in neonatal cardiomyocytes treated with conditioned media of *Irg1*-deficient M1 macrophages. A) Schematic representation of the *in vitro* experimental model: BMDMs from WT and *Irg1*$^{-/-}$ mice were polarized to M1 macrophages for 24 h by LPS stimulation. The conditioned medium (CM) was then collected from the cells. Neonatal WT cardiomyocytes were then treated with CM from either WT- or *Irg1*$^{-/-}$ M1-polarized BMDMs to examine the paracrine effect on cardiac cells. Created with BioRender.com. B) Representative images of protein levels of *Irg1*, determined by WB analysis, and β-actin (n = 2 per group). C) *IL-1β* mRNA expression (ΔCT) in WT and *Irg1*$^{-/-}$ M1 macrophages (n = 3 per group). D) *Nppb* and *Nppa* and E) *Myh7* and *Myh6* mRNA expression

(fold change) in nCM treated with WT or *Irg1*$^{-/-}$ M1 macrophages CM (*n* = 5 per group). F) Ratio of *Myh7* expression to *Myh6* expression. The error bars indicate the mean value with SEM. Data were analyzed with unpaired Student's *t*-test *p<0.05, **p<0.01, ***p<0.001.

4.16. *IRG1*-silenced M1 macrophages stimulate proliferation and pro-fibrotic phenotype in cardiac fibroblasts.

To investigate the paracrine effects of IRG1-deficient M1 macrophages on human cardiac fibroblasts (CFs), we knocked down *IRG1* in macrophages derived from PBMCs from human donors using *IRG1*-targeted siRNA (siIRG1) (Figure 4.16.A). This approach efficiently reduced *IRG1* expression compared to control siRNA (siControl). After silencing *IRG1*, macrophages were polarized to the M1 phenotype with LPS and IFNγ for 24 hours, which enhanced their proinflammatory response as shown by increased levels of IL-1β and IL-6 compared to controls (Figure 4.16.B). CM from these transfected M1 macrophages were then applied to CFs and PASMCs to assess the effects on cell proliferation and pro-fibrotic phenotype. Of note, periostin (*POSTN*), *ACTC1* and *COL1A2*, the genes responsible for ECM development and cell adhesion in cardiac tissue, were significantly upregulated in CFs treated with CM from siIRG1-M1 macrophages compared to controls (Figure 4.16.C). In addition, Both PASMCs and CFs treated with CM of siIRG1-M1 macrophages exhibited a significant increase in cell proliferation without a corresponding increase in cell apoptosis (Figure 4.16.D-E).

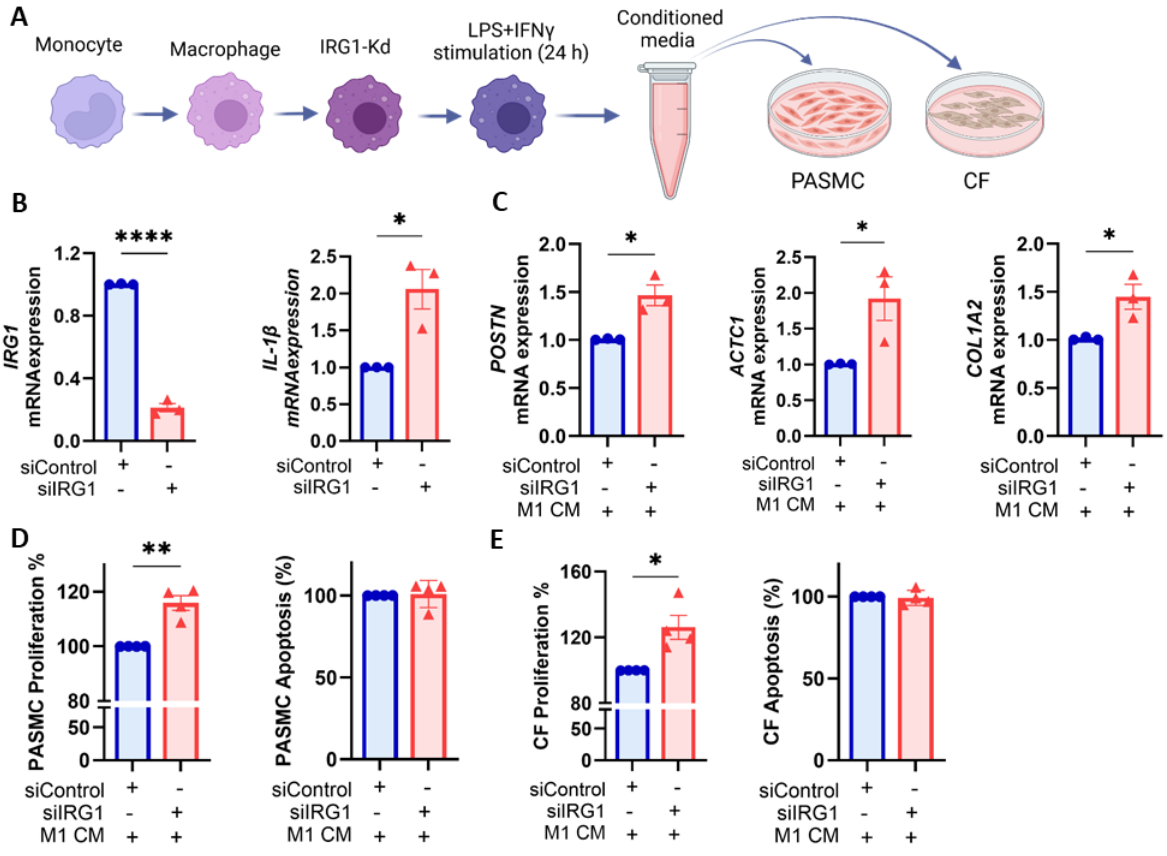

Figure. 4.16: Hyperproliferative and pro-fibrotic phenotype in cardiac fibroblasts treated with *IRG1*-silenced M1 macrophage conditioned media. A) PBMCs from human donors were differentiated into macrophage followed by *IRG1* silencing. Cells were then polarized into the M1 phenotype by LPS + IFNγ stimulation for 24 hours. Conditioned medium (CM) from the *Irg1*-silenced M1 macrophages was collected after 24 hours and subsequently used to treat human pulmonary arterial smooth muscle cells (PASMCs) and cardiac fibroblasts (CFs). After 24 hours of treatment, the growth and phenotype of CFs and PASMCs were assessed using BrdU incorporation and cell death detection assays to evaluate proliferation and apoptosis, respectively, and qPCR to measure the expression of fibrotic markers in CFs. Created with BioRender.com. B) mRNA expression (fold change) of *IRG1*, *IL-1β* in siControl and siIRG1 PBMC-derived M1 (*n* = 3). D) mRNA expression (fold change) of *POSTN*, *ACTC1* and *COL1A2* in CFs treated with CM of siControl and siIRG1-M1 macrophages (*n* = 3). C-D) Percentage of cell proliferation (left) and cell apoptosis (right) of C) PASMCs and D) CFs treated with siControl and siIRG1 CM (*n* = 4). The error bars indicate the mean value with SEM. Data were analyzed using unpaired Student's *t*-test *p<0.05, **p<0.01, ****p<0.0001.

4.17. *Irg1*$^{-/-}$ BM cells contribute to cardiac hypertrophy and dysfunction.

To investigate the contribution of the hematopoietic organ BM, to the cardiac phenotype of *Irg1*$^{-/-}$ mice, we transplanted WT-irradiated mice with either WT or *Irg1*$^{-/-}$ BM cells (Figure 4.17.A). *Irg1*$^{-/-}$ BM recipient mice developed marked RV hypertrophy compared to WT BM recipient mice, as evidenced by a significantly increased Fulton index (RV/LV+S) and RV mass to body weight ratio (RV/BW), as well as a marked tendency towards an increased LV + septal mass to body weight ratio (LV+S/BW) (Figure 4.17.B). However, body weight remained constant between groups (Figure 4.17.C). *Irg1*$^{-/-}$-BM recipient mice showed deterioration in echocardiographically determined cardiac functional parameters, including decreased CI, SVI and LVEF, although their heart rate was comparable to that of WT-BM recipient mice (Figure 4.17.D-F).

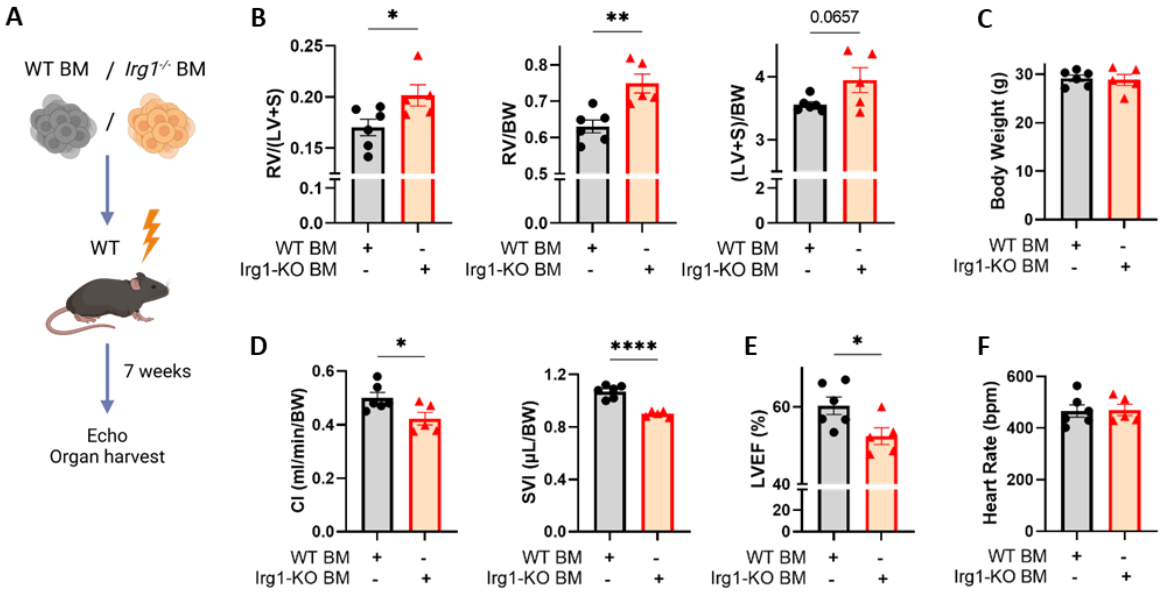

Figure 4.17: LV and RV remodeling in *Irg1*$^{-/-}$-BM recipient mice. A) Schematic representation of the bone marrow (BM) transplantation model: WT-irradiated mice were transplanted with BM cells from WT or *Irg1*$^{-/-}$ mice and their hearts were analyzed by echocardiography. Schematic figure was created with BioRender.com. B) Fulton index (RV/(LV+septum)) (left), ratio of RV mass to body weight (center) and LV plus septal mass to body weight ((LV+S)/BW) (right) C) Body weight. D) CI and SVI. E) LVEF. *n* = 5-6 mice per group. CI: cardiac output ratio to body weight; SV: stroke volume ratio to body weight; LVEF: LV ejection fraction. The error bars indicate the mean value with SEM. Data were analyzed using two-way ANOVA and unpaired Student's *t*-test *p<0.05, **p<0.01, ****p<0.0001.

4.18. *Irg1*$^{-/-}$-BM recipient mice did not develop vascular remodeling.

Pulmonary vascular remodeling was investigated in BMT mice. *Irg1*$^{-/-}$- BM recipient mice showed no increase in medial wall thickness or percentage of muscularization in the pulmonary vasculature compared to mice transplanted with WT BM cells (Figure 4.18.A-C). These results suggest that the PH phenotype observed in *Irg1*$^{-/-}$ mice may be a secondary consequence of LV hypertrophy and dysfunction, ultimately leading to postcapillary PH. Therefore, longer follow-up of BMT mice after transplantation is needed to further investigate progression of pulmonary vascular remodeling and cardiac phenotype. In addition, exposing the BMT mice to a second stress, e.g., hypoxia, could be beneficial for further evaluation of the PH-related phenotype.

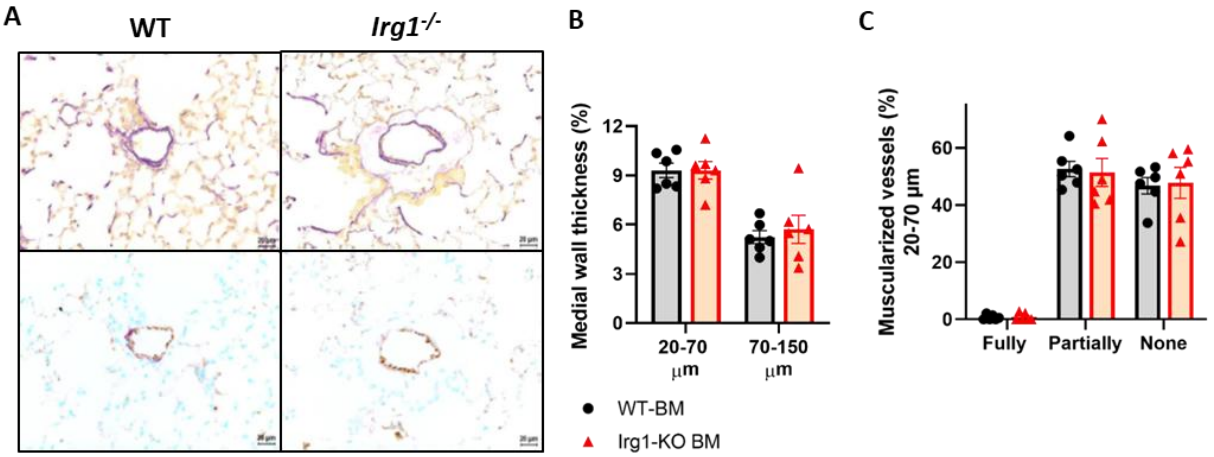

Figure 4.18: Evaluation of pulmonary vascular remodeling in WT and *Irg1*$^{-/-}$ BM recipient mice. A) Representative images of medial wall thickness (elastin, top) and immunostaining with vWF and α-actin (bottom) staining. B) Percentage of thickening of the medial wall of the pulmonary vessels. C) Percentage of fully, partially and non-muscularized pulmonary vessels (20–70 µm diameter). *n* = 6 lungs per group. Scale bars: 20µm. Error bars indicate the mean with SEM. Data were analyzed with two-way ANOVA.

4.19. *Irg1*-expressing cells are expanded in the BM niche following acute myocardial infarction.

Since *Irg1*-deficient BM cells have a direct impact on the cardiac phenotype, we wanted to investigate the expression of *Irg1* in BM cells under conditions of CVD. To this end, we reanalyzed a publicly available single-cell transcriptome dataset from Hoffmann et al. (165), investigating the effects of AMI on the vascular niche of mouse BM. In the cluster analysis, *Irg1*-expressing cells were predominantly found in clusters 2, 8 and 10 of 17 identified clusters in the vascular niche of mouse BM, with a significantly higher population in cluster 2 (Figure 4.19.A-C). Surprisingly, *Irg1*-expressing cells showed a significant increase on day 7 post-MI (Figure 4.19.D). However, the specific contribution of *Irg1*-expressing cells to AMI in mice and their role in the differentiation of BM cells, which are the primary hematopoietic site in adult humans, remains unclear.

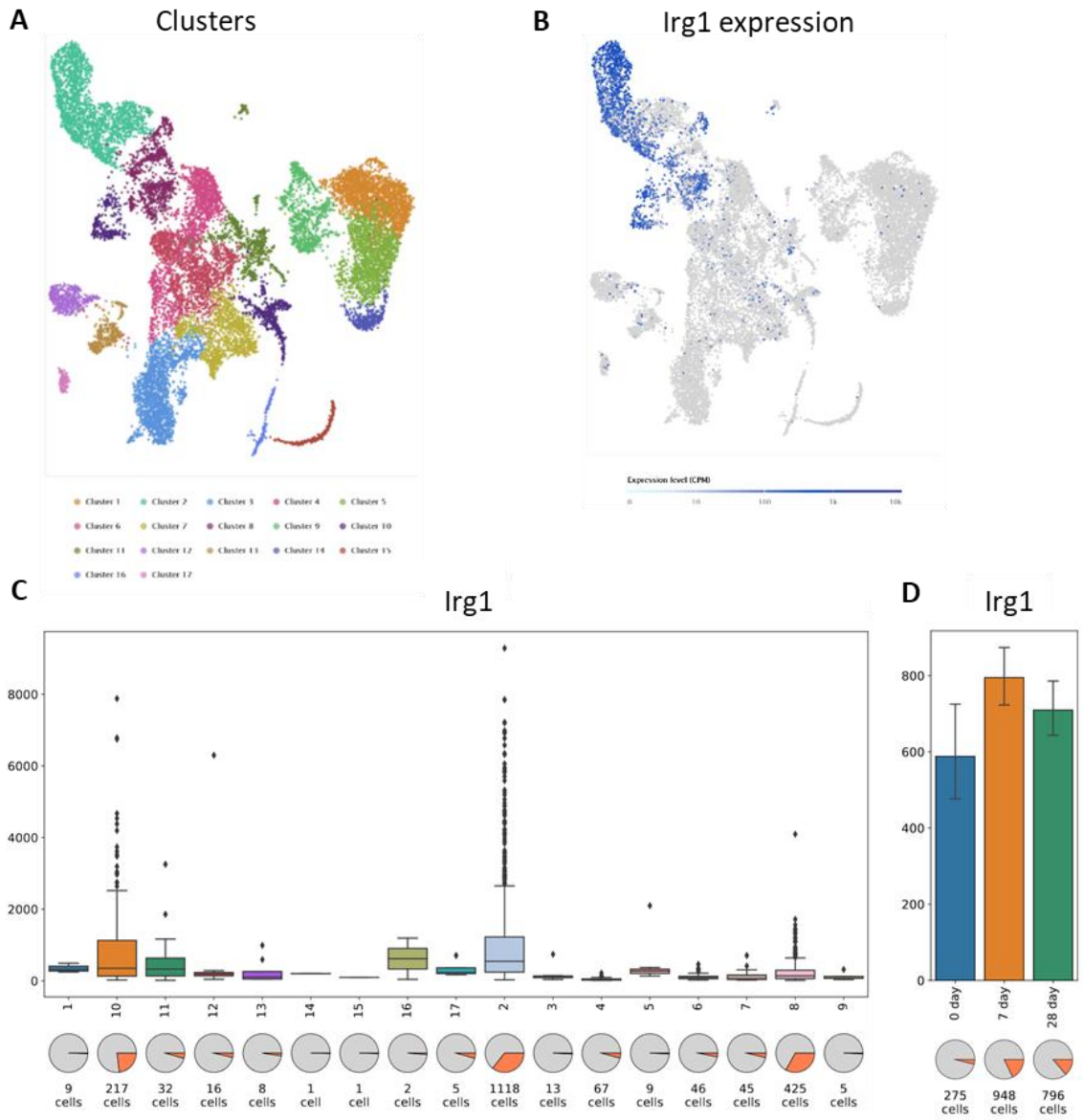

Figure 4.19: *Irg1* upregulation in BM cells on day 7 after MI. A-C) scRNA-seq analysis of the vascular BM niche in mice at three time points: 7 days (7 days) and 28 days (28 days) after myocardial infarction, together with controls (0 days). A) Clustered cells from all time points are visualized in t-SNE plots, B) with *Irg1*-expressing cells highlighted in blue. C) Enrichment

of *Irg1* expression *Irg1*in clusters 2, 8 and 10. D) Number of *Irg1*-expressing cells in 3 time points.

4.20. Irg1/Itaconate deficiency impairs HSC differentiation and expansion.

Since HSPCs are the origin of all blood and immune cells, we performed phenotypic analysis of HSCs (Figure 4.20.A) in WT and *Irg1*$^{-/-}$ BM samples by FACS to assess the effects of the Irg1/Itaconate axis on HSC differentiation and frequency. *Irg1*$^{-/-}$ mice had comparable amounts of HSCs to WT controls, including LSKs (Lineage^{-}Sca1^{+}cKit^{+}) and ST-HSCs (LSK CD150^{-} CD48^{-}) (Figure 4.20.B), while the composition of LT-HSCs (LSK CD150^{+}CD48^{-}), which are characterized by stem states with quiescence and self-renewal, was significantly reduced in *Irg1*$^{-/-}$-BM (P-value = 0.087) *Irg1*$^{-/-}$ (Figure 4.20.C). Differentiation evaluation of multi-potent progenitors revealed a distinct differentiation into downstream progenitors, MPP^{Ly} (LK CD150^{-} CD135^{+}) in *Irg1*$^{-/-}$ mice, while MPP^{GM} (LK CD150^{-}CD135^{-}CD48^{+}) and MPP^{MkE} (LK CD150^{+}CD135^{-}CD48^{+}) showed no significant differences compared to WT controls (Figure 4.20.D). In addition, the population of granulocyte-monocyte progenitors (GMP, Lin^{-}Sca1^{-} cKit^{+}CD150^{-}CD16/32^{+}CD34^{+}) showed a clear trend towards expansion in *Irg1*$^{-/-}$ BM (Figure 4.20.E). In addition to dysregulations in differentiation profile of HSCs in *Irg1*$^{-/-}$ BM, cKit^{+} sorted cells of *Irg1*$^{-/-}$ mice demonstrated a significant upregulation of IL-1β in mRNA level compared to WT control. These results suggest that the Irg1/Itaconate axis plays a critical role in regulating the balance of hematopoietic lineages, particularly by influencing long-term self-renewal in LT-HSCs, which favors lineage priming of MPP^{Ly} to promote the expansion of granulocyte-monocyte progenitors. This underscores the far-reaching effects of *Irg1* on HSC function and lineage differentiation pathways.

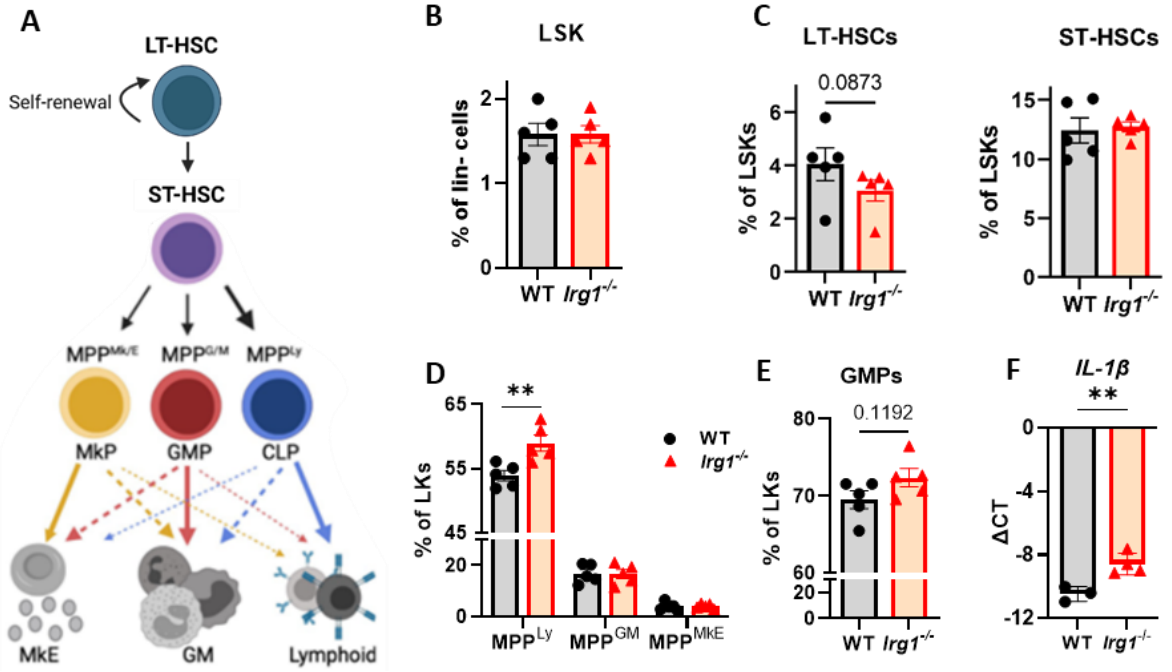

Figure 4.20: Impaired HSC differentiation in *Irg1*$^{-/-}$ BM. A) Schematic representation of the hierarchical models of hematopoiesis. The topmost HSC pool, referred to as long-term (LT-) HSCs, comprises largely dormant with highest self-renewal potential giving rise to short-term (ST-) HSCs. ST-HSCs are poised to exit quiescence faster than LT-HSCs with transient repopulation potential differentiating into multipotent progenitor cells (MPP) with different lineage propensities: MPP^{Ly} for the lymphoid lineage, MPP^{GM} for the granulocyte-monocyte lineage and MPP^{MkE} for the megakaryocyte-erythrocyte lineage, which then give rise to the corresponding mature cell types such as megakaryocyte progenitor (MkE), granulocyte-monocyte progenitor (GMP) and common lymphoid progenitor (CLP). B-E) FACS phenotyping of HSCs, B) Quantification of LSK (Lin$^-$Sca1$^+$cKit$^+$) as a percentage of lineage-negative (Lin$^-$) cells. C) Frequency of LT-HSCs (long-term HSCs, right) and ST-HSCs (short-term HSCs, left) within the LSK population in WT and *Irg1*$^{-/-}$ mice. D) Composition of MPP subpopulations (MPP^{Ly}, MPP^{GM} and MPP^{MkE}) as a percentage of LK (Lin−c-Kit+) cells. E) Frequency of GMPs as a percentage within the LK population. (*n* = 5 per group for FACS). F) *IL-1β* mRNA expression in cKit$^+$ cells, measured by qPCR (*n* = 3 in WT, *n* = 4 in *Irg1*$^{-/-}$). Error bars indicate the mean with SEM. Data were analyzed with unpaired Student's *t*-test. **p<0.01.

4.21. RNA-seq analysis reveals distinct transcriptional alterations in *Irg1*$^{-/-}$ LKs.

To further elucidate the mechanisms underlying impaired hematopoiesis in *Irg1*$^{-/-}$ HSCs, we sorted two distinct subpopulations of BM cells by FACS: LKs and MPP^{Ly} populations. Total RNA was extracted from these cells and subjected to bulk RNA sequencing to analyze gene expression profiles. PCA of RNA-seq data from LKs revealed that biological replicates (n = 4 per group) of both WT LKs and *Irg1*$^{-/-}$ LKs were tightly clustered within their respective groups. These clusters were clearly separated along the first two principal components, PC1 and PC2, which accounted for 28.8 % and 21.2 % of the total variance, respectively (Figure 4.21.A). The differential expression analysis, visualized by a volcano plot, shows the statistical significance of the gene expression changes with the negative log10 of the false discovery rate (−log10 FDR) on the y-axis and the log2 fold change (log2 FC) on the x-axis. A total of 213 DEGs were identified. Among them, 133 DEGs were upregulated (shown as red dots) and 80 genes were downregulated (shown as blue dots) in *Irg1*$^{-/-}$ LKs (log2FC <> ± 0.58) (Figure 4.21.C). The 50 most significant DEGs, based on the largest absolute fold change (FDR < 0.05), were plotted in a heatmap (Figure 4.21.D), highlighting the different expression patterns between the two groups. These results suggest that loss of *Irg1* significantly alters the transcriptional landscape of HSCs, possibly contributing to the impaired hematopoiesis observed in *Irg1*$^{-/-}$ mice.

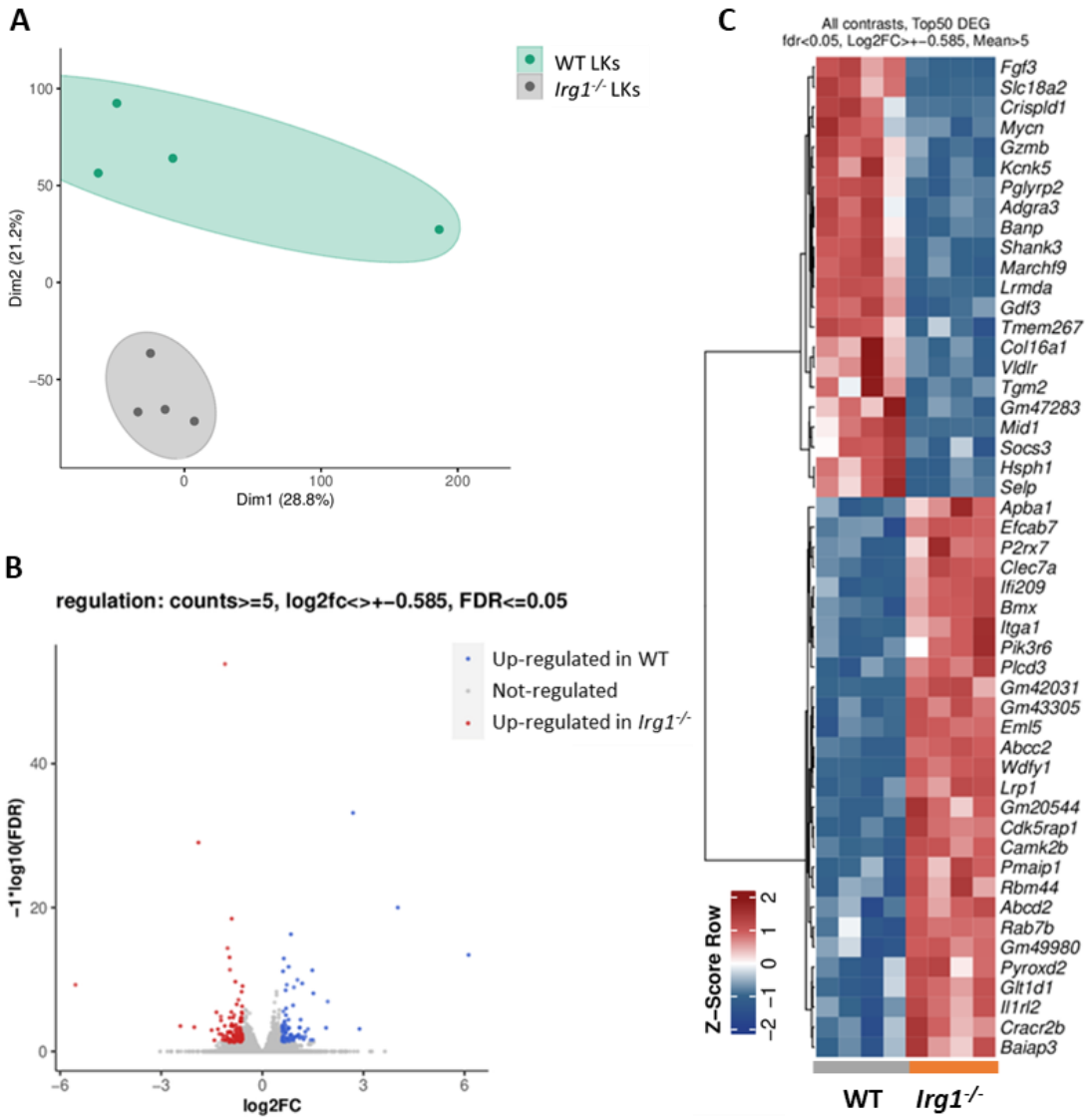

Figure 4.21: Transcriptomic profiling of WT and *Irg1*$^{-/-}$ LKs. A) Principal component analysis (PCA) of WT and *Irg1*$^{-/-}$ LKs showing the distribution of the gene profile of each sample. WT samples are shown in green and *Irg1*$^{-/-}$ samples in gray. B) Volcano plot of all genes detected in the mass RNA-seq. The X-axis is the log2 base fold change (log2FC) and the Y-axis is the −log10 base false discovery rate (-log10FDR). C) The heatmap shows the top 50 DEGs between WT and *Irg1*$^{-/-}$ LKs based on log2FC (<> ± 0.58) and statistical significance (FDR < 0.05). Each row represents one DEG, and each column represents one sample. Red: representation of upregulated DEGs and blue: representation of downregulated DEGs in *Irg1*$^{-/-}$ LKs. (n = 4 per group).

4.22. Irg1-deficiency drives enrichment of NLRP3 inflammasome and purine metabolism pathways in LKs.

GSEA of differentially regulated genes in *Irg1*$^{-/-}$ LKs compared to WT LKs highlights the 10 most enriched pathways in both the upregulated and downregulated categories, based on Reactome pathways with an FDR cutoff of <0.2. In *Irg1*$^{-/-}$ LKs, significant upregulation of

inflammation-related pathways is observed, particularly the NLRP3 inflammasome signaling pathway, which is a key mediator of innate immune activation. The NLRP3 inflammasome is known to drive the production of proinflammatory cytokines such as IL-1β, affecting the BM microenvironment and potentially impairing hematopoiesis. The involvement of ERBB2-related signaling pathways in cell motility and inflammation underscores the inflammatory phenotype of *Irg1*$^{-/-}$ LKs, as these pathways can promote immune cell migration and inflammatory responses. Interestingly, purine catabolism is also upregulated in *Irg1*$^{-/-}$ LKs (Figure 4.22). Purine catabolism plays a crucial role in the degradation of purine nucleotides to generate energy and metabolic intermediates. This metabolic shift could be a compensatory mechanism to support increased immune activity in *Irg1*$^{-/-}$ LKs, but it could also contribute to cellular stress over time, potentially affecting HSC function and homeostasis. The significant upregulation of Purinergic Receptor P2X 7 (P2rx7) in *Irg1*$^{-/-}$ LKs suggests enhanced purinergic signaling due to increased extracellular ATP acting in synergy with NLRP3 inflammasome activation. This dual activation likely promotes the mobilization of LKs and the egress of HSC cells from the BM. This reveals a mechanism by which enhanced purinergic signaling and inflammasome activity disrupt HSC dynamics and impair hematopoiesis under *Irg1*-deficient conditions.

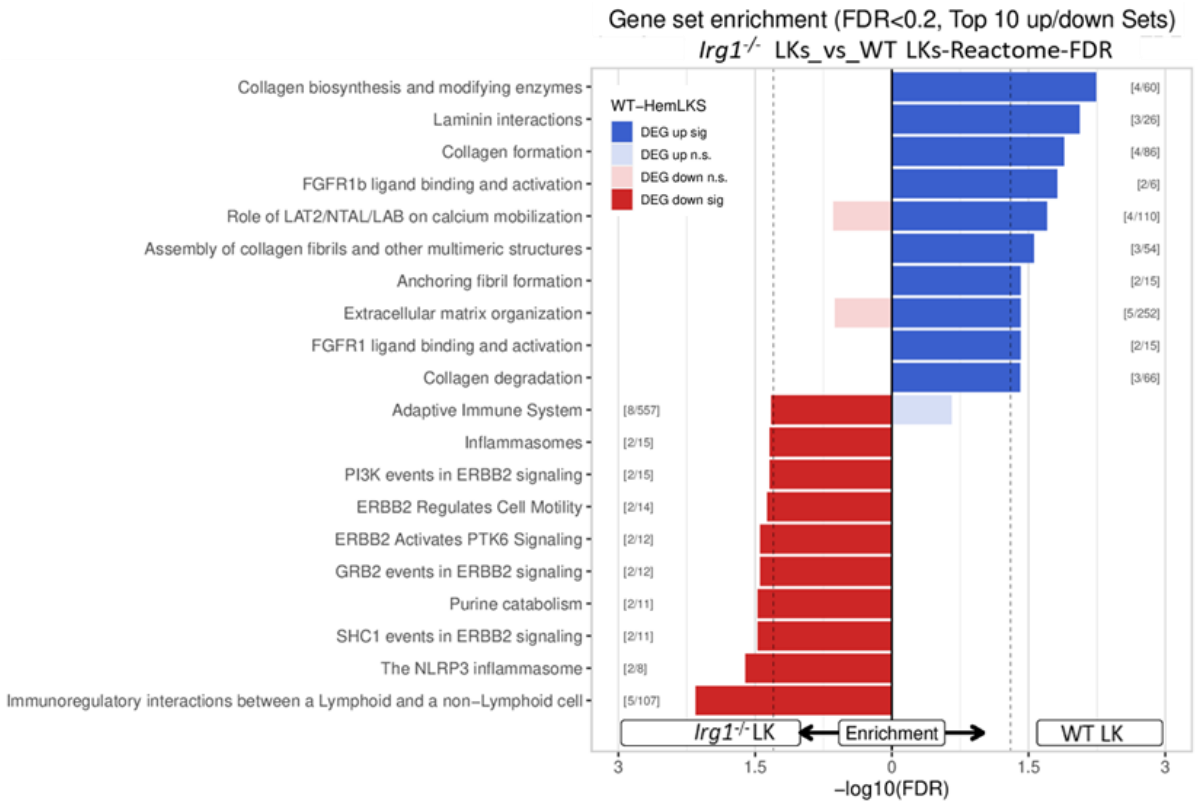

Figure. 4.22: GSEA analysis between WT LK and *Irg1*$^{-/-}$ LK. The 10 most enriched reactome pathways (FDR < 0.2) when comparing WT and *Irg1*$^{-/-}$ LK cells. Bars show –log10(FDR) scores, where blue represents downregulated and red represents upregulated pathways in *Irg1*$^{-/-}$ LKs.

4.23. RNA-seq analysis reveals distinct transcriptomic signature in *Irg1*$^{-/-}$ MPP^{Ly}.

Considering that the MPP^{Ly} subpopulation had the most significant changes in *Irg1*$^{-/-}$-BM, it was crucial to gain insight into the transcriptomic changes within this specific group. PCA of WT and *Irg1*$^{-/-}$ MPP^{Ly} populations (n = 3 per group) shows a clear separation along Dim1 and Dim2, accounting for 30.7% and 25.5% of the total variance, respectively (Figure 4.23.A). This segregation highlights the unique transcriptional profiles of WT MPP^{Ly} (green) compared to *Irg1*$^{-/-}$ MPP^{Ly} (gray), with each group showing tight clustering between replicates. Differential expression analysis, illustrated by the volcano plot (Figure 4.23.B), shows the statistical significance of gene expression changes (−log10 FDR) on the y-axis versus the log2FC scale on the x-axis. Genes that are significantly upregulated in *Irg1*$^{-/-}$ MPP^{Ly} are represented by red dots, while those that are upregulated in WT are shown as blue dots. A total of 156 DEGs were identified, with 132 genes upregulated in *Irg1*$^{-/-}$ and 24 downregulated. *Irg1*$^{-/-}$ The heatmap highlights the top 50 DEGs with the highest absolute fold changes and provides a clear visualization of the most striking gene expression differences between the two genotypes and illustrates the transcriptional shifts in *Irg1*$^{-/-}$ MPP^{Ly} cells (Figure 4.23.C).

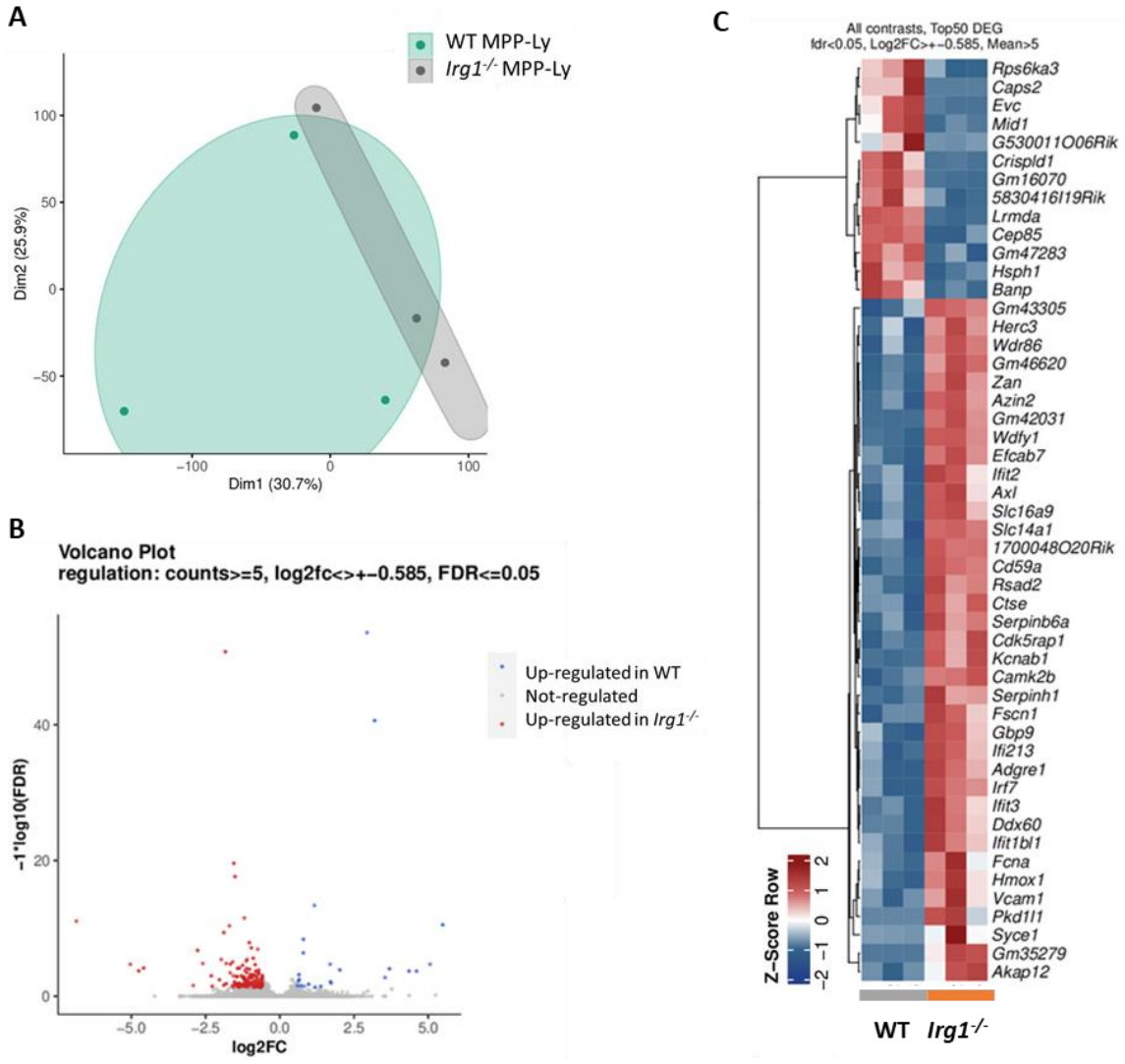

Figure 4.23: Transcriptomic profiling of WT and *Irg1*$^{-/-}$ MPP^{Ly}. A) PCA of WT and *Irg1*$^{-/-}$ MPP^{Ly} showing the distribution of the gene profile of each sample. WT samples are shown in green and *Irg1*$^{-/-}$ samples in gray. B) Volcano plot of all genes detected in the bulk RNA-seq. The X-axis is the log2 base fold change (log2FC) and the Y-axis is the −log10 base false discovery rate (-log10FDR). C) The heatmap shows the top 50 DEGs between WT and *Irg1*$^{-/-}$ MPP^{Ly} based on log2FC (<> ± 0.58) and statistical significance (FDR < 0.05). Each row represents one DEG and each column represents one sample. Red: represents the upregulated DEGs and blue: represents the downregulated DEGs in *Irg1*$^{-/-}$ MPP^{Ly}. (*n* = 3 per group).

4.24. Interferon-associated inflammatory signaling and complement pathway activation are upregulated in *Irg1*$^{-/-}$ MPP^{Ly}.

GSEA of *Irg1*$^{-/-}$ MPP^{Ly} compared to WT MPP^{Ly} populations using Gene Ontology with an FDR cutoff of <0.2 shows that *Irg1*$^{-/-}$ MPP^{Ly} cells display enrichment of inflammatory and immune response pathways, consistent with findings in LKs, including innate immune response–activating signal transduction, cellular response to interferon-beta, cellular response to interferon-alpha, and complement activation, classical pathway. In addition, the enrichment of the nucleoside diphosphate synthesis pathway associated with purine metabolism indicates a requirement for nucleotide resources. The overlap of these immune and metabolic pathways between MPP^{Ly} and LKs suggests a consistent inflammatory and metabolically active state in *Irg1*$^{-/-}$ HSC subpopulations that affects hematopoietic differentiation and fate (Figure 4.24).

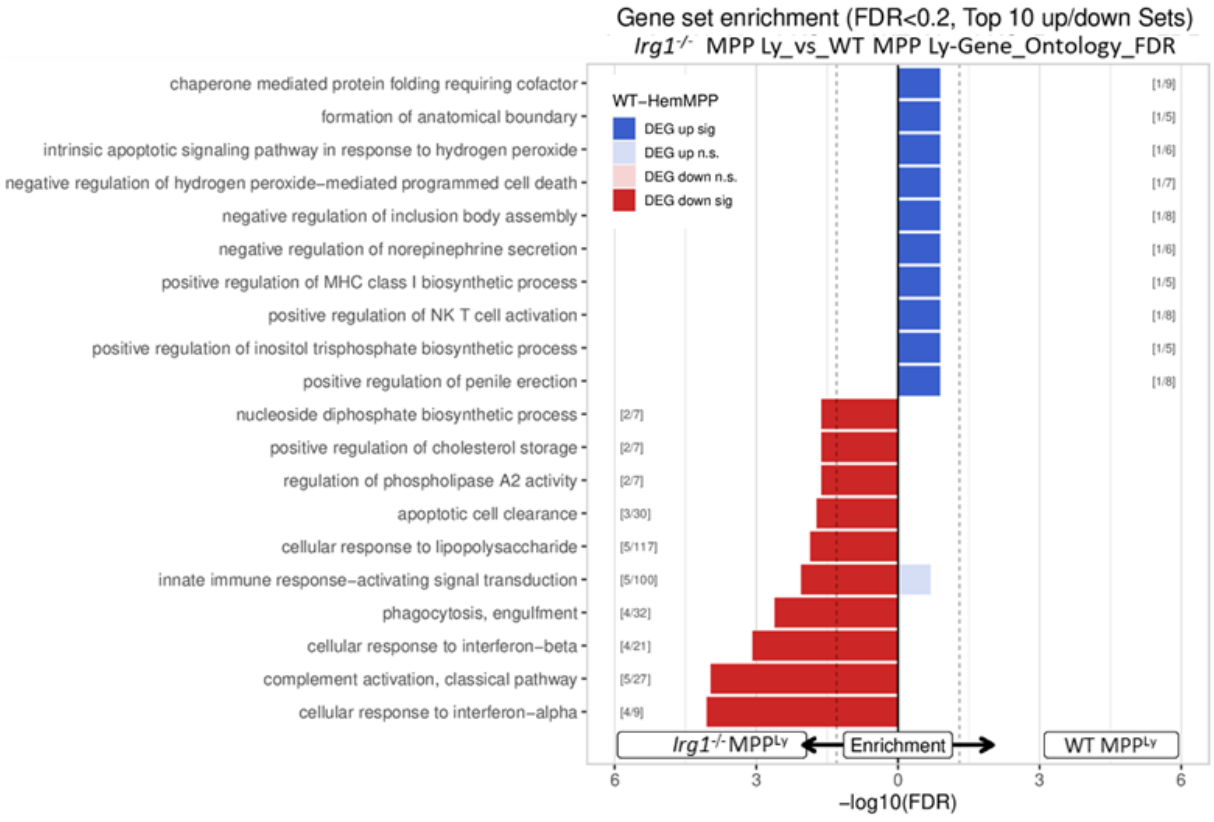

Figure. 4.24: GSEA analysis between WT MPP^{Ly} and *Irg1*$^{-/-}$ MPP^{Ly}. Top 10 enriched gene ontology (FDR < 0.2) compared between WT and *Irg1*$^{-/-}$ LK cells. Bars show –log10 (FDR) scores, where blue represents upregulated and red represents downregulated pathways in *Irg1*$^{-/-}$ MPP^{Ly}.

4.25. Loss of *Irg1* disrupts purine metabolism in LKs.

To investigate the role of the *Irg1*/itaconate axis as an immunometabolic regulator for the metabolic profile of LKs, a metabolomic analysis was performed on these cells. Among the metabolites analyzed, we focused on those involved in the purine pathway, as genes within this pathway showed significant changes in their transcriptomic profiles in *Irg1*$^{-/-}$ LKs (Figure 4.25.A). In particular, the levels of purine nucleotides, adenine and guanosine were significantly reduced in *Irg1*$^{-/-}$ LKs (Figure 4.25.B). Although the concentrations of guanosine monophosphate (GMP) and inosine monophosphate exhibited a notable reduction in *Irg1*$^{-/-}$ LKs, the diphosphate metabolites remained unchanged between *Irg1*$^{-/-}$ and WT-LKs (Figure 4.25.C). Conversely, these cells exhibited a marked increase in nucleoside triphosphates of the purine pathway, including adenosine triphosphate (ATP), guanosine triphosphate (GTP) and inosine triphosphate (ITP) (Figure 4.25.D). These results suggest that loss of *Irg1* disrupts purine metabolism and alters the expression of enzymes that are critical for regulating this metabolism.

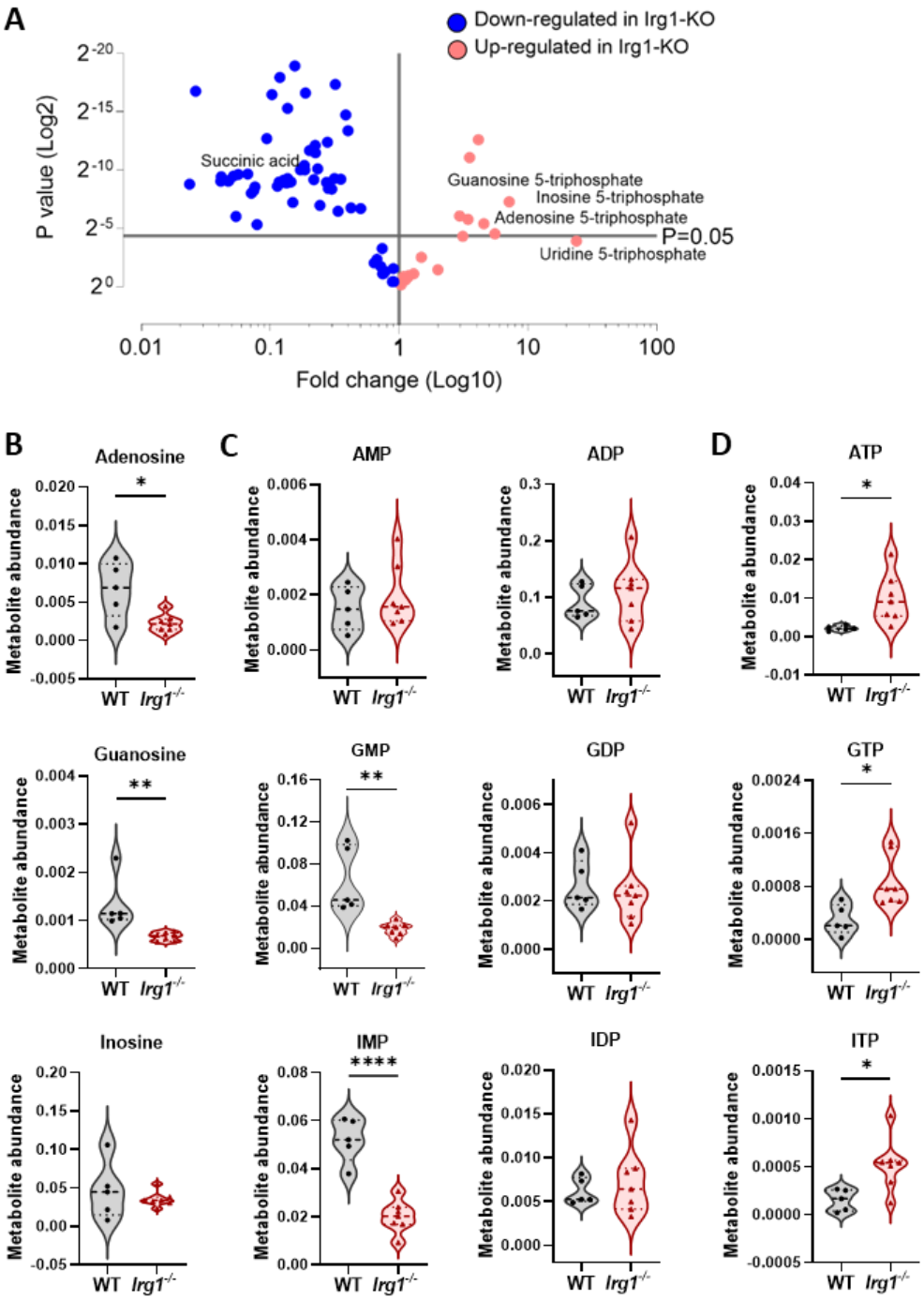

Figure 4.25: Altered purine metabolism in *Irg1*$^{-/-}$ LKs. A) Volcano plot comparing metabolite levels between WT-LK and *Irg1*$^{-/-}$ LK, highlighting the significantly altered metabolites (log10-fold change ≥1.20 or ≤0.80; p ≤ 0.05). B) Abundance of purine nucleosides: adenosine, guanosine and inosine. (C) Purine monophosphates (AMP, GMP, IMP) and diphosphates (ADP, GDP, IDP). (D) Purine triphosphates: ATP, GTP and ITP. n = 5 in WT LKs. n = 7 in *Irg1*$^{-/-}$ LKs. The error bars indicate the mean value with SEM. Data were analyzed with a two-way ANOVA and an unpaired Student's t-test. *p<0.05, **p<0.01, ****p<0.0001.

5. Discussion

In this thesis, I investigated the effects of the IRG1/Itaconate axis on the cardiopulmonary phenotype, focusing on its immunometabolic regulatory function. Both *in vitro* and *in vivo* results show that this axis plays a crucial protective role for the cardiovascular system through inter-organ communication actively mediated by the BM. Specifically, we show that IRG1/Itaconate modulates the differentiation and mobilization of HSPCs via immunometabolic mechanisms, which in turn shapes the composition of immune cells in the circulation and ultimately influences their infiltration into the lung and heart. These findings emphasize the importance of BM-derived cells, particularly those derived from HSC lineages, in the development and progression of cardiopulmonary diseases, including PH. In addition, itaconate could be a potential therapeutic target for cardiovascular complications. Our main findings are therefore as follows (Figure 5.1):

1) *Irg1*-deficient mice develop RV and LV hypertrophy and dysfunction at baseline. This phenotype was characterized by a distinct molecular signature involving enrichment of markers TNF-α_via_NF-κB signaling and hypoxia, and upregulation of key markers involved in the vascular and epigenetic machinery, such as Edn3 and Jmjd3 in the heart.

2) *Irg1*-deficient mice exhibited mild pulmonary vascular remodeling at baseline but developed exacerbated PH when exposed to chronic hypoxia compared to WT mice, demonstrating increased susceptibility to PH stimuli.

3) In the heart and lungs of *Irg1*-deficient mice, we observed remarkable changes in immune cell composition, particularly in the myeloid lineage. This shift in immune cell populations contributes to the observed cardiopulmonary dysfunction leading to an inflammatory signature in the heart.

4) Proinflammatory BMDMs from *Irg1*$^{-/-}$ mice induce cardiac remodeling markers in cardiomyocytes and notably increase *Myh7:Myh6* ratio via a paracrine effect, suggesting that Irg1/itaconate-deficient BMDMs play a vital role in promoting cardiac hypertrophy and dysfunction.

5) Adoptive transfer of BM from *Irg1*$^{-/-}$ mice into naive WT mice results in cardiac hypertrophy, emphasizing the strong contribution of BM to cardiac dysfunction in Irg1 deficient mice.

6) Irg1-deficient HSCs exhibit impaired multipotency characterized by a reduction in LT-HSCs and a pronounced shift towards MPP-Ly, disrupting immune cell dynamics. This dysfunction is associated with dysregulation of immunometabolism, as impaired purine metabolism in *Irg1*$^{-/-}$ HSCs activates the NLRP3 inflammasome, potentially affecting mobilization of HSCs and contributing to altered hematopoietic and immune responses.

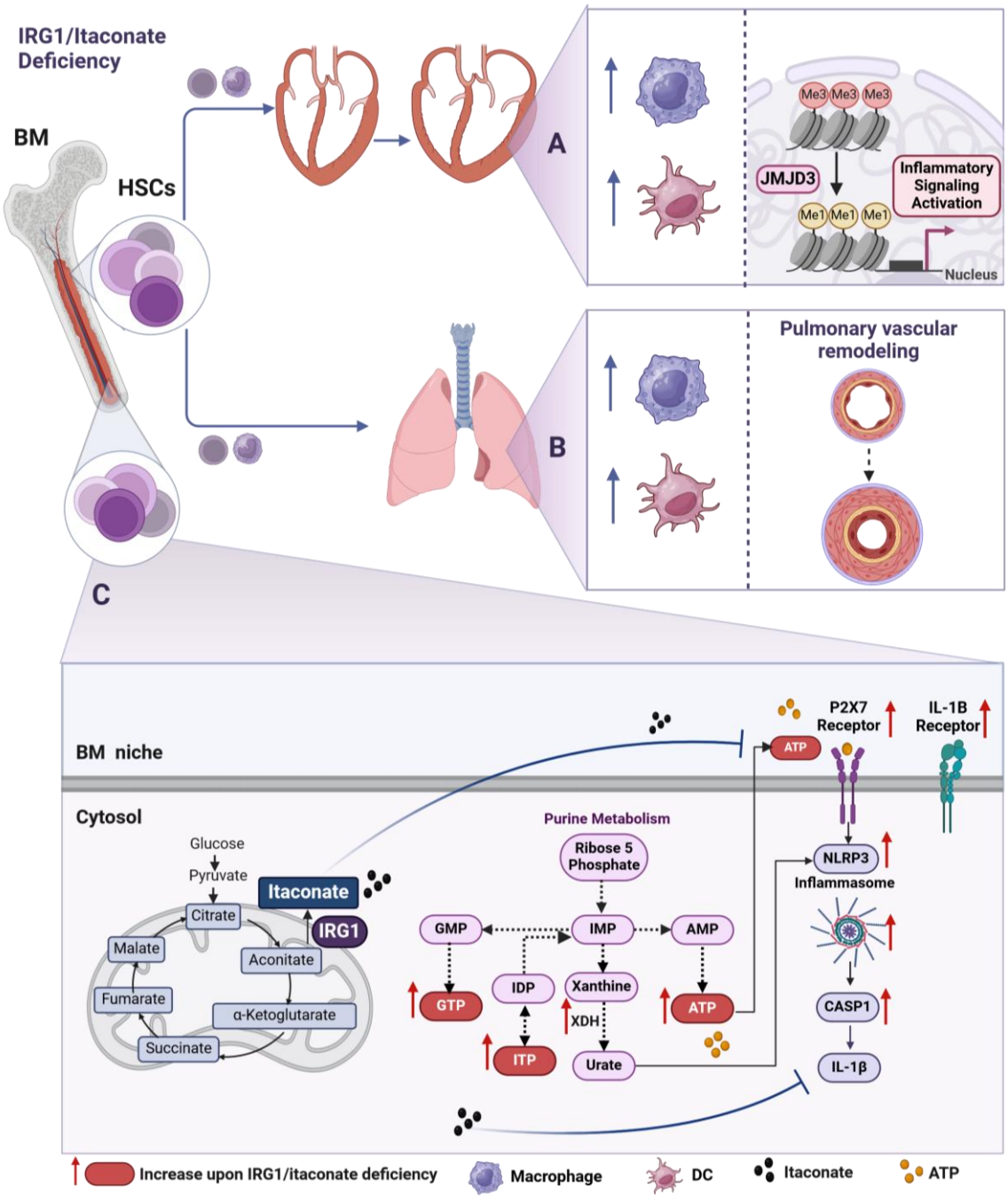

Figure 5.1: The schematic figure representing the findings of my thesis. A) IRG1/Itaconate deficiency exacerbates inflammation in the heart by increasing immune cell infiltration, particularly macrophages and DCs and promoting the activation of JMJD3-mediated inflammatory signaling pathways, contributing to cardiac hypertrophy and dysfunction. B) The IRG1/Itaconate deficiency leads to heightened immune cell infiltration and vascular remodeling in the lung. C) In HSCs, the IRG1/Itaconate axis modulates intracellular metabolic pathways, including purine metabolism, to regulate ATP levels and downstream inflammatory responses. Elevated extracellular ATP, resulting from IRG1/Itaconate deficiency, activates P2X7 receptors, promoting NLRP3 inflammasome assembly and caspase-1 (CASP1) activation, leading to the production of proinflammatory IL-1β. Created with BioRender.com.

5.1. IRG1/Itaconate axis displays a protective role in CVD.

Itaconate has been investigated in various *in vivo* and *ex vivo* models as a potential therapeutic target for CVD, with evidence of its role in improving cardiovascular structure and function through specific pathways (Figure 5.2). However, previous studies have primarily focused on the protective or therapeutic functions of IRG1 or itaconate in specific CVD such as MI and atherosclerosis (166). To date, no studies have investigated the underlying cardiovascular abnormalities resulting from *Irg1*/Itaconate deficiency. As part of my dissertation project, we investigated in detail the structural and functional parameters of cardiac hypertrophy and failure in *Irg1*$^{-/-}$ mice, and the observed RV remodeling in these mice drew our attention to possible changes in their pulmonary vasculature.

Duan et al. demonstrated that *Irg1*-deficient mice exhibited larger infarct size, increased myocardial fibrosis and impaired cardiac function following doxorubicin-induced myocardial injury. Mechanistically, *Irg1* deficiency led to increased production of proinflammatory cytokines due to inhibition of NRF2 and activation of transcription factor 3 (ATF3) in cardiac macrophages. Importantly, administration of 4OI *in vivo* as a rescue experiment successfully reduced cardiac inflammation and fibrosis, effectively preventing adverse ventricular remodeling in *Irg1*-deficient mice subjected to MI. These results indicate that *IRG1* plays a critical role in limiting inflammation and protecting against cardiac dysfunction in ischemic or toxic injury (167). With respect to cardiac fibrosis, our data are fully consistent with these observations and show that *Irg1*$^{-/-}$ hearts have significantly higher collagen deposition compared to WT hearts, which is associated with upregulation of Collagen III. Furthermore, the significant increase in the total number of immune cells, especially macrophages, in *Irg1*$^{-/-}$ hearts were corraborated by our *in vitro* experiments. Notably, *IRG1*-silenced human M1 macrophages significantly induced hyperproliferative and pro-fibrotic phenotypes in human CFs through the upregulation of fibrotic and ECM markers, including *Postn*, *Col1a2* and *Actc1*. These results indicate that IRG1 is a critical regulator of inflammatory and fibrotic responses in cardiac pathology. However, further studies are needed to uncover the IRG1/Itaconate-modulating molecular pathways that regulate ECM production by CFs.

Studies in atherosclerotic CVD have shown that IRG1 expression and itaconate production increase in myeloid cells of atherosclerotic plaques (168, 169). Chronic activation of innate immune system cells, including monocytes, macrophages and neutrophils, within the plaque creates a preserved inflammatory environment (170). Macrophages play a central role in atherosclerosis by recognizing and degrading oxidized low-density lipoprotein (LDL), which activates proinflammatory signaling pathways and the NLRP3 inflammasome, leading to the release of cytokines such as IL-1β (171). Neutrophils contribute to the plaques by releasing ROS, neutrophil extracellular traps (NETs) and proteases, which increase inflammation and

allow further infiltration of immune cells (172). Cyr et al. found that activation of the NLRP3 inflammasome in macrophages leads to increased IL-1β production, boosting inflammtion. In IRG1 deficiency, inadequate resolution of this inflammation promotes plaque progression, which can lead to heart attack or stroke (168). The IRG1/itaconate axis plays a protective role in atherogenesis by regulating inflammation through the activation of NRF2 signaling. *In vitro* studies have also shown that 4OI supplementation attenuates proinflammatory signaling pathways in human PBMCs treated with CVD patient plasma, reduces neutrophil degranulation and enhances antioxidant and anti-inflammatory signaling pathways in macrophages (169). Our results contribute to this understanding and demonstrate that NLRP3 inflammasome activation in IRG1-deficient HSC cells impair their differentiation and mobilization, leading to defective HSC function. These phenotypic changes in *IRG1*-deficient HSCs, as the origin of immune cells, may contribute to inflammatory cascades that promote atherogenesis.

During heart transplantation, acetylation of histones H3K9 and H3K27 decreases, impairing gene transcription in the donor heart. Lei et al. demonstrated that preservation of the heart in a solution containing the histone deacetylase inhibitor valproic acid (VPA) improved donor heart function by upregulating *IRG1* and increasing itaconate production. This was achieved by enhanced translocation of NRF2 to the nucleus, which reduced oxidative stress and increased the activity of antioxidant proteins. The study emphasizes that the cardio-protective effects of VPA are dependent on IRG1-driven itaconate production. In addition, treatment with exogenous 4OI improved cardiac function and reduced oxidative DNA damage (173). These results highlight the epigenetic regulatory role of the itaconate metabolite. In this context, my data also showed that JMJD3, a histone demethylase, may be upregulated in IRG1/Itaconate-deficient hearts. Further studies are needed to determine whether itaconate plays a primary regulatory role in this mechanism.

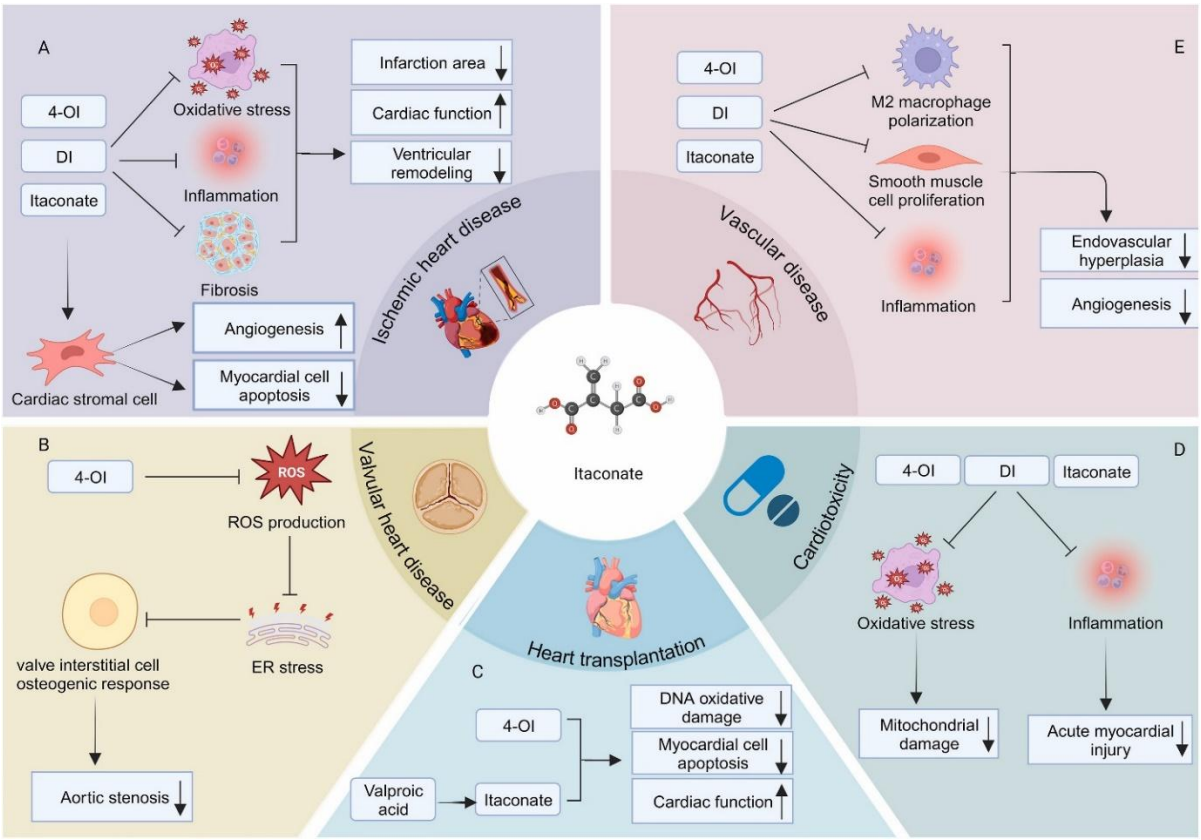

Figure. 5.2. Contribution of IRG1/Itaconate axis to CVD. A) Itaconate promotes myocardial repair following MI by enhancing cardiac stromal cell function, modulating inflammatory responses, mitigating oxidative stress, and reducing fibrosis. B) Itaconate prevents aortic valve calcification and stenosis in valvular heart disease via an anti-osteogenic effect through inhibiting the production of reactive oxygen species (ROS) and endoplasmic reticulum stress in valvular mesenchymal stromal cells. C) During heart transplantation, itaconate improves donor heart function and resilience to ischemic stress by activating the Nrf2 signaling pathway, dampening oxidative DNA damage and preserving cardiac performance. D) Itaconate protects against chemotherapy-induced cardiotoxicity by attenuating acute myocardial injury through the inhibition of inflammation and oxidative stress. Additionally, it shields mitochondria from oxidative damage, mitigating drug-related cardiac dysfunction. E) In vascular disease, itaconate regulates vascular remodeling by suppressing smooth muscle cell proliferation and endothelial inflammatory responses. Reused under Creative Common CC BY license from reference (166).

5.2. IRG1/Itaconate-deficiency drives cardiac hypertrophy and dysfunction through activation of inflammatory and endothelin-associated pathways.

My data show that upregulation of Jmjd3 in *Irg1*$^{-/-}$ hearts mediates demethylation of H3K27me3, leading to upregulation of TNFα via NFκB inflammatory signaling. JMJD3 is an important epigenetic regulator that functions as a histone demethylase and specifically targets the trimethylation of H3K27me3. This process plays a critical role in the activation of transcriptome regulation associated with development, differentiation and inflammation (174).

The activity of JMJD3 depends on α-KG as an essential cofactor, while succinate, a by-product of its enzymatic reaction, inhibits its function. Consequently, the intracellular balance between α-KG and succinate can directly affect chromatin structure and gene expression (75). In addition, itaconate contributes to succinate accumulation in M1 macrophages by inhibiting SDH activity (150). As a result, increased itaconate level, decreased α-KG and enhanced succinate concentrations can potentially impair JMJD3 activity (175). The electrophilic α, β-unsaturated carboxylic acid group of itaconate enables it to induce post-translational modifications on glycolytic enzymes by alkylating their cysteine residues, thereby inhibiting glycolysis and providing anti-inflammatory effects. In view of this, it is worth investigating whether JMJD3 is one of the potential targets for itaconate-mediated modifications, despite the potential of itaconate to indirectly contribute to the inhibition of JMJD3 activity (176).

A strong correlation was also found between JMJD3 and endothelin receptor type B (EDNRB) expression. JMJD3 deficiency in SMCs leads to a reduction in EDNRB expression, which triggers a compensatory upregulation of endothelin receptor type A (EDNRA). Since arterial SMCs are critical for the regulation of vascular tone, upregulation of EDNRA due to JMJD3 deficiency promotes a synthetic phenotype in SMCs, leading to hypertensive arterial remodeling (177).

In the same line, RNA-seq examination of LV and RV in *Irg1*$^{-/-}$ mice revealed significant upregulation of EDN3 in both ventricles. Endothelins (EDNs) are a family of three structurally similar peptides, EDN1, EDN2 and EDN3, which play a key role in the pathophysiology of HF (178). Increased EDN1 activity is associated with a variety of hypertrophy-associated CVD (179). In particular, plasma levels of EDN1 correlate positively with the severity of HF in patients with chronic HF, emphasizing its importance as a marker and factor for disease progression (180). Both EDN1 and EDN3 are potent activators of the EDNRB receptor, which mediates vasoconstriction and vasodilation and induces the release of nitric oxide and prostacyclin, ultimately contributing to vascular relaxation and homeostasis (181). *In vitro* studies show that EDN1 not only regulates the contractile function of SMCs and cardiomyocytes, but also promotes their growth phenotype and induces cellular hypertrophy (182). In addition, EDN3 selectively binds to EDNRB, where it can induce hypertrophy and stimulate EDN1 production. Importantly, this hypertrophic response can be attenuated by blocking the EDNRA receptor, suggesting that EDNRA antagonists can effectively prevent hypertrophic changes in cardiomyocytes (183). Our results are consistent with these findings and suggest that upregulation of Edn3 may contribute substantially to the cardiac hypertrophy phenotype in *Irg1*$^{-/-}$ mice. Previous research has shown that TNF-α can induce the expression and release of EDN1 through NF-κB activation (184), ndicating that the elevated EDN3 expression observed in *Irg1*$^{-/-}$ hearts might be linked to TNF-α_via_NF-κB signaling, potentially triggered by immune cell infiltration. In addition, itaconate-mediated epigenetic regulation may

represent another mechanism affecting EDN3 expression, warranting further investigation into its potential role in regulating endothelin expression and associated hypertrophic responses.

5.3. IRG1/Itaconate-deficiency drives pulmonary vascular remodeling and induce PH.

Itaconate and its derivatives have been shown to play significant roles in vascular diseases due to their anti-angiogenic, anti-inflammatory, and antioxidant properties. In vascular contexts, protective effects of itaconate have been demonstrated through its ability to attenuate inflammation, inhibit vascular cell proliferation, and modulate angiogenic processes. For example, increased itaconate expression in human and murine aortic aneurysms was shown to mitigate inflammation via NRF2 activation, reducing aneurysm formation (185). Similarly, the itaconate derivative dimethyl itaconate (DMI) inhibits endothelial cell angiogenesis by suppressing their growth, migration, and invasion in a dose-dependent manner. This effect is mediated through inhibition of IL-6, NLRP3, NF-κB, and IL-1β, alongside NRF2 activation and reduction of oxidative stress (186-188). These findings suggest that the anti-inflammatory and anti-proliferative properties of itaconate derivatives may have broader implications for vascular remodeling and disease prevention.

In the context of severe peripheral arterial disease (PAD), where M1 macrophages hinder arteriogenesis, microRNA-93 (miR93) has been found to favor angiogenesis by downregulating IRG1 and decreasing itaconate production, promoting M2-like polarization in ischemic muscle (152). Similarly, itaconate has demonstrated potential therapeutic effects in restenosis following stent implantation. Recent studies show that 4OI-releasing scaffolds inhibit smooth muscle cell proliferation and inflammation, improving vascular remodeling by modulating TGF-β/SMAD signaling (189). Together, these findings underscore the multifaceted role of itaconate in regulating vascular responses through its immunometabolic functions.

Our results align with these observations, particularly in PH, where we found that IRG1-deficient macrophages exhibit a proinflammatory phenotype characterized by increased IL-1β production, which drives a hyperproliferative response in PASMCs via paracrine mechanisms. Furthermore, *Irg1*$^{-/-}$ mice show significant pulmonary vascular remodeling and notable increment of percentage of muscularization in micro vessels. When exposed to hypoxia, these mice exhibit exacerbated PH phenotype compared to WT controls, indicating that the IRG1/Itaconate axis plays a crucial role in remodeling of pulmonary vessels.

Although itaconate may regulate several immunometabolic mechanisms that affect angiogenesis and vascular cell proliferation, the specific downstream pathways remain incompletely defined. In this context, unpublished findings from our group (Mansouri et al.) have identified a metabolic-based mechanism involving the reduction of the pentose

phosphate pathway, which explains the anti-proliferative function of itaconate and its derivatives on vascular cells. These findings provide a novel link between itaconate metabolism and its regulatory role in vascular remodeling, supporting our observations of its impact on pulmonary vascular cells.

Beyond PH, the IRG1/Itaconate axis has been implicated in other lung diseases, including pulmonary fibrosis and asthma. In idiopathic pulmonary fibrosis (IPF), reduced IRG1 expression and itaconate levels in alveolar macrophages were associated with a pro-fibrotic phenotype. Studies show that exogenous itaconate administration mitigates fibrosis by inhibiting lung fibroblast proliferation and wound healing (190). In support of these findings, our data show that IRG1 silenced macrophages promote the proliferation of CFs and induce a pro-fibrotic phenotype in these cells. Furthermore, IRG1-deficient M1 macrophages express higher levels of the proinflammatory cytokine IL-1β. This suggests that IRG1/Itaconate-deficient macrophages develop a unique phenotype that can trigger hyperproliferative responses in vascular cells through paracrine effects.

Beyond these, in allergic asthma, Irg1 deficiency exacerbates disease progression, characterized by increased Th2 cytokines and a proinflammatory macrophage phenotype (191). The role of itaconate extends to enhancing mucociliary clearance in respiratory epithelium. Itaconate binds to the 2-oxoglutarate receptor (OXGR1), activating pathways that improve mucus secretion and transport, thereby bolstering innate airway defense mechanisms (192). Impaired mucociliary clearance contributes to diseases such as asthma, COPD, and cystic fibrosis (193), further highlighting itaconate's therapeutic potential across a spectrum of lung diseases.

5.4. IRG1/Itaconate deficiency contributes to cardiopulmonary disease through dysregulation of HSC differentiation and myeloid progenitor expansion.

The primary cells responsible for the expression of *IRG1* are macrophages, which originate predominantly from the HSCs in the BM. These macrophages infiltrate the lung and their activity increases under pathological conditions. Our results suggest that Irg1-deficient mice exhibit impaired differentiation of HSCs, with an increased shift of HSCs towards the MPP^{Ly} and GMP populations. This shift can lead to proliferation of myeloid cells, particularly macrophages, in the lungs and heart, ultimately resulting in an inflammatory phenotype manifested by cardiac hypertrophy and pulmonary vascular remodeling.

In agreement with our results, there is evidence that myeloproliferative abnormalities are frequently found in the BM cells of PAH patients. This is also supported by the increased prevalence of PAH in patients with myeloproliferative disorders such as myeloid leukemia and primary myelofibrosis, suggesting a possible link between myeloid cells derived from the

hematopoietic lineage and the pathogenesis of PAH (194-196). Higher levels of circulating $CD133^+$ and $CD34^+$ cells were observed in PAH patients compared to healthy individuals, with these cells showing a greater tendency to differentiate into the myeloid lineage (197). Asosingh et al. demonstrated that transplantation of $CD133^+$ cells from PAH patients into nude mice resulted in increased pulmonary pressure, further indicating the role of myeloid progenitor cells in the development of PH (198).

Myeloproliferative neoplasms (MPN), which are characterized by chronic overproduction of mature myeloid cells, are also frequently associated with an increased incidence of PH and increased mortality (199, 200). In the WHO clinical classification, MPN-associated PH is categorized as Group V PH. The importance of hematopoietic progenitor cells in PAH is also emphasized by studies focusing on the *BMPR2* gene. 25% of patients with idiopathic PAH carry a mutation in BMPR2 (201). Heterozygous Bmpr2-null mice do not spontaneously develop PAH. Similarly, in heritable PAH in humans, patients with heterozygous *BMPR2* mutations have a lower penetrance (approximately 20–30%), suggesting that a second hit is required for disease manifestation. Of note, transplantation of *BMPR2*-mutated HSCs into irradiated mice followed by chronic low-dose LPS treatment resulted in the development of PAH in recipients, whereas mice receiving WT HSCs were protected (202). This emphasizes the role of *BMPR2*-mutated HSCs triggered by chronic inflammation in the pathogenesis of PH. Our data show conceptual similarities with this phenotype: IRG1-silenced, LPS-treated M1 macrophages can induce a growth response in pulmonary vascular cells. Moreover, transfer of *Irg1*$^{-/-}$ BM cells into naïve irradiated WT mice resulted in increased RV and LV mass and impaired cardiac function.

Further evidence for the involvement of HSCs in the pathogenesis of PH is the somatic JAK2 mutation (JAK2V617F), which has been described as the most frequently observed driver mutation in patients with myeloproliferative disorders, particularly MPN (203). This mutation is also one of the most common somatic mutations in clonal hematopoiesis. Small hematopoietic cell clones carrying the JAK2 V617F mutation can contribute to the development of PH, especially under conditions of chronic hypoxia. This process is associated with increased perivascular neutrophil infiltration in the lung mediated by upregulation of activin A receptor-like type 1 (Acvrl1), which encodes ALK1, a type I transmembrane serine/threonine kinase receptor expressed in $Ly6G^+$ cells (204). Interestingly, itaconate and 4OI have been shown to inhibit JAK1 activation by direct post-translational modification at different cysteine residues (153). Therefore, the modification of JAK signaling by itaconate and 4OI may be a potential mechanism by which the IRG1/itaconate axis regulates HSC function, including their differentiation and relocalization in the BM and other organs.

Regarding the contribution of BM-derived cells in CVD, Hoffmann et al. have shown that in a mouse model of ischemic HF, 28 days after MI, there was a significant increase in progenitor cells that were concentrated in the myeloid lineage, as evidenced by increased CD41 expression. Interestingly, the expression of *Irg1* in HSCs initially increased 7 days after MI but then decreased until day 28 (165). This dynamic pattern is consistent with our findings on the protective role of *Irg1* in BM. Our data show that the IRG1/Itaconate axis regulates HSC differentiation by inhibiting myeloid distortion in the BM niche, suggesting that this axis plays a critical protective role in preventing the proliferation of myeloid progenitor cells after MI.

Our findings can be applied to clonal hematopoiesis of indeterminate potential (CHIP), which represents a major age-related risk factor for several CVD, including coronary artery disease and chronic HF (205-207). CHIP is characterized by the clonal expansion of HSCs due to somatic mutations in genes such as *DNMT3A*, *TET2*, *ASXL1* and *JAK2* that occur during aging in the human population (208, 209). These mutations, particularly *DNMT3A* mutations, confer a selective advantage to certain HSCs leading to their immortalization, while loss of TET2 promotes greater myeloid bias in HSC differentiation (210). Interestingly, itaconate, a product of mitochondrial metabolism, has been shown to inhibit TET activity, thereby altering the DNA methylation profile in immune cells and affecting the immune response (151). This raises the intriguing possibility that IRG1/Itaconate, a key component of mitochondrial metabolism, may be dysregulated in HSCs with CHIP driver mutations (211). Itaconate has also been identified as a potent SDHA blocker, supporting our hypothesis that dysregulation of the IRG1/Itaconate axis in CHIP patients may impair the ability to effectively inhibit SDHA activity. Therefore, it is necessary to investigate the effects of age-related driver mutation on IRG1/Itaconate levels in the elderly human population with and without CHIP driver mutations.

Another aspect is that recent studies have elucidated the mechanisms by which CHIP mutations contribute to cardiac dysfunction. For example, mutations in *DNMT3A* and *TET2* are associated with a proinflammatory phenotype in monocytes and other immune cells. Abplanalp et al. showed that *DNMT3A*-mutated monocytes exhibit increased expression of genes involved in inflammation, cytokine production and phagocytosis (212). This increased inflammatory state promotes cardiac remodeling and fibrotic changes that exacerbate HF. We observed similar phenotypes in cardiac cells (nCMs and CFs) after treatment with the supernatant of *IRG1*-ablated BMDMs or PBMC-derived macrophages. Therefore, by attenuating the proinflammatory status in the macrophage population, IRG1 may function as a checkpoint inflammatory factor during MI.

The results of our research on IRG1/Itaconate deficiency provide valuable insights into the mechanisms by which proinflammatory immune cells contribute to cardiac hypertrophy and dysfunction. They also open up possibilities for novel therapeutic interventions targeting

immune cell metabolism to prevent or ameliorate HF associated with CHIP and other inflammatory diseases.

5.5. IRG1/Itaconate axis regulate the differentiation and expansion of HSCs.

Recent observations have challenged the traditional model of HSC lineage restriction, which previously suggested a clear separation into common myeloid and common lymphoid progenitor pathways (213). Instead, there is evidence that MPP^{Ly} retain the capacity for both granulocyte-monocyte (GM) and lymphoid differentiation at the earliest stages of lymphopoiesis, despite exhibiting reduced megakaryocyte-erythroid (MkE) transcription and lineage potential. Studies have shown that the earliest thymic progenitors commited to the lymphoid lineage also have combined T cell and GM differentiation capacities but lack MkE potential (214), supporting the idea that MPP^{Ly} retain GM potential. Consistent with these findings, our data show that despite the observed increase in the MPP^{Ly} population in the BM of *Irg1*$^{-/-}$ mice, there is a concomitant increase in myeloid lineage cells in the BM, heart and lungs of these mice. This suggests that the expanded MPP^{Ly} pool in *Irg1*$^{-/-}$ mice does not impede myeloid differentiation. Instead, this suggests a more complex regulatory mechanism that allows for the simultaneous expansion of both lymphoid-primed progenitor cells and myeloid lineage cells, possibly indicating compensatory or alternative pathways that drive myelopoiesis in Irg1-deficient mice compared to WT. The thrombopoietin receptor (MPL) is essential for the maintenance of HSCs and megakaryocyte differentiation. Downregulation of MPL in LKs, is associated with an increase in GM potential (215). Consistent with this, our RNA-seq data show that *Mpl* expression is significantly lower in Irg1-deficient LKs, which are the origin of MPP^{Ly}, than in WT LKs, indicating a shift in their functional properties consistent with this transition. Accordingly, the GM lymphoid restriction criterion is more pronounced in Irg1-deficient LKs, demonstrating their diminished ability to commit to the MkE fate.

In addition, recent reports indicate that infections trigger emergency granulopoiesis, which differs in transcription from steady-state granulopoiesis (216). This leads to rapid proliferation of myeloid progenitor cells and *de novo* granulocyte formation (217). Furthermore, elevated levels of IL-1 in the BM after infection direct HSCs to myeloid differentiation via the NF-κB signaling pathway and accelerate maturation into myeloid cells. While beneficial during acute inflammation, chronic IL-1 exposure impairs the ability of HSCs to differentiate into lymphoid and erythroid lineages and decreases the capacity for self-renewal, which is reversible upon IL-1 withdrawal (218).

The protein C receptor (PROCR /CD201) is a cell surface marker that helps to distinguish HSCs with different cell fate. $CD201^{-}$ cells show a tendency towards myeloid differentiation, especially during emergency granulopoiesis, when HSCs generally favor myeloid over

lymphoid production. In response to infection, $CD201^+$ and $CD201^-$ HSCs turn on different receptors and signaling pathways and use different isoforms of the transcription factor CCAAT Enhancer Binding Protein Beta (C/EBPβ), which regulates their lineage-specific differentiation (219). Our data is consistent with these findings and show that upregulation of IL-1β in $cKit^+$ cells from *Irg1*$^{-/-}$ BM contributes to HSC differentiation and increased GMP subpopulation. This leads to increased numbers of myeloid lineage cells in peripheral tissues such as the lung and heart. In addition, CD201 is significantly downregulated in *Irg1*$^{-/-}$ compared to WT LKs, suggesting that the absence of the IRG1/Itaconate axis shifts HSCs from a lymphoid to a myeloid population, leading to increased myeloid cell production.

5.6. IRG1/Itaconate axis deficiency leads to mobilization of HSCs through dysregulation of purine metabolism and activation of the NLRP3 inflammasome.

Activation of purinergic signaling in HSCs plays a crucial role in their mobilization from the BM into peripheral blood and tissues. Elevated extracellular ATP levels serve as a key trigger for this process by activating the NLRP3 inflammasome, leading to HSC mobilization (220). Sterile inflammation, which occurs without microbial infection and is triggered by endogenous signals such as extracellular nucleotides and ROS, contributes to HSC mobilization (221). In the BM microenvironment, the release of extracellular ATP and ROS acts as DAMPs that activate purinergic signaling and trigger sterile inflammation. ROS is released by granulocytes and monocytes residing in the BM, which further amplifies inflammatory signaling and promotes HSC egress (222, 223). Extracellular ATP triggers purinergic signaling by binding to P2 family receptors on HSCs, including P2X ion channel receptors such as P2RX7 (224). Activation of P2RX7 leads to downstream events that promote the assembly and activation of the NLRP3 inflammasome (225). The inflammasome triggers the cleavage of pro-caspase-1 into active caspase-1, which processes the proinflammatory cytokines IL-1β and IL-18 (226). These cytokines interfere with the interactions between HSCs and their niches in the BM, specifically affecting the SDF-1–CXCR4 and very late activation antigen-4 (VLA-4) and vascular cell adhesion molecule (VCAM-1) axes, which are important for HSC retention, leading to the release of HSCs into the circulation (227). In this context, my thesis data show that in IRG1-deficient HSCs there is a significant alteration in purine metabolism, as evidenced by increased production of nucleoside triphosphates such as ATP, GTP and UTP. Transcriptome profiling of HSC subpopulations confirmed significant upregulation of enzymes involved in the purine metabolic pathway, including xanthine dehydrogenase (XDH) and purine nucleoside phosphorylase 2 (PNP2). This upregulation at the transcriptomic level may represent a cellular mechanism to maintain nucleotide homeostasis through feedback control in purine metabolism.

Furthermore, the increased levels of macrophages and DCs observed in the heart and lung tissues of *Irg1*$^{-/-}$ mice suggest that deficiency in the IRG1/Itaconate axis affects the differentiation and homing patterns of HSCs. This is consistent with the concept that mobilized HSCs can migrate to extramedullary tissues where they proliferate and differentiate into cells of the myeloid lineage, thus contribute to local immune surveillance and innate immune responses (228).

Given the role of itaconate as an anti-inflammatory metabolite that can inhibit ROS production and NLRP3 inflammasome activation, it should be investigated whether the use of exogenous itaconate could inhibit the phenotypes of HSC mobilization associated with IRG1 deficiency. The interplay between purinergic signaling, NLRP3 inflammasome activation, ROS production and the complement system underscores a complex network that regulates HSC mobilization. Conversely, inhibition of CD73, an ectonucleotidase that degrades extracellular ATP to adenosine, enhances HSC mobilization by preventing adenosine-mediated negative feedback (226). Interfering with these pathways may provide novel strategies to control HSC mobilization, which would have significant clinical implications for hematopoietic transplantation and the treatment of hematological diseases.

Previous reports have shown that in PH, hypoxia-induced vascular remodeling is accompanied by the mobilization of BM-derived cKit^{+} progenitor cells. The migration of these BM-derived cKit^{+} cells into the peripheral circulation contributes to an environment in the pulmonary artery vessel wall that facilitates adhesion of circulating cells and promotes vascular remodeling (229). *In vivo* studies have shown that administration of AMD3100 (a CXCR4 antagonist) and CCX771 (a CXCR7 antagonist) to mice exposed to chronic hypoxia prevented vascular remodeling, RV hypertrophy, and ultimately the development of PH by inhibiting the accumulation of perivascular LKS progenitor cells (230). Interestingly, sildenafil, a phosphodiesterase-5 (PDE-5) inhibitor used therapeutically in PH, has been shown to improve the PH phenotype *in vivo* by inhibiting the recruitment of BM-derived cKit^{+} cells and CD68^{+} macrophages together with CXCR4^{+} cells into the lung tissue (231). Similar to these observations, our data suggest that modulation of the IRG1/Itaconate axis may have a protective role against vascular remodeling and PH progression by preventing the egress of BM-derived progenitor cells, ultimately reducing their contribution to pathological vascular remodeling in PH. Exogenous itaconate could potentially reduce extracellular ATP levels and subsequent inflammasome activation as well as modulate ROS production. This therapeutic approach requires further investigation to evaluate its efficacy in modulating HSC trafficking and attenuating inflammatory responses in PH and hematopoietic disorders.

In summary, our results highlight the critical role of elevated extracellular ATP levels in the activation of purinergic signaling pathways and the NLRP3 inflammasome in HSCs, particularly

when the IRG1/Itaconate axis is defective. Understanding this mechanism provides valuable insights into the regulation of HSC trafficking and suggests potential therapeutic interventions targeting metabolic and signaling pathways to modulate immune responses in PH and hematopoietic disorders.

6. Outlook

Since Irg1/Itaconate-deficient mice spontaneously develop RV and LV hypertrophy, the following experiments may provide further insight into clinical, mechanistic and therapeutic constellations.

Clinical studies: Screening HF patients for IRG1-associated SNPs or mutations could provide valuable clinical insights. Similar clinical investigations could be extended to PH patients, especially those with pulmonary arterial hypertension (PAH, group 1) and left heart-associated PH (group 2), as *in vivo* studies have clearly demonstrated the critical role of the Irg1/itaconate axis in both the development and progression of PH.

IRG1 regulation or Itaconate levels might be impaired in PH or HF patients. Therefore, measurement of IRG1 expression and itaconate levels or its biological derivatives in blood cells or plasma samples from patients would help to elucidate potential clinical correlations between IRG1/Itaconate levels and cardiopulmonary pathology. In addition, lung, heart and ideally BM samples from cardiopulmonary patients would be invaluable for exploring any clinical correlations between *IRG1* expression or itaconate levels and disease severity.

Given the hematopoietic abnormalities observed in *Irg1*-deficient mice that contribute to cardiac dysfunction and PH, investigating IRG1 expression or Itaconate production in patients with CHIP-associated HF or PH may provide further insight into the contribution of hematopoietic abnormalities to cardiopulmonary disease.

Therefore, I believe that investigating the presence of *IRG1* SNPs or mutations and measuring itaconate levels in patients with CVD and individuals with hematopoietic disorders could help identify new genetic susceptibilities.

Mechanistic studies: CITE-seq (Cellular Indexing of Transcriptomes and Epitopes by Sequencing) is a valuable approach to complement single-cell RNA sequencing (scRNA-seq) for the investigation of HSC lineage decisions and the identification of precise HSC subtypes and states. Application of CITE-seq specifically to *Irg1*-deficient HSCs would provide more detailed insights into the altered lineage dynamics and functional states caused by Irg1 deficiency. By combining transcriptome and epitope profiling of individual cells, CITE-seq can improve the depth and precision of our understanding of lineage bias and functional states. This technology is particularly useful for distinguishing between lymphoid and myeloid HSCs and provides insights into clonal diversity.

Further investigation of the proposed mechanism in Irg1-deficient HSCs should include measurement of extracellular ATP levels in the BM niche of *Irg1*$^{-/-}$ mice. In addition, evaluation of the population of cKIT^{+} cells in the peripheral blood, lung and heart of *Irg1*$^{-/-}$ mice could help

validate our proposed mechanism involving increased cell egress and organ crosstalk mediated by the IRG1/Itaconate axis.

In vitro and *in vivo* studies should also investigate whether exogenous itaconate administration can attenuate HSC mobilization phenotypes by restoring the IRG1/Itaconate axis. In addition, investigation of post-translational modifications of JMJD3 and the rate-limiting enzymes of purine metabolism (PNP2, NME1 and IMDPH) could provide deeper insights into the regulatory mechanisms.

Therapeutic approaches: To obtain a longitudinal assessment of PH and cardiac remodeling, a longer follow-up of *Irg1*$^{-/-}$ mice and *Irg1*$^{-/-}$ BM recipients exposed to hypoxia could provide a more comprehensive insight into the progression of pulmonary vascular remodeling and cardiac hypertrophy. This would also help to determine whether interventions with itaconate or its derivatives could prevent disease progression.

To further explore the role of JMJD3-mediated epigenetic modifications, studies using specific JMJD3 inhibitors could investigate whether pharmacologic modulation of JMJD3 is able to reverse or attenuate the inflammatory phenotype and cardiac hypertrophy in *Irg1*-deficient mice. This approach could help validate JMJD3 as a potential target for therapeutic intervention.

Elucidating how *IRG1* deficiency contributes to pulmonary vascular remodeling, fibrosis and immunomodulation could pave the way for targeted therapies. Modulation of this signaling pathway could lead to effective treatments for PH and other debilitating pulmonary diseases and underscore the therapeutic potential of targeting the IRG1/Itaconate axis.

Taken together, these prospects will broaden the understanding of how metabolic mediators such as itaconate affect inter-organ communication at the cellular and molecular level and offer promising avenues for therapeutic exploration.

7. Summary

The results of this work present the IRG1/Itaconate axis as a key mediator of inter-organ communication, particularly between BM, heart, and lung. We investigated the effects of IRG1/Itaconate deficiency on the cardiopulmonary phenotype through BM dynamics and showed that the absence of *IRG1* has profound effects on multiple organ systems, primarily through immune and metabolic dysfunction in HSCs, subsequently altering their differentiation and fate within the BM.

Our results showed that IRG1 deficiency leads to significant RV and LV hypertrophy and dilatation, accompanied by increased collagen deposition leading to cardiac dysfunction. These changes were associated with increased macrophage and DC composition. Transcriptome profiling of the *Irg1*$^{-/-}$ heart revealed dysregulated inflammatory pathways, particularly TNF-α signaling via NF-κB, hypoxia-associated pathways, and upregulation of Edn3. Furthermore, the histone demethylase Jmjd3 was upregulated in the hearts of Irg1-deficient mice, which was accompanied by a corresponding reduction in H3K27me3 levels. This suggests an epigenetic mechanism that exacerbates inflammation and promotes cardiac hypertrophy in the absence of IRG1. Overall, our data suggests that IRG1/Itaconate affects not only immune and metabolic pathways, but also epigenetic regulation that promotes inflammation.

In *Irg1*-deficient mice, we observed a predisposition to pulmonary vascular remodeling and increased susceptibility to hypoxia-induced PH, suggesting that IRG1 deficiency impairs both basic pulmonary homeostasis and exacerbates disease under external stress. This pathology is associated with abnormal immune cell dynamics and an increased inflammatory milieu in the lung driven by an increased myeloid cell population. These findings are consistent with our observations in group 1 PH patients, who had a similarly increased myeloid cell population compared to non-PH controls.

To better understand the role of BM cells in the cardiac phenotype of *Irg1*$^{-/-}$ mice, we performed adoptive transfer experiments. Transfer of BM cells from *Irg1*$^{-/-}$ mice into WT recipients replicated the hypertrophic cardiac phenotype, suggesting that BM-derived cells are central mediators of this pathological crosstalk.

IRG1/Itaconate-deficient proinflammatory BMDMs or PBMC-derived macrophages were shown to induce tissue remodeling in cardiac cells through paracrine signaling. This process upregulated markers of HF (*Mhc7:Mhc6* and *Nppb*) in nCM and pro-fibrotic markers (*Postn, Actc1* and *Col1a2*) in CF. These findings emphasize the key role of macrophages in the development of cardiac pathology associated with IRG1 deficiency, contributing to inflammation, hypertrophy and fibrosis.

Our study also investigated the effects of the IRG1/Itaconate axis on HSC differentiation and revealed significant perturbations characterized by a biased differentiation towards myeloid progenitors at the expense of lymphoid progenitors in *Irg1*$^{-/-}$ mice. Impaired purine metabolism in *Irg1*-deficient HSCs led to increased ATP levels, which activated the NLRP3 inflammasome and triggered an inflammatory cascade that promoted mobilization of HSCs and infiltration of immune cells into peripheral organs, particularly the heart and lungs. The combined effect of impaired HSC differentiation enhanced purinergic signaling and inflammasome activation links BM dysfunction to cardiopulmonary pathology.

In summary, our work reveals a paradigm in which the IRG1/Itaconate axis acts as a central regulator of immune-metabolic balance and controls inter-organ communication between the BM, lung and heart. The ability of this axis to modulate HSC differentiation, immune cell mobilization and inflammation underscores its essential role in maintaining systemic homeostasis. These findings suggest that therapeutically targeting the IRG1/Itaconate axis may be an effective strategy for the treatment of cardiopulmonary diseases caused by dysregulated immune responses and chronic inflammation. In addition, itaconate is a promising metabolite that can regulate the normal fate and propagation of HSCs.

8. Zusammenfassung

Die vorliegende Arbeit zeigt, dass die IRG1/Itaconate-Achse eine zentrale Rolle bei der Interorgankommunikation einnimmt, insbesondere zwischen Knochenmark, Herz und Lunge. Es konnte ein Zusammenhang zwischen einem Mangel an IRG1 und den daraus resultierenden Auswirkungen auf den kardiopulmonären Phänotyp aufgezeigt werden. Die Auswirkungen von IRG1/Itaconat-Mangel auf den kardiopulmonären Phänotyp über die Dynamik des Knochenmarks wurde untersucht und es konnte gezeigt werden, dass ein Mangel an *IRG1* tiefgreifende Auswirkungen auf mehrere Organsysteme hat. Dies ist primär auf immunologische und metabolische Dysfunktionen in HSCs zurückzuführen, die ihrerseits eine Veränderung ihrer Differenzierung und Determination innerhalb des Knochenmarks zur Folge hat.

Die Ergebnisse legen nahe, dass ein IRG1-Mangel zu einer signifikanten RV- und LV-Hypertrophie und –dilatation führt, begleitet von einer verstärkten Kollagenablagerung, die wiederum in einer kardialen Dysfunktion resultiert. Diese Veränderungen wurden von einem Makrophagenanstieg sowie DC Komposition begleitet. Transkriptom-Profiling von *Irg1*$^{-/-}$ Herzen zeigte dysregulierte Entzündungswege, darunter der Signaltransduktion von TNF-α über NF-κB, hypoxieassoziierte Signalwege sowie eine Hochregulierung von Edn3. Zudem konnte eine Hochregulierung der Histon-Demethylase Jmjd3 in den Herzen von Irg1-defizitären Mäusen beobachtet werden, welche mit einer entsprechenden Verringerung von H3K27me3 einherging. Dies lässt auf einen epigenetischen Mechanismus schließen, durch den in Abwesenheit von IRG1 die Entzündung verschlimmert und die kardiale Hypertrophie gefördert wird. Insgesamt weisen die Daten daraufhin, dass IRG1/Taconat nicht nur Immun- und Stoffwechselwege, sondern auch entzündungsfördernde epigenetische Regulationsmechanismen beeinflusst.

Bei *Irg1*-defizitären Mäusen konnte eine Prädisposition zu pulmonalem vaskulären Remodeling und eine erhöhte Anfälligkeit zu hypoxieinduzierter PH festgestellt werden, was darauf hindeutet, dass ein IRG1-Mangel sowohl die grundlegende pulmonale Homöostase beeinträchtigt als auch die Krankheit unter externem Stress verschlimmert. Dieser Zustand geht mit einer abnormalen Immunzelldynamik und einem erhöhten Entzündungsmilieu in der Lunge einher, das durch eine erhöhte myeloische Zellpopulation angetrieben wird. Diese Ergebnisse stimmen mit den Beobachtungen bei PH-Patienten der Gruppe I überein, welche im Vergleich zu Patienten ohne PH eine ähnlich erhöhte Anzahl myeloischer Zellen aufwiesen.

Um die Rolle von Knochenmarkszellen des kardialen Phänotyps von *Irg1*$^{-/-}$ Mäusen zu untersuchen, wurden adoptive Transfermethoden eingesetzt. Der Transfer von Knochenmarkszellen aus *Irg1*$^{-/-}$ Mäusen in Wildtyp-Rezipienten führte zu einer Replikation des

hypertrophen kardialen Phänotyps. Dies lässt den Schluss zu, dass Knochenmarkszellen eine zentrale Rolle als Mediatoren des pathologischen Cross-Talks einnehmen.

Es konnte nachgewiesen werden, dass IRG1/Itaconat-defizitäre, proinflammatorische BMDMs oder aus PBMC stammende Makrophagen durch parakrine Signalübertragungen einen Gewebeumbau in Herzzellen induzieren. Der Prozess resultierte in einer Hochregulierung von Markern für Herzversagen (*Mhc7:Mhc6* und *Nppb*) in nCM sowie pro-fibrotischen Markern (*Postn, Actc1* and *Col1a2*) in CF. Diese Ergebnisse unterstreichen die wichtige Rolle der Makrophagen bei der Entwicklung der mit IGR1-Defizit assoziierten Herzpathologie, die zu Entzündungen, Hypertrophie und Fibrose führt.

Die vorliegende Arbeit untersuchte zudem die Auswirkungen der IRG1/Itaconat-Achse auf die HSC-Differenzierung. Dabei konnten signifikante Störungen beobachtet werden, die durch eine einseitige Differenzierung in Richtung myeloischer Vorläuferzellen in *Irg1*$^{-/-}$ Mäusen gekennzeichnet ist. Der beeinträchtige Purinstoffwechsel in *Irg1*-defizitären HSCs führte zu erhöhten ATP-Spiegeln, die das NLRP3-Inflammasom aktivierten und eine Entzündungskaskade auslösten, die die Mobilisierung von HSCs und die Infiltration von Immunzellen in periphere Organe, insbesondere Herz und Lunge, förderte. Die kombinierte Wirkung von gestörter HSC-Differenzierung, verstärkter puringergen Signalübetragung und Inflammasom-Aktivierung verbindet die Knochenmarksdysfunktion mit kardiopulmunärer Pathologie.

Zusammenfassend kann festgestellt werden, dass das hier gezeigte Paradigma die IRG1/Itaconat-Achse als zentralen Regulator des immun-metabolischen Gleichgewichts aufzeigt und die Interorgankommunikation zwischen Knochenmark, Lunge und Herz kontrolliert. Die Fähigkeit dieser Achse, die HSC-Differenzierung, Immunzellmobilisierung sowie Entzündungen zu modulieren, unterstreicht ihre wesentliche Rolle bei der Aufrechterhaltung der systemischen Homöostase. Die vorliegenden Ergebnisse legen den Schluss nahe, dass ein therapeutischer Eingriff in die IRG1/Itaconat-Achse eine vielversprechende Strategie zur Behandlung von Herz-Lungen-Erkrankungen, die durch dysregulierte Immunreaktionen und chronische Entzündungen verursacht werden, darstellen könnte. Darüber hinaus weist sich Itaconat als vielversprechender Metabolit zur Regulation von Zelldetermination und Propagation von HSCs aus.

9. List of abbreviations

ACLY - ATP citrate lyase
Acvrl1 - Activin A receptor-like type 1
ALK1 - Type I transmembrane serine/threonine kinase receptor
AM - Alveolar macrophages
AMs - Alveolar macrophages
Ang-II - Angiotensin-II
ATF3 - Activation transcription factor 3
ATP - Adenosine triphosphate
BMDMs - Bone marrow-derived macrophages
BM - Bone marrow
BMP - Bone morphogenetic proteins
BMPR2 - Bone morphogenetic protein receptor type 2
cAMP - Cyclic adenosine monophosphate
CaMKIIδ - Calcium/calmodulin-dependent protein kinase II delta
CCR2 - C-C chemokine receptor 2
CCR5 - C-C chemokine receptor type 5
CD201 - Protein C receptor
CD206 - Mannose receptor
CD34 - Cluster of differentiation 34
CF - Cardiac fibroblasts
CHIP - Clonal hematopoiesis of indeterminate potential
cDNA - Complementary DNA
cKit - KIT proto-oncogene, receptor tyrosine kinase
CO - Cardiac output
Col III - Collagen III
COPD - Chronic obstructive pulmonary disease
CRTAC1 - Cartilage acidic protein 1
CSA - Cross-sectional area
CX3CL1 - C-X3-C motif chemokine ligand 1
CXCL12 - C-X-C motif chemokine 12
DCs - Dendritic cells
DNMT3A - DNA methyltransferase 3 alpha
DMI - Dimethyl itaconate
EC - Endothelial cells
ECM - Extracellular matrix
EDN1 - Endothelin 1
EDN3 - Endothelin 3
EDNRA - Endothelin receptor type A
EDNRB - Endothelin receptor type B

FACS - Fluorescence-activated cell sorting
FCS - Fetal calf serum
GAPDH - Glyceraldehyde-3-phosphate dehydrogenase
GM-CSF - Granulocyte-macrophage colony-stimulating factor
GM - Granulocyte-monocyte
GMP - Granulocyte-monocyte progenitors
GMP - Guanosine monophosphate
GSEA - Gene set enrichment analysis
HF - Heart failure
HIF - Hypoxia-inducible factor
HIF PHD - Hypoxia-inducible factor prolyl hydroxylase
HLA - Human leukocyte antigen
HPRT1 - Hypoxanthine phosphoribosyltransferase 1
HR - Heart rate
HSC - Hematopoietic stem cell
HSPC - Hematopoietic stem and progenitor cell
IB4 - Isolectin B4
IFNγ - Interferon gamma
IL-1β - Interleukin 1 beta
IL-2 - Interleukin 2
IL-4 - Interleukin 4
IL-6 - Interleukin 6
IL-8 - Interleukin 8
IL-10 - Interleukin 10
IM - Interstitial macrophages
IPF - Idiopathic pulmonary fibrosis
IRF3 - Interferon regulatory factor 3
IRF9 - Interferon regulatory factor 9
IRG1 - Immune-responsive gene 1
ITP - Inosine triphosphate
JAK1 - Janus kinase 1
JMJD3 - Jumonji domain-containing protein 3
LDL - Low-density lipoprotein
LPS - Lipopolysaccharide
LT-HSC - Long-term hematopoietic stem cells
LV - Left ventricular
LVSP - Left ventricular systolic pressure
LVEF - Left ventricular ejection fraction
LVWT - Left ventricular wall thickness
MacLow - Macrophage-low

MCPs - Monocyte chemoattractant proteins
MCT - Monocrotaline
MI - Myocardial infarction
MIF - Macrophage migration inhibitory factor
MMP - Metalloproteinase
MPL - Thrombopoietin receptor
MPP - Multipotent progenitor cells
MPPGM - Granulocyte-monocyte-primed MPPs
MPPLy - Lymphoid-primed multipotent progenitors
MPPMkE - Megakaryocyte-erythrocyte-primed multipotent progenitors
mPAP - Mean pulmonary artery pressure
mRNA - Messenger RNA
mTORC1 - mTOR complex 1
MSCs - Mesenchymal stromal cells
MYD88 - Myeloid differentiation primary response 88
Myh6 - Myosin heavy chain 6
Myh7 - Myosin heavy chain 7
NAD^+ - Nicotinamide adenine dinucleotide
NETs - Neutrophil extracellular traps
NF-κB - Nuclear factor kappa B
NID1 - Nidogen 1
NLRP3 - NLR Family Pyrin Domain Containing 3
NRF2 - Nuclear factor erythroid 2-related factor 2
NT-pro BNP - N-terminal pro b-type natriuretic peptide
Nppa - Natriuretic peptide A
Nppb - Natriuretic peptide B
OXGR1 - 2-oxoglutarate receptor
OXPHOS - Oxidative phosphorylation
PAECs - Pulmonary artery endothelial cells
PAAFs - Pulmonary artery adventitial fibroblasts
PAH - Pulmonary arterial hypertension
PASMCs - Pulmonary artery smooth muscle cells
PAMPs - Pathogen-associated molecular patterns
PBMCs - Peripheral blood mononuclear cells
PCA - Principal component analysis
PDE-5 - Phosphodiesterase-5
PDGF - Platelet-derived growth factor
PFA - Paraformaldehyde
pDCs - Plasmacytoid dendritic cells
PNP2 - Purine nucleoside phosphorylase 2

POSTN - Periostin
PPARγ - Peroxisome proliferator-activated receptor gamma
PRRs - Pattern recognition receptors
PROCR - Protein C receptor
PU.1 - Spi-1 proto-oncogene
qPCR - Quantitative polymerase chain reaction
RCM - Resident cardiac macrophage
ROS - Reactive oxygen species
RVID - Right ventricular internal diameter
RV - Right ventricular
RVSP - Right ventricular systolic pressure
RVWT - Right ventricular wall thickness
SCF - Stem cell factor
SDHA - Succinate dehydrogenase
SEM - Standard error of the mean
SiglecH - Sialic acid-binding immunoglobulin-like lectin H
siControl - Control small interfering RNA
siIRG1 - IRG1-targeted small interfering RNA
SLAM - Signaling lymphocyte activation molecule
SMCs - Smooth muscle cells
STAT1 - Signal transducer and activator of transcription 1
ST-HSC - Short-term hematopoietic stem cell
SV - Stroke volume
TAPSE - Tricuspid annular plane systolic excursion
TCA - Tricarboxylic acid
TET - Ten-eleven translocation
TFs - Transcription factors
TGF-β - Transforming growth factor-beta
Th1 - T-helper 1 cells
Th2 - T-helper 2 cells
TNF-α - Tumor necrosis factor-alpha
vWF - von Willebrand factor
VLA-4 - Very late activation antigen-4
VCAM-1 - Vascular cell adhesion molecule 1
VPA - Valproic acid
WT - Wild-type
WGA - Wheat germ agglutinin
XDH - Xanthine dehydrogenase
ZEB2 - Zinc finger E-box binding homeobox 2

10. List of figures

11. List of tables

12. References

1. Galie N, McLaughlin VV, Rubin LJ, Simonneau G. An overview of the 6th World Symposium on Pulmonary Hypertension. Eur Respir J. 2019;53(1).
2. Voelkel NF, Tuder RM. Cellular and molecular biology of vascular smooth muscle cells in pulmonary hypertension. Pulm Pharmacol Ther. 1997;10(5-6):231-41.
3. International PPHC, Lane KB, Machado RD, Pauciulo MW, Thomson JR, Phillips JA, 3rd, et al. Heterozygous germline mutations in BMPR2, encoding a TGF-beta receptor, cause familial primary pulmonary hypertension. Nat Genet. 2000;26(1):81-4.
4. Chelladurai P, Seeger W, Pullamsetti SS. Epigenetic mechanisms in pulmonary arterial hypertension: the need for global perspectives. Eur Respir Rev. 2016;25(140):135-40.
5. Ryanto GRT, Suraya R, Nagano T. Mitochondrial Dysfunction in Pulmonary Hypertension. Antioxidants (Basel). 2023;12(2).
6. Chan SY, Rubin LJ. Metabolic dysfunction in pulmonary hypertension: from basic science to clinical practice. Eur Respir Rev. 2017;26(146).
7. Simonneau G, Hoeper MM. The revised definition of pulmonary hypertension: exploring the impact on patient management. Eur Heart J Suppl. 2019;21(Suppl K):K4-K8.
8. Montani D, Gunther S, Dorfmuller P, Perros F, Girerd B, Garcia G, et al. Pulmonary arterial hypertension. Orphanet J Rare Dis. 2013;8:97.
9. Oudiz RJ. Pulmonary hypertension associated with left-sided heart disease. Clin Chest Med. 2007;28(1):233-41, x.
10. Alamri AK, Ma CL, Ryan JJ. Novel Drugs for the Treatment of Pulmonary Arterial Hypertension: Where Are We Going? Drugs. 2023;83(7):577-85.
11. Rako ZA, Kremer N, Yogeswaran A, Richter MJ, Tello K. Adaptive versus maladaptive right ventricular remodelling. ESC Heart Fail. 2023;10(2):762-75.
12. Egemnazarov B, Crnkovic S, Nagy BM, Olschewski H, Kwapiszewska G. Right ventricular fibrosis and dysfunction: Actual concepts and common misconceptions. Matrix Biol. 2018;68-69:507-21.
13. Sydykov A, Mamazhakypov A, Petrovic A, Kosanovic D, Sarybaev AS, Weissmann N, et al. Inflammatory Mediators Drive Adverse Right Ventricular Remodeling and Dysfunction and Serve as Potential Biomarkers. Front Physiol. 2018;9:609.
14. Frump AL, Bonnet S, de Jesus Perez VA, Lahm T. Emerging role of angiogenesis in adaptive and maladaptive right ventricular remodeling in pulmonary hypertension. Am J Physiol Lung Cell Mol Physiol. 2018;314(3):L443-L60.
15. Ryan JJ, Archer SL. Emerging concepts in the molecular basis of pulmonary arterial hypertension: part I: metabolic plasticity and mitochondrial dynamics in the pulmonary circulation and right ventricle in pulmonary arterial hypertension. Circulation. 2015;131(19):1691-702.
16. Piao L, Marsboom G, Archer SL. Mitochondrial metabolic adaptation in right ventricular hypertrophy and failure. J Mol Med (Berl). 2010;88(10):1011-20.
17. Khassafi F, Chelladurai P, Valasarajan C, Nayakanti SR, Martineau S, Sommer N, et al. Transcriptional profiling unveils molecular subgroups of adaptive and maladaptive right ventricular remodeling in pulmonary hypertension. Nat Cardiovasc Res. 2023;2(10):917-36.
18. Park JF, Clark VR, Banerjee S, Hong J, Razee A, Williams T, et al. Transcriptomic Analysis of Right Ventricular Remodeling in Two Rat Models of Pulmonary Hypertension: Identification and Validation of Epithelial-to-Mesenchymal Transition in Human Right Ventricular Failure. Circ Heart Fail. 2021;14(2):e007058.
19. Hindmarch CCT, Tian L, Xiong PY, Potus F, Bentley RET, Al-Qazazi R, et al. An integrated proteomic and transcriptomic signature of the failing right ventricle in monocrotaline induced pulmonary arterial hypertension in male rats. Front Physiol. 2022;13:966454.

20. Amini M, Zayeri F, Salehi M. Trend analysis of cardiovascular disease mortality, incidence, and mortality-to-incidence ratio: results from global burden of disease study 2017. BMC Public Health. 2021;21(1):401.
21. Roth GA, Mensah GA, Johnson CO, Addolorato G, Ammirati E, Baddour LM, et al. Global Burden of Cardiovascular Diseases and Risk Factors, 1990-2019: Update From the GBD 2019 Study. J Am Coll Cardiol. 2020;76(25):2982-3021.
22. Hautefort A, Girerd B, Montani D, Cohen-Kaminsky S, Price L, Lambrecht BN, et al. T-helper 17 cell polarization in pulmonary arterial hypertension. Chest. 2015;147(6):1610-20.
23. Thygesen K, Alpert JS, Jaffe AS, Chaitman BR, Bax JJ, Morrow DA, et al. Fourth Universal Definition of Myocardial Infarction (2018). J Am Coll Cardiol. 2018;72(18):2231-64.
24. Lodrini AM, Goumans MJ. Cardiomyocytes Cellular Phenotypes After Myocardial Infarction. Front Cardiovasc Med. 2021;8:750510.
25. Sutton MG, Sharpe N. Left ventricular remodeling after myocardial infarction: pathophysiology and therapy. Circulation. 2000;101(25):2981-8.
26. Erlebacher JA, Weiss JL, Weisfeldt ML, Bulkley BH. Early dilation of the infarcted segment in acute transmural myocardial infarction: role of infarct expansion in acute left ventricular enlargement. J Am Coll Cardiol. 1984;4(2):201-8.
27. Frangogiannis NG. Pathophysiology of Myocardial Infarction. Compr Physiol. 2015;5(4):1841-75.
28. Gabriel-Costa D. The pathophysiology of myocardial infarction-induced heart failure. Pathophysiology. 2018;25(4):277-84.
29. Pfeffer MA, Braunwald E. Ventricular remodeling after myocardial infarction. Experimental observations and clinical implications. Circulation. 1990;81(4):1161-72.
30. Desmouliere A, Geinoz A, Gabbiani F, Gabbiani G. Transforming growth factor-beta 1 induces alpha-smooth muscle actin expression in granulation tissue myofibroblasts and in quiescent and growing cultured fibroblasts. J Cell Biol. 1993;122(1):103-11.
31. Jugdutt BI. Aging and heart failure: changing demographics and implications for therapy in the elderly. Heart Fail Rev. 2010;15(5):401-5.
32. Rabinovitch M, Guignabert C, Humbert M, Nicolls MR. Inflammation and immunity in the pathogenesis of pulmonary arterial hypertension. Circ Res. 2014;115(1):165-75.
33. Ye Y, Xu Q, Wuren T. Inflammation and immunity in the pathogenesis of hypoxic pulmonary hypertension. Front Immunol. 2023;14:1162556.
34. Florentin J, Coppin E, Vasamsetti SB, Zhao J, Tai YY, Tang Y, et al. Inflammatory Macrophage Expansion in Pulmonary Hypertension Depends upon Mobilization of Blood-Borne Monocytes. J Immunol. 2018;200(10):3612-25.
35. Huertas A, Tu L, Humbert M, Guignabert C. Chronic inflammation within the vascular wall in pulmonary arterial hypertension: more than a spectator. Cardiovasc Res. 2020;116(5):885-93.
36. Huertas A, Phan C, Bordenave J, Tu L, Thuillet R, Le Hiress M, et al. Regulatory T Cell Dysfunction in Idiopathic, Heritable and Connective Tissue-Associated Pulmonary Arterial Hypertension. Chest. 2016;149(6):1482-93.
37. Marsh LM, Jandl K, Grunig G, Foris V, Bashir M, Ghanim B, et al. The inflammatory cell landscape in the lungs of patients with idiopathic pulmonary arterial hypertension. Eur Respir J. 2018;51(1).
38. Savai R, Pullamsetti SS, Kolbe J, Bieniek E, Voswinckel R, Fink L, et al. Immune and inflammatory cell involvement in the pathology of idiopathic pulmonary arterial hypertension. Am J Respir Crit Care Med. 2012;186(9):897-908.
39. Perros F, Dorfmuller P, Montani D, Hammad H, Waelput W, Girerd B, et al. Pulmonary lymphoid neogenesis in idiopathic pulmonary arterial hypertension. Am J Respir Crit Care Med. 2012;185(3):311-21.

40. Aldabbous L, Abdul-Salam V, McKinnon T, Duluc L, Pepke-Zaba J, Southwood M, et al. Neutrophil Extracellular Traps Promote Angiogenesis: Evidence From Vascular Pathology in Pulmonary Hypertension. Arterioscler Thromb Vasc Biol. 2016;36(10):2078-87.
41. Bousseau S, Sobrano Fais R, Gu S, Frump A, Lahm T. Pathophysiology and new advances in pulmonary hypertension. BMJ Med. 2023;2(1):e000137.
42. Steiner MK, Syrkina OL, Kolliputi N, Mark EJ, Hales CA, Waxman AB. Interleukin-6 overexpression induces pulmonary hypertension. Circ Res. 2009;104(2):236-44, 28p following 44.
43. Chien SY, Huang CY, Tsai CH, Wang SW, Lin YM, Tang CH. Interleukin-1beta induces fibroblast growth factor 2 expression and subsequently promotes endothelial progenitor cell angiogenesis in chondrocytes. Clin Sci (Lond). 2016;130(9):667-81.
44. Jones PL, Cowan KN, Rabinovitch M. Tenascin-C, proliferation and subendothelial fibronectin in progressive pulmonary vascular disease. Am J Pathol. 1997;150(4):1349-60.
45. Soon E, Holmes AM, Treacy CM, Doughty NJ, Southgate L, Machado RD, et al. Elevated levels of inflammatory cytokines predict survival in idiopathic and familial pulmonary arterial hypertension. Circulation. 2010;122(9):920-7.
46. Matura LA, Ventetuolo CE, Palevsky HI, Lederer DJ, Horn EM, Mathai SC, et al. Interleukin-6 and tumor necrosis factor-alpha are associated with quality of life-related symptoms in pulmonary arterial hypertension. Ann Am Thorac Soc. 2015;12(3):370-5.
47. Tatius B, Wasityastuti W, Astarini FD, Nugrahaningsih DAA. Significance of BMPR2 mutations in pulmonary arterial hypertension. Respir Investig. 2021;59(4):397-407.
48. Funk-Hilsdorf TC, Behrens F, Grune J, Simmons S. Dysregulated Immunity in Pulmonary Hypertension: From Companion to Composer. Front Physiol. 2022;13:819145.
49. Morrison SJ, Scadden DT. The bone marrow niche for haematopoietic stem cells. Nature. 2014;505(7483):327-34.
50. Comazzetto S, Shen B, Morrison SJ. Niches that regulate stem cells and hematopoiesis in adult bone marrow. Dev Cell. 2021;56(13):1848-60.
51. Chen JY, Miyanishi M, Wang SK, Yamazaki S, Sinha R, Kao KS, et al. Hoxb5 marks long-term haematopoietic stem cells and reveals a homogenous perivascular niche. Nature. 2016;530(7589):223-7.
52. Itkin T, Gur-Cohen S, Spencer JA, Schajnovitz A, Ramasamy SK, Kusumbe AP, et al. Distinct bone marrow blood vessels differentially regulate haematopoiesis. Nature. 2016;532(7599):323-8.
53. Kunisaki Y, Bruns I, Scheiermann C, Ahmed J, Pinho S, Zhang D, et al. Arteriolar niches maintain haematopoietic stem cell quiescence. Nature. 2013;502(7473):637-43.
54. Ding L, Saunders TL, Enikolopov G, Morrison SJ. Endothelial and perivascular cells maintain haematopoietic stem cells. Nature. 2012;481(7382):457-62.
55. Greenbaum A, Hsu YM, Day RB, Schuettpelz LG, Christopher MJ, Borgerding JN, et al. CXCL12 in early mesenchymal progenitors is required for haematopoietic stem-cell maintenance. Nature. 2013;495(7440):227-30.
56. Mendelson A, Frenette PS. Hematopoietic stem cell niche maintenance during homeostasis and regeneration. Nat Med. 2014;20(8):833-46.
57. Spangrude GJ, Heimfeld S, Weissman IL. Purification and characterization of mouse hematopoietic stem cells. Science. 1988;241(4861):58-62.
58. Ikuta K, Weissman IL. Evidence that hematopoietic stem cells express mouse c-kit but do not depend on steel factor for their generation. Proc Natl Acad Sci U S A. 1992;89(4):1502-6.
59. Osawa M, Hanada K, Hamada H, Nakauchi H. Long-term lymphohematopoietic reconstitution by a single CD34-low/negative hematopoietic stem cell. Science. 1996;273(5272):242-5.

60. Oguro H, Ding L, Morrison SJ. SLAM family markers resolve functionally distinct subpopulations of hematopoietic stem cells and multipotent progenitors. Cell Stem Cell. 2013;13(1):102-16.
61. Gao X, Xu C, Asada N, Frenette PS. The hematopoietic stem cell niche: from embryo to adult. Development. 2018;145(2).
62. Wilson NK, Kent DG, Buettner F, Shehata M, Macaulay IC, Calero-Nieto FJ, et al. Combined Single-Cell Functional and Gene Expression Analysis Resolves Heterogeneity within Stem Cell Populations. Cell Stem Cell. 2015;16(6):712-24.
63. Safina K, van Galen P. New frameworks for hematopoiesis derived from single-cell genomics. Blood. 2024;144(10):1039-47.
64. Morrison SJ, Weissman IL. The long-term repopulating subset of hematopoietic stem cells is deterministic and isolatable by phenotype. Immunity. 1994;1(8):661-73.
65. Schoedel KB, Morcos MNF, Zerjatke T, Roeder I, Grinenko T, Voehringer D, et al. The bulk of the hematopoietic stem cell population is dispensable for murine steady-state and stress hematopoiesis. Blood. 2016;128(19):2285-96.
66. Yang L, Bryder D, Adolfsson J, Nygren J, Mansson R, Sigvardsson M, et al. Identification of Lin(-)Sca1(+)kit(+)CD34(+)Flt3- short-term hematopoietic stem cells capable of rapidly reconstituting and rescuing myeloablated transplant recipients. Blood. 2005;105(7):2717-23.
67. Xue J, Schmidt SV, Sander J, Draffehn A, Krebs W, Quester I, et al. Transcriptome-based network analysis reveals a spectrum model of human macrophage activation. Immunity. 2014;40(2):274-88.
68. Merien F. A Journey with Elie Metchnikoff: From Innate Cell Mechanisms in Infectious Diseases to Quantum Biology. Front Public Health. 2016;4:125.
69. Gordon S, Pluddemann A. Tissue macrophages: heterogeneity and functions. BMC Biol. 2017;15(1):53.
70. T'Jonck W, Guilliams M, Bonnardel J. Niche signals and transcription factors involved in tissue-resident macrophage development. Cell Immunol. 2018;330:43-53.
71. Mantovani A, Sozzani S, Locati M, Allavena P, Sica A. Macrophage polarization: tumor-associated macrophages as a paradigm for polarized M2 mononuclear phagocytes. Trends Immunol. 2002;23(11):549-55.
72. Zaslona Z, O'Neill LAJ. Cytokine-like Roles for Metabolites in Immunity. Mol Cell. 2020;78(5):814-23.
73. Tannahill GM, Curtis AM, Adamik J, Palsson-McDermott EM, McGettrick AF, Goel G, et al. Succinate is an inflammatory signal that induces IL-1beta through HIF-1alpha. Nature. 2013;496(7444):238-42.
74. de la Calle-Fabregat C, Calafell-Segura J, Gardet M, Dunsmore G, Mulder K, Ciudad L, et al. NF-kappaB and TET2 promote macrophage reprogramming in hypoxia that overrides the immunosuppressive effects of the tumor microenvironment. Sci Adv. 2024;10(38):eadq5226.
75. Liu PS, Wang H, Li X, Chao T, Teav T, Christen S, et al. alpha-ketoglutarate orchestrates macrophage activation through metabolic and epigenetic reprogramming. Nat Immunol. 2017;18(9):985-94.
76. Pan PK, Wu TM, Tsai HY, Cho IC, Tseng HW, Lin TD, et al. Acid external and internal environment exchange the Oreochromis niloticus tissue immune gene expression compared to the mouse macrophage polarization model. Front Immunol. 2022;13:1012078.
77. El-Kenawi A, Gatenbee C, Robertson-Tessi M, Bravo R, Dhillon J, Balagurunathan Y, et al. Acidity promotes tumour progression by altering macrophage phenotype in prostate cancer. Br J Cancer. 2019;121(7):556-66.

78. Chen S, Yan D, Qiu A. The role of macrophages in pulmonary hypertension: Pathogenesis and targeting. Int Immunopharmacol. 2020;88:106934.
79. Florentin J, Dutta P. Origin and production of inflammatory perivascular macrophages in pulmonary hypertension. Cytokine. 2017;100:11-5.
80. Wynn TA, Chawla A, Pollard JW. Macrophage biology in development, homeostasis and disease. Nature. 2013;496(7446):445-55.
81. Hashimoto D, Chow A, Noizat C, Teo P, Beasley MB, Leboeuf M, et al. Tissue-resident macrophages self-maintain locally throughout adult life with minimal contribution from circulating monocytes. Immunity. 2013;38(4):792-804.
82. Yu X, Buttgereit A, Lelios I, Utz SG, Cansever D, Becher B, et al. The Cytokine TGF-beta Promotes the Development and Homeostasis of Alveolar Macrophages. Immunity. 2017;47(5):903-12 e4.
83. Misharin AV, Morales-Nebreda L, Reyfman PA, Cuda CM, Walter JM, McQuattie-Pimentel AC, et al. Monocyte-derived alveolar macrophages drive lung fibrosis and persist in the lung over the life span. J Exp Med. 2017;214(8):2387-404.
84. Auffray C, Fogg D, Garfa M, Elain G, Join-Lambert O, Kayal S, et al. Monitoring of blood vessels and tissues by a population of monocytes with patrolling behavior. Science. 2007;317(5838):666-70.
85. Jakubzick C, Gautier EL, Gibbings SL, Sojka DK, Schlitzer A, Johnson TE, et al. Minimal differentiation of classical monocytes as they survey steady-state tissues and transport antigen to lymph nodes. Immunity. 2013;39(3):599-610.
86. Epelman S, Lavine KJ, Randolph GJ. Origin and functions of tissue macrophages. Immunity. 2014;41(1):21-35.
87. Epelman S, Lavine KJ, Beaudin AE, Sojka DK, Carrero JA, Calderon B, et al. Embryonic and adult-derived resident cardiac macrophages are maintained through distinct mechanisms at steady state and during inflammation. Immunity. 2014;40(1):91-104.
88. Chen R, Zhang H, Tang B, Luo Y, Yang Y, Zhong X, et al. Macrophages in cardiovascular diseases: molecular mechanisms and therapeutic targets. Signal Transduct Target Ther. 2024;9(1):130.
89. Hulsmans M, Clauss S, Xiao L, Aguirre AD, King KR, Hanley A, et al. Macrophages Facilitate Electrical Conduction in the Heart. Cell. 2017;169(3):510-22 e20.
90. Lim GB. Macrophages and neutrophils modulate arrhythmia risk after myocardial infarction. Nat Rev Cardiol. 2022;19(9):573.
91. Leid J, Carrelha J, Boukarabila H, Epelman S, Jacobsen SE, Lavine KJ. Primitive Embryonic Macrophages are Required for Coronary Development and Maturation. Circ Res. 2016;118(10):1498-511.
92. Bajpai G, Bredemeyer A, Li W, Zaitsev K, Koenig AL, Lokshina I, et al. Tissue Resident CCR2- and CCR2+ Cardiac Macrophages Differentially Orchestrate Monocyte Recruitment and Fate Specification Following Myocardial Injury. Circ Res. 2019;124(2):263-78.
93. Epelman S, Liu PP, Mann DL. Role of innate and adaptive immune mechanisms in cardiac injury and repair. Nat Rev Immunol. 2015;15(2):117-29.
94. Dick SA, Wong A, Hamidzada H, Nejat S, Nechanitzky R, Vohra S, et al. Three tissue resident macrophage subsets coexist across organs with conserved origins and life cycles. Sci Immunol. 2022;7(67):eabf7777.
95. Frid MG, Brunetti JA, Burke DL, Carpenter TC, Davie NJ, Reeves JT, et al. Hypoxia-induced pulmonary vascular remodeling requires recruitment of circulating mesenchymal precursors of a monocyte/macrophage lineage. Am J Pathol. 2006;168(2):659-69.
96. Xiao Y, Yu D. Tumor microenvironment as a therapeutic target in cancer. Pharmacol Ther. 2021;221:107753.

97. Zawia A, Arnold ND, West L, Pickworth JA, Turton H, Iremonger J, et al. Altered Macrophage Polarization Induces Experimental Pulmonary Hypertension and Is Observed in Patients With Pulmonary Arterial Hypertension. Arterioscler Thromb Vasc Biol. 2021;41(1):430-45.
98. Pullamsetti SS, Savai R. Macrophage Regulation during Vascular Remodeling: Implications for Pulmonary Hypertension Therapy. Am J Respir Cell Mol Biol. 2017;56(5):556-8.
99. Pugliese SC, Kumar S, Janssen WJ, Graham BB, Frid MG, Riddle SR, et al. A Time- and Compartment-Specific Activation of Lung Macrophages in Hypoxic Pulmonary Hypertension. J Immunol. 2017;198(12):4802-12.
100. Kumar S, Mickael C, Kumar R, Prasad RR, Campbell NV, Zhang H, et al. Single cell transcriptomic analyses reveal diverse and dynamic changes of distinct populations of lung interstitial macrophages in hypoxia-induced pulmonary hypertension. Front Immunol. 2024;15:1372959.
101. Sanchez O, Marcos E, Perros F, Fadel E, Tu L, Humbert M, et al. Role of endothelium-derived CC chemokine ligand 2 in idiopathic pulmonary arterial hypertension. Am J Respir Crit Care Med. 2007;176(10):1041-7.
102. Zhang J, Hu H, Palma NL, Harrison JK, Mubarak KK, Carrie RD, et al. Hypoxia-induced endothelial CX3CL1 triggers lung smooth muscle cell phenotypic switching and proliferative expansion. Am J Physiol Lung Cell Mol Physiol. 2012;303(10):L912-22.
103. Dorfmuller P, Zarka V, Durand-Gasselin I, Monti G, Balabanian K, Garcia G, et al. Chemokine RANTES in severe pulmonary arterial hypertension. Am J Respir Crit Care Med. 2002;165(4):534-9.
104. Frantz C, Cauvet A, Durand A, Gonzalez V, Pierre R, Do Cruzeiro M, et al. Driving Role of Interleukin-2-Related Regulatory CD4+ T Cell Deficiency in the Development of Lung Fibrosis and Vascular Remodeling in a Mouse Model of Systemic Sclerosis. Arthritis Rheumatol. 2022;74(8):1387-98.
105. Prabhu SD, Frangogiannis NG. The Biological Basis for Cardiac Repair After Myocardial Infarction: From Inflammation to Fibrosis. Circ Res. 2016;119(1):91-112.
106. Frangogiannis NG. Regulation of the inflammatory response in cardiac repair. Circ Res. 2012;110(1):159-73.
107. Wan E, Yeap XY, Dehn S, Terry R, Novak M, Zhang S, et al. Enhanced efferocytosis of apoptotic cardiomyocytes through myeloid-epithelial-reproductive tyrosine kinase links acute inflammation resolution to cardiac repair after infarction. Circ Res. 2013;113(8):1004-12.
108. Yap J, Irei J, Lozano-Gerona J, Vanapruks S, Bishop T, Boisvert WA. Macrophages in cardiac remodelling after myocardial infarction. Nat Rev Cardiol. 2023;20(6):373-85.
109. Heidt T, Courties G, Dutta P, Sager HB, Sebas M, Iwamoto Y, et al. Differential contribution of monocytes to heart macrophages in steady-state and after myocardial infarction. Circ Res. 2014;115(2):284-95.
110. Frangogiannis NG, Dewald O, Xia Y, Ren G, Haudek S, Leucker T, et al. Critical role of monocyte chemoattractant protein-1/CC chemokine ligand 2 in the pathogenesis of ischemic cardiomyopathy. Circulation. 2007;115(5):584-92.
111. Lavine KJ, Epelman S, Uchida K, Weber KJ, Nichols CG, Schilling JD, et al. Distinct macrophage lineages contribute to disparate patterns of cardiac recovery and remodeling in the neonatal and adult heart. Proc Natl Acad Sci U S A. 2014;111(45):16029-34.
112. Liu W, Zhang X, Zhao M, Zhang X, Chi J, Liu Y, et al. Activation in M1 but not M2 Macrophages Contributes to Cardiac Remodeling after Myocardial Infarction in Rats: a Critical Role of the Calcium Sensing Receptor/NRLP3 Inflammasome. Cell Physiol Biochem. 2015;35(6):2483-500.

113. Jing R, Long TY, Pan W, Li F, Xie QY. IL-6 knockout ameliorates myocardial remodeling after myocardial infarction by regulating activation of M2 macrophages and fibroblast cells. Eur Rev Med Pharmacol Sci. 2019;23(14):6283-91.

114. Weber KT, Sun Y, Bhattacharya SK, Ahokas RA, Gerling IC. Myofibroblast-mediated mechanisms of pathological remodelling of the heart. Nat Rev Cardiol. 2013;10(1):15-26.

115. Bageghni SA, Hemmings KE, Yuldasheva NY, Maqbool A, Gamboa-Esteves FO, Humphreys NE, et al. Fibroblast-specific deletion of interleukin-1 receptor-1 reduces adverse cardiac remodeling following myocardial infarction. JCI Insight. 2019;5(17).

116. Lugrin J, Parapanov R, Milano G, Cavin S, Debonneville A, Krueger T, et al. The systemic deletion of interleukin-1alpha reduces myocardial inflammation and attenuates ventricular remodeling in murine myocardial infarction. Sci Rep. 2023;13(1):4006.

117. Iyer RP, de Castro Bras LE, Patterson NL, Bhowmick M, Flynn ER, Asher M, et al. Early matrix metalloproteinase-9 inhibition post-myocardial infarction worsens cardiac dysfunction by delaying inflammation resolution. J Mol Cell Cardiol. 2016;100:109-17.

118. Cai S, Zhao M, Zhou B, Yoshii A, Bugg D, Villet O, et al. Mitochondrial dysfunction in macrophages promotes inflammation and suppresses repair after myocardial infarction. J Clin Invest. 2023;133(4).

119. Howangyin KY, Zlatanova I, Pinto C, Ngkelo A, Cochain C, Rouanet M, et al. Myeloid-Epithelial-Reproductive Receptor Tyrosine Kinase and Milk Fat Globule Epidermal Growth Factor 8 Coordinately Improve Remodeling After Myocardial Infarction via Local Delivery of Vascular Endothelial Growth Factor. Circulation. 2016;133(9):826-39.

120. Bacmeister L, Schwarzl M, Warnke S, Stoffers B, Blankenberg S, Westermann D, et al. Inflammation and fibrosis in murine models of heart failure. Basic Res Cardiol. 2019;114(3):19.

121. Zaman R, Hamidzada H, Kantores C, Wong A, Dick SA, Wang Y, et al. Selective loss of resident macrophage-derived insulin-like growth factor-1 abolishes adaptive cardiac growth to stress. Immunity. 2021;54(9):2057-71 e6.

122. Liao X, Shen Y, Zhang R, Sugi K, Vasudevan NT, Alaiti MA, et al. Distinct roles of resident and nonresident macrophages in nonischemic cardiomyopathy. Proc Natl Acad Sci U S A. 2018;115(20):E4661-E9.

123. Patel B, Ismahil MA, Hamid T, Bansal SS, Prabhu SD. Mononuclear Phagocytes Are Dispensable for Cardiac Remodeling in Established Pressure-Overload Heart Failure. PLoS One. 2017;12(1):e0170781.

124. Patel B, Bansal SS, Ismahil MA, Hamid T, Rokosh G, Mack M, et al. CCR2(+) Monocyte-Derived Infiltrating Macrophages Are Required for Adverse Cardiac Remodeling During Pressure Overload. JACC Basic Transl Sci. 2018;3(2):230-44.

125. Suetomi T, Willeford A, Brand CS, Cho Y, Ross RS, Miyamoto S, et al. Inflammation and NLRP3 Inflammasome Activation Initiated in Response to Pressure Overload by Ca(2+)/Calmodulin-Dependent Protein Kinase II delta Signaling in Cardiomyocytes Are Essential for Adverse Cardiac Remodeling. Circulation. 2018;138(22):2530-44.

126. Li X, You J, Dai F, Wang S, Yang FH, Wang X, et al. TAK1 Activation by NLRP3 Deficiency Confers Cardioprotection Against Pressure Overload-Induced Cardiomyocyte Pyroptosis and Hypertrophy. JACC Basic Transl Sci. 2023;8(12):1555-73.

127. Horio T, Nishikimi T, Yoshihara F, Nagaya N, Matsuo H, Takishita S, et al. Production and secretion of adrenomedullin in cultured rat cardiac myocytes and nonmyocytes: stimulation by interleukin-1beta and tumor necrosis factor-alpha. Endocrinology. 1998;139(11):4576-80.

128. Chou CH, Hung CS, Liao CW, Wei LH, Chen CW, Shun CT, et al. IL-6 trans-signalling contributes to aldosterone-induced cardiac fibrosis. Cardiovasc Res. 2018;114(5):690-702.

129. Ma F, Li Y, Jia L, Han Y, Cheng J, Li H, et al. Macrophage-stimulated cardiac fibroblast production of IL-6 is essential for TGF beta/Smad activation and cardiac fibrosis induced by angiotensin II. PLoS One. 2012;7(5):e35144.

130. Wculek SK, Dunphy G, Heras-Murillo I, Mastrangelo A, Sancho D. Metabolism of tissue macrophages in homeostasis and pathology. Cell Mol Immunol. 2022;19(3):384-408.
131. Mills EL, Kelly B, Logan A, Costa ASH, Varma M, Bryant CE, et al. Succinate Dehydrogenase Supports Metabolic Repurposing of Mitochondria to Drive Inflammatory Macrophages. Cell. 2016;167(2):457-70 e13.
132. Kedia-Mehta N, Finlay DK. Competition for nutrients and its role in controlling immune responses. Nat Commun. 2019;10(1):2123.
133. Winn NC, Volk KM, Hasty AH. Regulation of tissue iron homeostasis: the macrophage "ferrostat". JCI Insight. 2020;5(2).
134. Wenes M, Shang M, Di Matteo M, Goveia J, Martin-Perez R, Serneels J, et al. Macrophage Metabolism Controls Tumor Blood Vessel Morphogenesis and Metastasis. Cell Metab. 2016;24(5):701-15.
135. Koelwyn GJ, Corr EM, Erbay E, Moore KJ. Regulation of macrophage immunometabolism in atherosclerosis. Nat Immunol. 2018;19(6):526-37.
136. Hassel B, Ilebekk A, Tonnessen T. Cardiac accumulation of citrate during brief myocardial ischaemia and reperfusion in the pig in vivo. Acta Physiol Scand. 1998;164(1):53-9.
137. Lauterbach MA, Hanke JE, Serefidou M, Mangan MSJ, Kolbe CC, Hess T, et al. Toll-like Receptor Signaling Rewires Macrophage Metabolism and Promotes Histone Acetylation via ATP-Citrate Lyase. Immunity. 2019;51(6):997-1011 e7.
138. Bruick RK, McKnight SL. A conserved family of prolyl-4-hydroxylases that modify HIF. Science. 2001;294(5545):1337-40.
139. Kjellman U, Bjork K, Ekroth R, Karlsson H, Jagenburg R, Nilsson F, et al. Alpha-ketoglutarate for myocardial protection in heart surgery. Lancet. 1995;345(8949):552-3.
140. Chen Y, Wu G, Li M, Hesse M, Ma Y, Chen W, et al. LDHA-mediated metabolic reprogramming promoted cardiomyocyte proliferation by alleviating ROS and inducing M2 macrophage polarization. Redox Biol. 2022;56:102446.
141. de Couto G, Jaghatspanyan E, DeBerge M, Liu W, Luther K, Wang Y, et al. Mechanism of Enhanced MerTK-Dependent Macrophage Efferocytosis by Extracellular Vesicles. Arterioscler Thromb Vasc Biol. 2019;39(10):2082-96.
142. Lee CF, Caudal A, Abell L, Nagana Gowda GA, Tian R. Targeting NAD(+) Metabolism as Interventions for Mitochondrial Disease. Sci Rep. 2019;9(1):3073.
143. Zhang MQ, Wang CC, Pang XB, Shi JZ, Li HR, Xie XM, et al. Role of macrophages in pulmonary arterial hypertension. Front Immunol. 2023;14:1152881.
144. Shin JH, Yang JY, Jeon BY, Yoon YJ, Cho SN, Kang YH, et al. (1)H NMR-based metabolomic profiling in mice infected with Mycobacterium tuberculosis. J Proteome Res. 2011;10(5):2238-47.
145. Strelko CL, Lu W, Dufort FJ, Seyfried TN, Chiles TC, Rabinowitz JD, et al. Itaconic acid is a mammalian metabolite induced during macrophage activation. J Am Chem Soc. 2011;133(41):16386-9.
146. Chu F, Li Y, Meng X, Li Y, Li T, Zhai M, et al. Gut Microbial Dysbiosis and Changes in Fecal Metabolic Phenotype in Precancerous Lesions of Gastric Cancer Induced With N-Methyl-N'-Nitro-N-Nitrosoguanidine, Sodium Salicylate, Ranitidine, and Irregular Diet. Front Physiol. 2021;12:733979.
147. Michelucci A, Cordes T, Ghelfi J, Pailot A, Reiling N, Goldmann O, et al. Immune-responsive gene 1 protein links metabolism to immunity by catalyzing itaconic acid production. Proc Natl Acad Sci U S A. 2013;110(19):7820-5.
148. Mills EL, Ryan DG, Prag HA, Dikovskaya D, Menon D, Zaslona Z, et al. Itaconate is an anti-inflammatory metabolite that activates Nrf2 via alkylation of KEAP1. Nature. 2018;556(7699):113-7.

149. Liao ST, Han C, Xu DQ, Fu XW, Wang JS, Kong LY. 4-Octyl itaconate inhibits aerobic glycolysis by targeting GAPDH to exert anti-inflammatory effects. Nat Commun. 2019;10(1):5091.

150. Lampropoulou V, Sergushichev A, Bambouskova M, Nair S, Vincent EE, Loginicheva E, et al. Itaconate Links Inhibition of Succinate Dehydrogenase with Macrophage Metabolic Remodeling and Regulation of Inflammation. Cell Metab. 2016;24(1):158-66.

151. Chen LL, Morcelle C, Cheng ZL, Chen X, Xu Y, Gao Y, et al. Itaconate inhibits TET DNA dioxygenases to dampen inflammatory responses. Nat Cell Biol. 2022;24(3):353-63.

152. Ganta VC, Choi MH, Kutateladze A, Fox TE, Farber CR, Annex BH. A MicroRNA93-Interferon Regulatory Factor-9-Immunoresponsive Gene-1-Itaconic Acid Pathway Modulates M2-Like Macrophage Polarization to Revascularize Ischemic Muscle. Circulation. 2017;135(24):2403-25.

153. Runtsch MC, Angiari S, Hooftman A, Wadhwa R, Zhang Y, Zheng Y, et al. Itaconate and itaconate derivatives target JAK1 to suppress alternative activation of macrophages. Cell Metab. 2022;34(3):487-501 e8.

154. Chen C, Liu C, Sun P, Zhang Z, Wang Z, Liu P, et al. Itaconate uptake via SLC13A3 improves hepatic antibacterial innate immunity. Dev Cell. 2024;59(21):2807-17 e8.

155. Lin H, Tison K, Du Y, Kirchhoff P, Kim C, Wang W, et al. Itaconate transporter SLC13A3 impairs tumor immunity via endowing ferroptosis resistance. Cancer Cell. 2024.

156. Bolger AM, Lohse M, Usadel B. Trimmomatic: a flexible trimmer for Illumina sequence data. Bioinformatics. 2014;30(15):2114-20.

157. Dobin A, Davis CA, Schlesinger F, Drenkow J, Zaleski C, Jha S, et al. STAR: ultrafast universal RNA-seq aligner. Bioinformatics. 2013;29(1):15-21.

158. Liao Y, Smyth GK, Shi W. featureCounts: an efficient general purpose program for assigning sequence reads to genomic features. Bioinformatics. 2014;30(7):923-30.

159. Love MI, Huber W, Anders S. Moderated estimation of fold change and dispersion for RNA-seq data with DESeq2. Genome Biol. 2014;15(12):550.

160. Lê S, Josse J, Husson F. FactoMineR: An R Package for Multivariate Analysis. Journal of Statistical Software. 2008;25(1):1 - 18.

161.Pelletier JP, Mineau F, Faure MP, Martel-Pelletier J. Imbalance between the mechanisms of activation and inhibition of metalloproteases in the early lesions of experimental osteoarthritis. Arthritis Rheum. 1990;33(10):1466-76.

162.Urboniene D, Haber I, Fang YH, Thenappan T, Archer SL. Validation of high-resolution echocardiography and magnetic resonance imaging vs. high-fidelity catheterization in experimental pulmonary hypertension. Am J Physiol Lung Cell Mol Physiol. 2010;299(3):L401-12.

163. Yu W, Schmachtel T, Fawaz M, Rieger MA. Isolation of murine bone marrow hematopoietic stem and progenitor cell populations via flow cytometry. Methods Cell Biol. 2022;171:173-95.

164. Gomez-Arroyo J, Saleem SJ, Mizuno S, Syed AA, Bogaard HJ, Abbate A, et al. A brief overview of mouse models of pulmonary arterial hypertension: problems and prospects. Am J Physiol Lung Cell Mol Physiol. 2012;302(10):L977-91.

165. Hoffmann J, Luxan G, Abplanalp WT, Glaser SF, Rasper T, Fischer A, et al. Post-myocardial infarction heart failure dysregulates the bone vascular niche. Nat Commun. 2021;12(1):3964.

166. Shan W, Cui J, Song Y, Yan D, Feng L, Jian Y, et al. Itaconate as a key player in cardiovascular immunometabolism. Free Radic Biol Med. 2024;219:64-75.

167. Duan X, Hu M, Yang L, Zhang S, Wang B, Li T, et al. IRG1 prevents excessive inflammatory responses and cardiac dysfunction after myocardial injury. Biochem Pharmacol. 2023;213:115614.

168. Cyr Y, Bozal FK, Barcia Duran JG, Newman AAC, Amadori L, Smyrnis P, et al. The IRG1-itaconate axis protects from cholesterol-induced inflammation and atherosclerosis. Proc Natl Acad Sci U S A. 2024;121(15):e2400675121.
169. Song J, Zhang Y, Frieler RA, Andren A, Wood S, Tyrrell DJ, et al. Itaconate suppresses atherosclerosis by activating a Nrf2-dependent antiinflammatory response in macrophages in mice. J Clin Invest. 2023;134(3).
170. Soehnlein O, Libby P. Targeting inflammation in atherosclerosis - from experimental insights to the clinic. Nat Rev Drug Discov. 2021;20(8):589-610.
171. Moore KJ, Koplev S, Fisher EA, Tabas I, Bjorkegren JLM, Doran AC, et al. Macrophage Trafficking, Inflammatory Resolution, and Genomics in Atherosclerosis: JACC Macrophage in CVD Series (Part 2). J Am Coll Cardiol. 2018;72(18):2181-97.
172. Warnatsch A, Ioannou M, Wang Q, Papayannopoulos V. Inflammation. Neutrophil extracellular traps license macrophages for cytokine production in atherosclerosis. Science. 2015;349(6245):316-20.
173. Lei I, Huang W, Noly PE, Naik S, Ghali M, Liu L, et al. Metabolic reprogramming by immune-responsive gene 1 up-regulation improves donor heart preservation and function. Sci Transl Med. 2023;15(682):eade3782.
174. Swigut T, Wysocka J. H3K27 demethylases, at long last. Cell. 2007;131(1):29-32.
175. Ming-Chin Lee K, Achuthan AA, De Souza DP, Lupancu TJ, Binger KJ, Lee MKS, et al. Type I interferon antagonism of the JMJD3-IRF4 pathway modulates macrophage activation and polarization. Cell Rep. 2022;39(3):110719.
176. Qin W, Zhang Y, Tang H, Liu D, Chen Y, Liu Y, et al. Chemoproteomic Profiling of Itaconation by Bioorthogonal Probes in Inflammatory Macrophages. J Am Chem Soc. 2020;142(25):10894-8.
177. Mangum KD, Li Q, Bauer TM, Wolf SJ, Shadiow J, Moon JY, et al. Epigenetic Alteration of Smooth Muscle Cells Regulates Endothelin-Dependent Blood Pressure and Hypertensive Arterial Remodeling. medRxiv. 2024.
178. Dhaun N, Webb DJ. Endothelins in cardiovascular biology and therapeutics. Nat Rev Cardiol. 2019;16(8):491-502.
179. Li M, He HP, Gong HQ, Zhang J, Ma WJ, Zhou H, et al. NFATc4 and myocardin synergistically up-regulate the expression of LTCC alpha1C in ET-1-induced cardiomyocyte hypertrophy. Life Sci. 2016;155:11-20.
180. Cody RJ, Haas GJ, Binkley PF, Capers Q, Kelley R. Plasma endothelin correlates with the extent of pulmonary hypertension in patients with chronic congestive heart failure. Circulation. 1992;85(2):504-9.
181. Clozel M, Gray GA, Breu V, Loffler BM, Osterwalder R. The endothelin ETB receptor mediates both vasodilation and vasoconstriction in vivo. Biochem Biophys Res Commun. 1992;186(2):867-73.
182. Dhople AM, Hanks JH. Factors that influence the growth of Mycobacterium lepraemurium in the Nakamura's system. Int J Lepr Other Mycobact Dis. 1976;44(1-2):18-26.
183. Tamamori M, Ito H, Adachi S, Akimoto H, Marumo F, Hiroe M. Endothelin-3 induces hypertrophy of cardiomyocytes by the endogenous endothelin-1-mediated mechanism. J Clin Invest. 1996;97(2):366-72.
184. Ohkita M, Takaoka M, Kobayashi Y, Itoh E, Uemachi H, Matsumura Y. Involvement of proteasome in endothelin-1 production in cultured vascular endothelial cells. Jpn J Pharmacol. 2002;88(2):197-205.
185. Song H, Xu T, Feng X, Lai Y, Yang Y, Zheng H, et al. Itaconate prevents abdominal aortic aneurysm formation through inhibiting inflammation via activation of Nrf2. EBioMedicine. 2020;57:102832.

186. Vidal I, Fernandez-Florido E, Marrero AD, Castilla L, A RQ, Martinez-Poveda B, et al. The Immunomodulator Dimethyl Itaconate Inhibits Several Key Steps of Angiogenesis in Cultured Endothelial Cells. Int J Mol Sci. 2022;23(24).

187. Zhao C, Jiang P, He Z, Yuan X, Guo J, Li Y, et al. Dimethyl itaconate protects against lippolysacchride-induced mastitis in mice by activating MAPKs and Nrf2 and inhibiting NF-kappaB signaling pathways. Microb Pathog. 2019;133:103541.

188. Swain A, Bambouskova M, Kim H, Andhey PS, Duncan D, Auclair K, et al. Comparative evaluation of itaconate and its derivatives reveals divergent inflammasome and type I interferon regulation in macrophages. Nat Metab. 2020;2(7):594-602.

189. Qian HL, Chen SY, Jia F, Huang WP, Wang J, Ren KF, et al. "Spongy skin" as a robust strategy to deliver 4-octyl itaconate for conducting dual-regulation against in-stent restenosis. Biomaterials. 2023;296:122069.

190. Adegnika AA, de Vries SG, Zinsou FJ, Honkepehedji YJ, Dejon Agobe JC, Vodonou KG, et al. Safety and immunogenicity of co-administered hookworm vaccine candidates Na-GST-1 and Na-APR-1 in Gabonese adults: a randomised, controlled, double-blind, phase 1 dose-escalation trial. Lancet Infect Dis. 2021;21(2):275-85.

191.Chen WM, Lin ZY. [Controversies on the diagnosis and treatment of relapsed/refractory multiple myeloma]. Zhonghua Yi Xue Za Zhi. 2022;102(30):2311-4.

192.Wada H, Miyauchi K, Suwa S, Miyazaki S, Hayashi H, Yamashiro K, et al. Impact of atrial fibrillation type (paroxysmal vs. non-paroxysmal) on long-term clinical outcomes: The RAFFINE registry subanalysis. J Cardiol. 2023;81(5):450-5.

193. Liang Y, Xu ML, Wang XW, Gao XX, Cheng JJ, Li C, et al. ATP synthesis is active on the cell surface of the shrimp Litopenaeus vannamei and is suppressed by WSSV infection. Virol J. 2015;12:49.

194. Zetterberg E, Popat U, Hasselbalch H, Prchal J, Palmblad J. Angiogenesis in pulmonary hypertension with myelofibrosis. Haematologica. 2008;93(6):945-6.

195.Popat U, Frost A, Liu E, Guan Y, Durette A, Reddy V, et al. High levels of circulating CD34 cells, dacrocytes, clonal hematopoiesis, and JAK2 mutation differentiate myelofibrosis with myeloid metaplasia from secondary myelofibrosis associated with pulmonary hypertension. Blood. 2006;107(9):3486-8.

196.Guilpain P, Montani D, Damaj G, Achouh L, Lefrere F, Le Pavec J, et al. Pulmonary hypertension associated with myeloproliferative disorders: a retrospective study of ten cases. Respiration. 2008;76(3):295-302.

197. Farha S, Asosingh K, Xu W, Sharp J, George D, Comhair S, et al. Hypoxia-inducible factors in human pulmonary arterial hypertension: a link to the intrinsic myeloid abnormalities. Blood. 2011;117(13):3485-93.

198.Asosingh K, Farha S, Lichtin A, Graham B, George D, Aldred M, et al. Pulmonary vascular disease in mice xenografted with human BM progenitors from patients with pulmonary arterial hypertension. Blood. 2012;120(6):1218-27.

199. Machado RF, Farber HW. Pulmonary hypertension associated with chronic hemolytic anemia and other blood disorders. Clin Chest Med. 2013;34(4):739-52.

200. Boldyrev AI. [Treatment of children and adolescents in the initial stage of epilepsy]. Zh Nevropatol Psikhiatr Im S S Korsakova. 1988;88(6):61-6.

201. Atkinson C, Stewart S, Upton PD, Machado R, Thomson JR, Trembath RC, et al. Primary pulmonary hypertension is associated with reduced pulmonary vascular expression of type II bone morphogenetic protein receptor. Circulation. 2002;105(14):1672-8.

202. Crosby A, Toshner MR, Southwood MR, Soon E, Dunmore BJ, Groves E, et al. Hematopoietic stem cell transplantation alters susceptibility to pulmonary hypertension in Bmpr2-deficient mice. Pulm Circ. 2018;8(4):2045894018801642.

203. Primignani M, Barosi G, Bergamaschi G, Gianelli U, Fabris F, Reati R, et al. Role of the JAK2 mutation in the diagnosis of chronic myeloproliferative disorders in splanchnic vein thrombosis. Hepatology. 2006;44(6):1528-34.

204. Kimishima Y, Misaka T, Yokokawa T, Wada K, Ueda K, Sugimoto K, et al. Clonal hematopoiesis with JAK2V617F promotes pulmonary hypertension with ALK1 upregulation in lung neutrophils. Nat Commun. 2021;12(1):6177.
205. Jaiswal S, Natarajan P, Silver AJ, Gibson CJ, Bick AG, Shvartz E, et al. Clonal Hematopoiesis and Risk of Atherosclerotic Cardiovascular Disease. N Engl J Med. 2017;377(2):111-21.
206. Dorsheimer L, Assmus B, Rasper T, Ortmann CA, Ecke A, Abou-El-Ardat K, et al. Association of Mutations Contributing to Clonal Hematopoiesis With Prognosis in Chronic Ischemic Heart Failure. JAMA Cardiol. 2019;4(1):25-33.
207. Mas-Peiro S, Hoffmann J, Fichtlscherer S, Dorsheimer L, Rieger MA, Dimmeler S, et al. Clonal haematopoiesis in patients with degenerative aortic valve stenosis undergoing transcatheter aortic valve implantation. Eur Heart J. 2020;41(8):933-9.
208. Jaiswal S, Ebert BL. Clonal hematopoiesis in human aging and disease. Science. 2019;366(6465).
209. Jaiswal S, Fontanillas P, Flannick J, Manning A, Grauman PV, Mar BG, et al. Age-related clonal hematopoiesis associated with adverse outcomes. N Engl J Med. 2014;371(26):2488-98.
210. Schleicher WE, Hoag B, De Dominici M, DeGregori J, Pietras EM. CHIP: a clonal odyssey of the bone marrow niche. J Clin Invest. 2024;134(15).
211. Mansouri S, Hemmerling I, Hesami G, Cremer S, Kirschbaum K, Klatt S, et al. Metabolic alterations drive inflammatory phenotypes in CHIP-associated heart failure. bioRxiv. 2024:2024.07.30.605744.
212. Abplanalp WT, Schuhmacher B, Cremer S, Merten M, Shumliakivska M, Macinkovic I, et al. Cell-intrinsic effects of clonal hematopoiesis in heart failure. Nat Cardiovasc Res. 2023;2(9):819-34.
213. Mansson R, Hultquist A, Luc S, Yang L, Anderson K, Kharazi S, et al. Molecular evidence for hierarchical transcriptional lineage priming in fetal and adult stem cells and multipotent progenitors. Immunity. 2007;26(4):407-19.
214. Bell JJ, Bhandoola A. The earliest thymic progenitors for T cells possess myeloid lineage potential. Nature. 2008;452(7188):764-7.
215. Luc S, Anderson K, Kharazi S, Buza-Vidas N, Boiers C, Jensen CT, et al. Down-regulation of Mpl marks the transition to lymphoid-primed multipotent progenitors with gradual loss of granulocyte-monocyte potential. Blood. 2008;111(7):3424-34.
216. Hirai H, Zhang P, Dayaram T, Hetherington CJ, Mizuno S, Imanishi J, et al. C/EBPbeta is required for 'emergency' granulopoiesis. Nat Immunol. 2006;7(7):732-9.
217. Manz MG, Boettcher S. Emergency granulopoiesis. Nat Rev Immunol. 2014;14(5):302-14.
218. Pietras EM, Mirantes-Barbeito C, Fong S, Loeffler D, Kovtonyuk LV, Zhang S, et al. Chronic interleukin-1 exposure drives haematopoietic stem cells towards precocious myeloid differentiation at the expense of self-renewal. Nat Cell Biol. 2016;18(6):607-18.
219. Vanickova K, Milosevic M, Ribeiro Bas I, Burocziova M, Yokota A, Danek P, et al. Hematopoietic stem cells undergo a lymphoid to myeloid switch in early stages of emergency granulopoiesis. EMBO J. 2023;42(23):e113527.
220. Ratajczak MZ, Adamiak M, Plonka M, Abdel-Latif A, Ratajczak J. Mobilization of hematopoietic stem cells as a result of innate immunity-mediated sterile inflammation in the bone marrow microenvironment-the involvement of extracellular nucleotides and purinergic signaling. Leukemia. 2018;32(5):1116-23.
221. Chen GY, Nunez G. Sterile inflammation: sensing and reacting to damage. Nat Rev Immunol. 2010;10(12):826-37.

222. Golan K, Vagima Y, Ludin A, Itkin T, Cohen-Gur S, Kalinkovich A, et al. S1P promotes murine progenitor cell egress and mobilization via S1P1-mediated ROS signaling and SDF-1 release. Blood. 2012;119(11):2478-88.

223. Adamiak M, Poniewierska-Baran A, Borkowska S, Schneider G, Abdelbaset-Ismail A, Suszynska M, et al. Evidence that a lipolytic enzyme--hematopoietic-specific phospholipase C-beta2--promotes mobilization of hematopoietic stem cells by decreasing their lipid raft-mediated bone marrow retention and increasing the promobilizing effects of granulocytes. Leukemia. 2016;30(4):919-28.

224. Lederer WH, Gerstbrein HL. Creatine kinase isoenzyme BB activity in serum of a patient with gastric cancer. Clin Chem. 1976;22(10):1748-9.

225. Feng W, Wang L, Zheng G. Expression and function of P2 receptors in hematopoietic stem and progenitor cells. Stem Cell Investig. 2015;2:14.

226. Adamiak M, Bujko K, Cymer M, Plonka M, Glaser T, Kucia M, et al. Novel evidence that extracellular nucleotides and purinergic signaling induce innate immunity-mediated mobilization of hematopoietic stem/progenitor cells. Leukemia. 2018;32(9):1920-31.

227. Ratajczak MZ. A novel view of the adult bone marrow stem cell hierarchy and stem cell trafficking. Leukemia. 2015;29(4):776-82.

228. Massberg S, Schaerli P, Knezevic-Maramica I, Kollnberger M, Tubo N, Moseman EA, et al. Immunosurveillance by hematopoietic progenitor cells trafficking through blood, lymph, and peripheral tissues. Cell. 2007;131(5):994-1008.

229. Davie NJ, Crossno JT, Jr., Frid MG, Hofmeister SE, Reeves JT, Hyde DM, et al. Hypoxia-induced pulmonary artery adventitial remodeling and neovascularization: contribution of progenitor cells. Am J Physiol Lung Cell Mol Physiol. 2004;286(4):L668-78.

230. Gambaryan N, Perros F, Montani D, Cohen-Kaminsky S, Mazmanian M, Renaud JF, et al. Targeting of c-kit+ haematopoietic progenitor cells prevents hypoxic pulmonary hypertension. Eur Respir J. 2011;37(6):1392-9.

231. Favre S, Gambini E, Nigro P, Scopece A, Bianciardi P, Caretti A, et al. Sildenafil attenuates hypoxic pulmonary remodelling by inhibiting bone marrow progenitor cells. J Cell Mol Med. 2017;21(5):871-80.

13. Ehrenwörtliche Erklärung

„Hiermit erkläre ich, dass ich die vorliegende Arbeit selbständig und ohne unzulässige Hilfe oder Benutzung anderer als der angegebenen Hilfsmittel angefertigt habe. Alle Textstellen, die wörtlich oder sinngemäß aus veröffentlichten oder nichtveröffentlichten Schriften entnommen sind, und alle Angaben, die auf mündlichen Auskünften beruhen, sind als solche kenntlich gemacht. Bei den von mir durchgeführten und in der Dissertation erwähnten Untersuchungen habe ich die Grundsätze guter wissenschaftlicher Praxis, wie sie in der „Satzung der Justus-Liebig-Universität Gießen zur Sicherung guter wissenschaftlicher Praxis“ niedergelegt sind, eingehalten sowie ethische, datenschutzrechtliche und tierschutzrechtliche Grundsätze befolgt. Ich versichere, dass Dritte von mir weder unmittelbar noch mittelbar geldwerte Leistungen für Arbeiten erhalten haben, die im Zusammenhang mit dem Inhalt der vorgelegten Dissertation stehen, und dass die vorgelegte Arbeit weder im Inland noch im Ausland in gleicher oder ähnlicher Form einer anderen Prüfungsbehörde zum Zweck einer Promotion oder eines anderen Prüfungsverfahrens vorgelegt wurde. Alles aus anderen Quellen und von anderen Personen übernommene Material, das in der Arbeit verwendet wurde oder auf das direkt Bezug genommen wird, wurde als solches kenntlich gemacht. Insbesondere wurden alle Personen genannt, die direkt und indirekt an der Entstehung der vorliegenden Arbeit beteiligt waren. Mit der Überprüfung meiner Arbeit durch eine Plagiatserkennungssoftware bzw. ein internetbasiertes Softwareprogramm erkläre ich mich einverstanden.“

_____ _____

Ort/Datum Unterschrift

14. Acknowledgments

I would like to extend my deepest appreciation to my advisor, Prof. Dr. Soni Savai Pullamsetti, for her outstanding mentorship and unwavering support throughout my PhD journey. Her extensive knowledge, patience, and genuine kindness have greatly influenced me, both professionally and individually. I consider myself incredibly lucky to have had such an inspiring mentor during this critical stage of my academic career.

I am also sincerely appreciative of Prof. Dr. Rajkumar Savai for his insightful feedback and invaluable perspectives from the initial stages of the project, which greatly enhanced my research. I am deeply thankful to Prof. Dr. Werner Seeger for his encouragement and for posing thought-provoking questions that pushed me to think more critically and broaden the scope of my work.

I am sincerely grateful to my collaborators, whose efforts were crucial to the success of this project. I extend my sincere appreciation to Prof. Dr. Michael Rieger for his expertise in hematopoietic cell phenotyping, Dr. Baktybek Kojonazarov for conducting the echocardiographic analyses, Prof. Dr. Andreas Weigert for his support with the FACS analyses, and Dr. Stefan Günther for his work on the transcriptomic studies.

I would also like to thank my labmates, both past and present, for their support and friendship throughout this journey. I am grateful to Dr. Chanil Valasarajan, whose enthusiasm and insightful discussions made my Ph.D. experience highly rewarding. I am also grateful to Monika Haselbauer for her dedicated help with administrative tasks, and to all the technical assistants, whose dedication was essential to the smooth running of the lab and the success of this research.

My heartfelt thanks go to my dear friends, Parisa, Javad, Solmaz, Setareh, Shahriar, Mohammad, Hanieh, and Jamal, who their unwavering friendship and the shared moments of laughter made the challenges far more bearable.

To my family, my wonderful parents, Shojae and Farideh, and my siblings, Shahab, Vahid, and Mehrnaz, I am deeply thankful for their constant love, support, and belief in me, which gave me the strength to persevere through all the highs and lows of this academic journey.

Finally, I want to dedicate my deepest appreciation to Siavash, the love of my life, who has been my unwavering partner throughout every step of this process. His intellectual contributions to my research, along with his emotional support, patience, and countless sacrifices, were invaluable. Having someone so supportive and encouraging by my side has been an extraordinary blessing, and I am endlessly appreciative to him.